

**The Effect of Sulfur in Rotary Kiln Fuels on Nickel Laterite  
Calcination**

by

**Muhammad Haziq Uddin**

B.A.Sc., The University of British Columbia, 2017

A THESIS SUBMITTED IN PARTIAL FULFILLMENT OF  
THE REQUIREMENTS FOR THE DEGREE OF

**MASTER OF APPLIED SCIENCE**

in

THE FACULTY OF GRADUATE AND POSTDOCTORAL STUDIES  
(Materials Engineering)

THE UNIVERSITY OF BRITISH COLUMBIA

(Vancouver)

January 2020

© Muhammad Haziq Uddin, 2020

The following individuals certify that they have read, and recommend to the Faculty of Graduate and Postdoctoral Studies for acceptance, a thesis/dissertation entitled:

The Effect of Sulfur in Rotary Kiln Fuels on Nickel Laterite Calcination

submitted by Muhammad Haziq Uddin in partial fulfillment of the requirements for

the degree of Master of Applied Science

in Materials Engineering

**Examining Committee:**

Leili Tafaghodi Khajavi, Materials Engineering  
Supervisor

David Dreisinger, Materials Engineering  
Supervisory Committee Member

Edouard Asselin, Materials Engineering  
Supervisory Committee Member

## Abstract

Rotary Kiln - Electric Furnace (RKEF) process is the most commonly used pyrometallurgical technique for processing nickel laterite ores and is mainly suited for saprolite deposits. Sulfur is one of the most harmful elements in crude ferronickel obtained via the RKEF process and adversely affects the mechanical properties of the final product. Typically, laterite ores contain insubstantial sulfur content; hence, it is hypothesized that most of the sulfur in crude ferronickel originates from the coal added as the fuel and the reductant during calcination in the rotary kiln. This study investigates the role of sulfur content of rotary kiln fuels on the composition of the calcine.

The calcination-partial reduction experiments were conducted in a furnace at 900 °C for a 2-hour residence time. Various reducing gas mixtures representing combustion product of rotary kiln fuels (i.e., coal) were contacted with the ore. The sulfur content of the resulting calcines were measured by ICP-AES analysis. At constant  $P_{CO}$ , the sulfur content of the calcine increases linearly with an increase in  $P_{SO_2}$  in the input gas mixtures. Similarly, at fixed  $P_{SO_2}$ , the percentage of sulfur in the calcine and sulfur deportation increase with  $P_{CO}$ . However, an exceptional case is observed at  $P_{SO_2} = 0$  atm, where the sulfur content and sulfur deportation slightly decrease by increasing  $P_{CO}$  in the input gas. The sulfur content and the percentage of sulfur deportation drop at a lower input flow rate of the reducing gas mixtures. Lastly, the sum of the metallized and sulfurized iron/nickel was found to increase with an increase in  $P_{SO_2}$ .

## **Lay Summary**

Rotary Kiln - Electric Furnace (RKEF) process is a pyrometallurgical technique to extract nickel from laterite ores. It is essentially a two-step process where the ore is first calcined in a rotary kiln and then smelted in an electric furnace. The product of the RKEF process is crude ferronickel (iron-nickel alloy), which needs to be refined for impurities such as sulfur. Sulfur is one of the most harmful impurity elements in ferronickel and degrades mechanical properties of the material. The rotary kiln is heated by combustion of fuels such as coal, which contain sulfur as an impurity. This study investigates the relationship between the sulfur content of rotary kiln fuel and the calcine.

## **Preface**

This thesis is the original, independent, and unpublished work by the author, Muhammad Haziq Uddin.

# Table of Contents

<b>Abstract .....</b>	<b>iii</b>
<b>Lay Summary .....</b>	<b>iv</b>
<b>Preface .....</b>	<b>v</b>
<b>Table of Contents .....</b>	<b>vi</b>
<b>List of Tables .....</b>	<b>ix</b>
<b>List of Figures.....</b>	<b>x</b>
<b>List of Symbols .....</b>	<b>xiv</b>
<b>List of Abbreviations.....</b>	<b>xv</b>
<b>Acknowledgments .....</b>	<b>xvi</b>
<b>Chapter 1: Introduction.....</b>	<b>1</b>
<b>Chapter 2: Literature Review.....</b>	<b>3</b>
2.1 Nickel Laterite Ores.....	3
2.1.1 Oxide Deposits.....	3
2.1.2 Hydrous Magnesium Silicates Deposits .....	3
2.1.3 Clay Silicate Deposits.....	4
2.2 Processing of Nickel Laterite Ores .....	4
2.2.1 High-Pressure Acid Leaching .....	5
2.2.1.1 Mixed-Sulfide Precipitation.....	7

2.2.1.2	Mixed-Hydroxide Precipitation.....	8
2.2.2	Caron Process (Yabulu Modification).....	9
2.2.3	Blast or Submerged Arc Furnace Smelting .....	11
2.2.4	Rotary Kiln Electric Furnace Process (Ferronickel Production) .....	12
2.2.4.1	Drying .....	14
2.2.4.2	Calcination and Partial Reduction .....	15
2.2.4.3	Smelting .....	16
2.2.4.4	Refining .....	18
2.2.5	Rotary Kiln Electric Furnace Process (Matte Production) .....	19
2.2.5.1	Roasting of Sulfide Matte .....	22
2.3	The Behavior of Laterite Ores in Carbo-Sulfurizing Gas Mixture.....	24
2.4	Scope and Objectives .....	29
<b>Chapter 3: Materials and Methods .....</b>		<b>31</b>
3.1	Materials.....	31
3.2	Characterization of Raw Materials .....	31
3.3	Preliminary Processing of the Raw Materials .....	34
3.4	Calcination and Partial Reduction Experiments.....	36
3.5	Chemical Analysis .....	42
3.5.1	Inductively Coupled Plasma - Atomic Emission Spectroscopy .....	42

3.5.2	X-ray Diffraction, Scanning Electron Microscopy and Energy Dispersive X-ray Spectroscopy .....	45
<b>Chapter 4:</b>	<b>Thermodynamic Analysis .....</b>	<b>46</b>
4.1	Model Description .....	46
4.2	Model Results.....	50
<b>Chapter 5:</b>	<b>Experimental Results and Discussion .....</b>	<b>56</b>
5.1	The Effect of $P_{SO_2}$ on the Sulfur Content of the Calcine .....	56
5.2	The Effect of $P_{CO}$ on the Sulfur Content and Sulfur Deportation in the Calcine .....	60
5.3	The Effect of the Flow Rate of the Input Gas on % S in the Calcine .....	65
5.4	X-ray Diffraction of the Calcine.....	68
5.5	The Effect $P_{SO_2}$ on Sum of Metallized and Sulfurized Iron and Nickel .....	70
5.6	Energy Dispersive Analysis of the Calcine.....	72
<b>Chapter 6:</b>	<b>Conclusion .....</b>	<b>74</b>
<b>Chapter 7:</b>	<b>Future Work.....</b>	<b>76</b>
<b>References.....</b>		<b>77</b>

## List of Tables

Table 2.1 Possible sulfurization reactions for $\text{Fe}_2\text{O}_3$ and $\text{NiO}$ at $900\text{ }^\circ\text{C}$ in $\text{CO-SO}_2$ system.....	24
Table 3.1 Chemical assay of the raw ore.....	32
Table 3.2 Composition of the coal added as the reductant.....	33
Table 3.3 The gas flow rates for the calcination and partial reduction experiments at $900\text{ }^\circ\text{C}$ and 2-hour residence time with total input flow rate of $292\text{ ml/min}$ .....	40
Table 3.4 The gas flow rates for the calcination and partial reduction experiments at $900\text{ }^\circ\text{C}$ and 2-hour residence time with total input flowrate of $176\text{ ml/min}$ .....	41
Table 4.1 List of all the considered species in thermodynamic analysis .....	46
Table 4.2 Initial and equilibrium partial pressure of different components of the gas mixtures at $900\text{ }^\circ\text{C}$ .....	48
Table 4.3 Standard Gibbs free energies of the reactions between species containing iron/nickel in the laterite ore and $\text{CO-SO}_2$ atmosphere at $900\text{ }^\circ\text{C}$ .....	49
Table 5.1 % Atomic concentration on selected points for calcine produced at $900\text{ }^\circ\text{C}$ under $P_{\text{CO}}$ and $P_{\text{SO}_2}$ equal to $0.51$ and $0.0216\text{ atm}$ , respectively .....	73

## List of Figures

Figure 2.1 An idealized profile of laterite ores from surface to bedrock [1].....	4
Figure 2.2 HPAL process flowsheet with mixed-sulfide precipitation [1] .....	6
Figure 2.3 Mixed-hydroxide precipitation flowsheet [24] .....	8
Figure 2.4 Caron process flowsheet with Yabulu modification [1, 23, 24] .....	10
Figure 2.5 The process flowsheet of the RKEF route [1] .....	13
Figure 2.6 (a) Shielded-arc electric furnace (b) Immersed electrode electric furnace [33] .....	18
Figure 2.7 PT Inco sulfide-matte smelting flowsheet [1].....	21
Figure 2.8 Peirce-Smith converter [1].....	22
Figure 2.9 Oxidation roasting of sulfide-matte [1].....	23
Figure 2.10 Equilibrium partial pressure of gaseous components at 700 °C in CO-SO <sub>2</sub> system of various compositions [39] .....	26
Figure 2.11 TGA curves of Fe <sub>2</sub> O <sub>3</sub> samples at 700 °C in CO-SO <sub>2</sub> atmosphere with various compositions [39].....	27
Figure 2.12 TGA curves of Fe <sub>2</sub> O <sub>3</sub> samples at X <sub>CO</sub> = 0.66 for various temperatures [39] .....	28
Figure 2.13 TGA curves of laterite samples at 700 °C in CO-SO <sub>2</sub> system of various composition [40] .....	29
Figure 3.1 XRD pattern of the raw ore.....	33
Figure 3.2 (a) Oven (b) Mortar grinder mill .....	34
Figure 3.3 (a) As-received ore (b) Dried ore (c) Ground ore (d) Ground coal.....	35

Figure 3.4 Particle size distribution of the ground ore.....	35
Figure 3.5 Furnace temperature calibration by comparing the values obtained from internal and external thermocouple .....	37
Figure 3.6 (a) Gas cylinders (b) Mass flow controllers (c) Gas mixing column (d) Gas inlet to the furnace .....	38
Figure 3.7 (a) Complete experimental setup (b) Quartz reactor .....	39
Figure 3.8 Temperature cycle for calcination and partial reduction experiments .....	41
Figure 3.9 Ball mill grinder .....	43
Figure 3.10 Muffle furnace.....	43
Figure 3.11 (a) Reduced calcine (b) KOH pellets (c) Zirconium crucible (d) Leached solution ..	44
Figure 4.1 Predicted sulfur content of the calcine produced at 900 °C for various amount of gas mixtures (a) experimental amounts listed in Table 3.3 (b) one - fourth of the experimental amounts (c) one - eighth of the experimental amounts .....	52
Figure 4.2 Predicted grades (i.e., percentages of iron and nickel in ferronickel alloy) at 900 °C for experiments listed in Table 3.3 (a-c) nickel (d-f) iron .....	53
Figure 4.3 Predicted metallization of nickel/iron at 900 °C for experiments listed in Table 3.3 (a-c) nickel (d-f) iron.....	54
Figure 4.4 Predicted sulfurization of nickel/iron at 900 °C for experiments listed in Table 3.3 (a-c) nickel (d-f) iron.....	55
Figure 5.1 The effect of $P_{SO_2}$ on the sulfur content of the calcine produced at 900 °C and $P_{CO} = 0.39$ atm .....	57

Figure 5.2 The effect of $P_{SO_2}$ on the sulfur content of the calcine produced at 900 °C and $P_{CO} = 0.45$ atm.....	58
Figure 5.3 The effect of $P_{SO_2}$ on the sulfur content of the calcine produced at 900 °C and $P_{CO} = 0.51$ atm.....	58
Figure 5.4 The effect of $P_{SO_2}$ on the sulfur content of the calcine produced at 900 °C and $P_{CO} = 0.57$ atm.....	59
Figure 5.5 The effect of $P_{SO_2}$ on the sulfur content of the calcine produced at 900 °C and $P_{CO} = 0.63$ atm.....	59
Figure 5.6 Comparison of experimentally obtained % S values with thermodynamic simulations .....	60
Figure 5.7 The effect of $P_{CO}$ on the sulfur content and sulfur deportation of the calcine produced at 900 °C and $P_{SO_2} = 0$ atm .....	61
Figure 5.8 The effect of $P_{CO}$ on the sulfur content and sulfur deportation of the calcine produced at 900 °C and $P_{SO_2} = 0.0072$ atm.....	61
Figure 5.9 The effect of $P_{CO}$ on the sulfur content and sulfur deportation of the calcine produced at 900 °C and $P_{SO_2} = 0.0144$ atm.....	62
Figure 5.10 The effect of $P_{CO}$ on the sulfur content and sulfur deportation of the calcine produced at 900 °C and $P_{SO_2} = 0.0216$ atm.....	62
Figure 5.11 The effect of $P_{CO}$ on the sulfur content and sulfur deportation of the calcine produced at 900 °C and $P_{SO_2} = 0.0288$ atm.....	63

Figure 5.12 The effect of $P_{CO}$ on the sulfur content and sulfur deportation of the calcine produced at 900 °C and $P_{SO_2} = 0.0360$ atm.....	63
Figure 5.13 Comparison of experimentally obtained % S values with those predicted by the model .....	65
Figure 5.14 The effect of gas flow rate on % S in the calcine for a 2-hour residence time at 900 °C .....	67
Figure 5.15 The effect of gas flow rate on % sulfur deportation in the calcine for a 2-hour residence time at 900 °C .....	67
Figure 5.16 XRD pattern of the calcine produced at 900 °C under $P_{SO_2} = 0.0360$ atm and $P_{CO} = 0.39$ atm.....	69
Figure 5.17 XRD pattern of the calcine produced at 900 °C under $P_{SO_2} = 0.0360$ atm and $P_{CO} = 0.51$ atm.....	69
Figure 5.18 XRD pattern of the calcine produced at 900 °C under $P_{SO_2} = 0.0360$ atm and $P_{CO} = 0.63$ atm.....	70
Figure 5.19 Sum of metallized and sulfurized iron/nickel in the calcine produced at 900 °C .....	71
Figure 5.20 (a) SEM image of the calcine produced at 900 °C under $P_{CO} = 0.51$ atm and $P_{SO_2} = 0.0216$ atm (b-f) EDS mapping of iron, sulfur, silicon, and magnesium .....	72

## List of Symbols

$\Delta G^\circ$	Standard Gibbs free energy
D	Diffusion coefficient
$d_s$	Diameter of particle
$k_g$	Gas-solid mass transfer coefficient
M	Molar
$P_x$	Partial pressure of x (gas)
Re	Reynolds number
Sc	Schmidt number
Sh	Sherwood number
v	Velocity
$\mu_g$	Gas viscosity
$\rho_g$	Gas density

## List of Abbreviations

BNC	Basic nickel carbonate
BVM	Bureau Veritas Minerals
HPAL	High-pressure acid leaching
ICP-AES	Inductively coupled plasma - atomic emission spectroscopy
LOI	Loss on ignition
MH	Mixed hydroxide
MS	Mixed sulfide
NPI	Nickel pig iron
PLS	Pregnant leach solution
RKEF	Rotary kiln - electric furnace
STP	Standard temperature and pressure
XRD	X-ray diffraction
XRF	X-ray fluorescence

## **Acknowledgments**

I would like to acknowledge the continuous trust, support, and encouragement from my supervisor, Dr. Leili Tafaghodi. Without her guidance, this thesis would not be completed. Furthermore, I am thankful to our sponsors Hatch and Mitacs for providing financial support for this project.

I am grateful to my friend and mentor, Dr. Kashif Mairaj Deen, for his consistent moral and technical support. Thank you for providing your valuable time whenever I encountered challenges in my research.

I would like to thank Maureen Soon for all the help she provided in conducting ICP analysis. I really appreciate Yuchang Xiao for assisting me in experimentation and analysis during this study. Furthermore, I would like to acknowledge the cooperation of Sahand Sarbishei in setting up the lab equipment and always providing useful suggestions whenever needed.

I am indebted to all my friends, especially Mohammad Rizvi and Usman Nasim, for their unconditional support throughout my research work. Thank you for always being there for me and never letting me feel alone.

Lastly, I appreciate the love and support of my family, without whom none of my accomplishments were possible.

## Chapter 1: Introduction

Nickel is a critical alloying element in stainless steel due to its excellent corrosion resistance, workability, and strength [1]. The manufacturing of stainless steel consumes almost two-thirds of the nickel produced globally, while the remaining is consumed in the production of superalloys, non-ferrous alloys, copper alloys, electroplating, and batteries [1, 2]. The growth of the stainless steel industry is the main driving force behind the increasing demand for nickel. As a result, the annual nickel production has increased from 1.1 million tonnes to 1.6 million tonnes in the first decade of the 21<sup>st</sup> century [3]. Stainless steel is the primary market for nickel; however, nickel demand for batteries is rapidly growing and expected to influence the market in near future [4].

Nickel ores are divided into two main categories; sulfide and laterite. The total reserves for nickel are estimated to be approximately 100 million tonnes [5], with laterite ores representing 72 % of the deposits. In 2003, laterite ores accounted for only 42 % of the primary nickel production [5]. The production of nickel from laterite ores has steadily increased, and was reported 60 % in 2013 [6, 7]. The difference in the available resources and production from the laterite ores is due to their higher energy consumption and challenges in beneficiation processes. However, as a result of continued depletion of sulfide ores and increasing demand for nickel, laterite ores are becoming an essential source for nickel [9].

There are two notable sub-divisions in a laterite profile; limonite and saprolite. These are separate layers of the same deposit but sub-divided based on the nickel-bearing host minerals. Limonite accounts for approximately 60 % of the total laterite resources, while saprolite is about 32 %. The remaining 8 % is found as a layer between limonite and saprolite, and is usually known as smectite [7, 9]. Generally, limonite ores are treated using hydrometallurgical processes due to

their high iron and low magnesia and nickel content. On the other hand, saprolite ores are economically processed using pyrometallurgical methods because of their relatively low iron and high magnesia and nickel content [11].

The rotary kiln-electric furnace (RKEF) process is the primary method for extracting nickel from saprolite ores. In this technique, the ore is first calcined and pre-reduced at 850 - 1000 °C in a rotary kiln followed by smelting in an electric furnace at 1500 - 1600 °C [11, 12]. The resulting crude ferronickel is refined before casting to remove impurities such as sulfur, phosphorus, and carbon [14]. The final ferronickel product typically contains 30 % nickel and 70 % iron. The RKEF process is energy-intensive and requires both fossil fuel and electric power [6]. It is difficult to concentrate the ore before processing, and substantially all of it undergoes the high energy-consuming steps, such as calcination and smelting. The ore is usually wet and needs drying before subsequent operations. The high magnesia content of the ore increases the melting temperature [1, 8]. Therefore, the profit margins in the RKEF process are slim and require the need to cut costs across the board [15].

Sulfur is one of the deleterious elements in crude ferronickel and is partially introduced by the addition of reductants and fuels. It is highly unwanted in steel production where most of the ferronickel is used as an alloying element [14]. Therefore, it must be removed before ferronickel is cast into bars or granulated. The refining of ferronickel is usually done in a ladle furnace and sulfur is removed by adding calcium carbide. The reported consumption of calcium carbide is approximately 6 kg/kg sulfur [16]. Thus, refining may add a significant cost to the overall economics of the process. For example, crude ferronickel containing 1 wt. % sulfur requires 60 kg CaC<sub>2</sub> per tonne. Considering the current price of CaC<sub>2</sub>, this accounts for USD 42 per tonne ferronickel in reagent costs alone for the removal of sulfur.

## **Chapter 2: Literature Review**

### **2.1 Nickel Laterite Ores**

Laterite ores are a product of extensive chemical weathering of olivine-rich ultramafic rocks such as peridotite, pyroxenite, and dunite, containing nickel, cobalt, iron, and other metals [8, 15]. They occur near the surface and are available for open-pit mining techniques. The tropical regions around the equator, western Australia, and humid regions of eastern Europe are most abundant in laterite ores [18]. These ores have formed over millions of years under changing climatic and tectonic activity. Consequently, their profile is complex with varying mineralogy from the surface to bedrock (**Figure 2.1**). There are generally three distinct layers found in a laterite profile [17]: oxides, hydrous magnesium silicates, and clay silicates.

#### **2.1.1 Oxide Deposits**

Oxide deposits are commonly referred to as ‘limonite’ and occur as an upper layer of laterite profile. The principle nickel-bearing minerals are iron oxyhydroxide, mainly goethite. Nickel is present either by adsorption onto the surface or by substitution for iron in the goethite structure [7, 15]. The limonitic layer is relatively rich in iron and low in nickel, magnesia, and silica content. The global mean grade of nickel in limonite deposits is 1.03 %, and they represent about 60 % of the total nickel laterite resources.

#### **2.1.2 Hydrous Magnesium Silicates Deposits**

This layer of laterite deposits is generally referred to as ‘saprolite’ and is usually found deep in the profile. The mineralogy of saprolite ores is very inconsistent, and nickel is present as a mixture of different nickel-containing varieties of magnesium-rich silicate minerals, i.e., serpentine, talc, chlorite, and sepiolite. These minerals are also informally referred to as the

garnierite group [19]. Both iron and nickel substitute for magnesium in various hydrous magnesium silicates present in the ore [20]. They are relatively abundant in nickel, magnesia, and silica while low in iron. The global mean grade of nickel in saprolite deposits is 1.53 %, and they represent about 32 % of the total nickel laterite resources [7, 8, 15].

### 2.1.3 Clay Silicate Deposits

These deposits generally occur as a transition layer between limonite and saprolite and are commonly referred to as ‘smectite.’ They have recently been recognized and exploited as a distinct ore type [8]. Nickel-rich smectite clays such as nontronite and saponite are found noticeably in these deposits. The global mean grade of nickel in smectite deposits is 1.21 %, and they represent 8 % of total nickel laterite resources [17].

Laterite Profile	Common Name	Minerals	Approximate Analysis (%)			
			Fe	MgO	Ni	Co
Ferricrete	Ferricrete	Goethite	> 50	< 0.5	< 0.8	< 0.1
Limonite	Limonite	Hydrated FeO(OH)	40 - 50	0.5 - 5	0.8 - 1.5	0.1 - 0.2
Smectite	Smectite	Nontronite, Saponite	10 - 30	5 - 15	0.6 - 2	0.02 - 0.1
Saprolite	Saprolite	Serpentine, Chlorite, Sepiolite, Talc	10 - 25	15 - 35	1.5 - 4	0.02 - 0.1
Serpentinized Peridotite	Bedrock	Peridotite	5	35 - 40	0.3	0.01

Figure 2.1 An idealized profile of laterite ores from surface to bedrock [1]

## 2.2 Processing of Nickel Laterite Ores

The identification of different layers in the laterite ores is vital due to the different extraction processes required for each segment. In general, limonite ores are commonly processed

by hydrometallurgical methods to reduce nickel to the metallic state. High iron and low nickel in limonite ores make them uneconomical for smelting, while their low magnesia content reduces the acid consumption during the leaching process. Contrarily, saprolite ores are processed by pyrometallurgical techniques due to their high magnesia content. The relatively low iron and higher nickel make them suitable for melting [1, 10]. In the following sections, the most widely used processes to treat laterite ores are discussed in further detail.

### **2.2.1 High-Pressure Acid Leaching**

In High-Pressure Acid Leaching (HPAL), an autoclave is used to leach limonite ores facilitated by the addition of sulfuric acid and steam (**Figure 2.2**). The process takes place under aggressive conditions, i.e., 250 °C temperature and 40 Bar pressure. Under these conditions, goethite containing nickel and cobalt, can rapidly dissolve in the solution. However, the dissolved iron quickly hydrolyzes and precipitates as hematite and jarosite while regenerating the acid [21]. The recovery of nickel in pregnant leach solution (PLS) is higher than 95 %, while only 3 % iron is dissolved in the solution [20, 21]. In downstream processing, there is some loss of nickel and cobalt; however, overall recoveries are still very high, and in the range of 90 - 92 %. There are several processing options to recover nickel and cobalt from the PLS. These include precipitation to produce mixed intermediate product, i.e., sulfide and hydroxide, or by direct solvent extraction and refining [13]. The HPAL process is not economical for saprolite ores due to the high concentration of acid consuming magnesia.

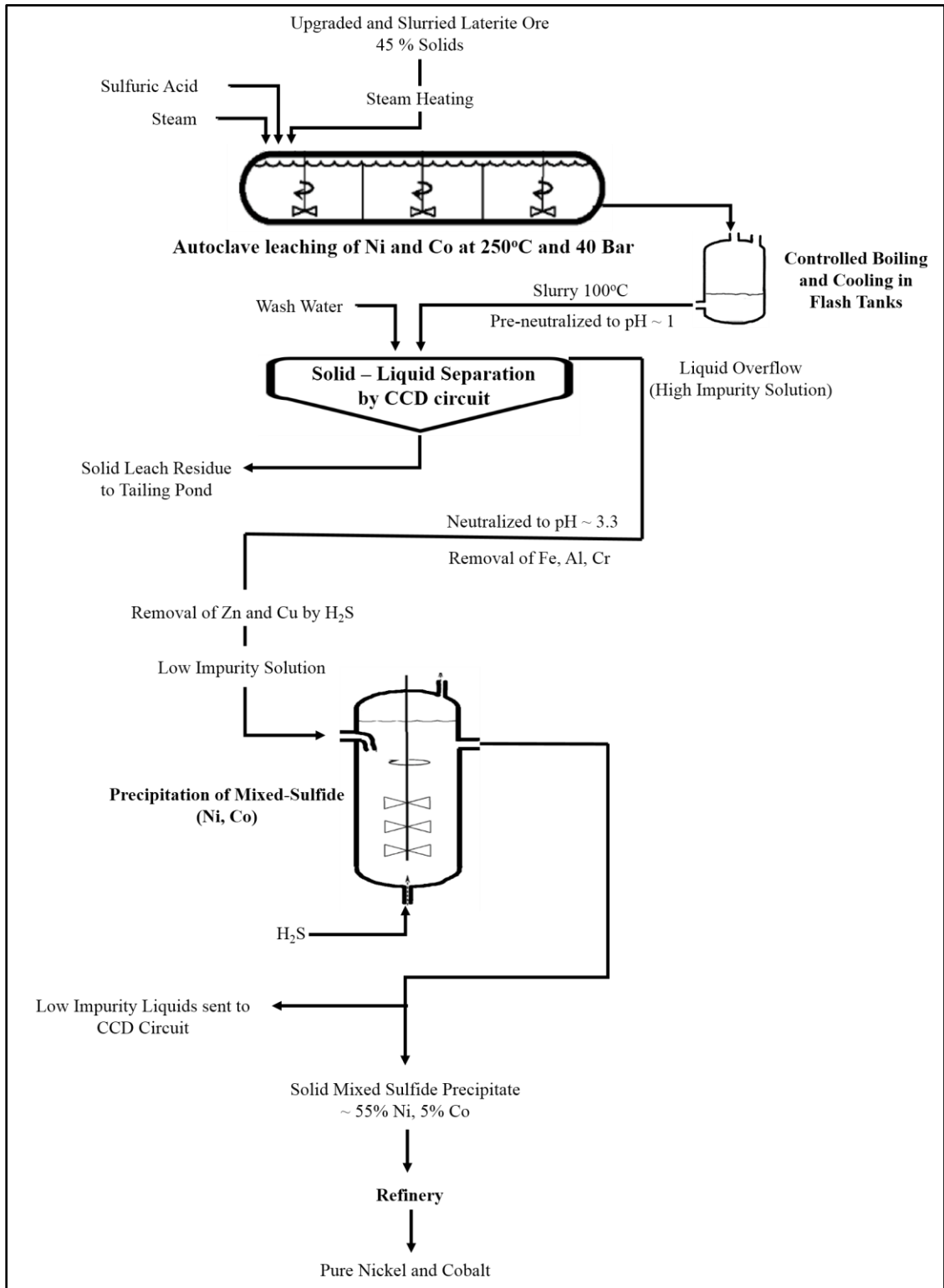


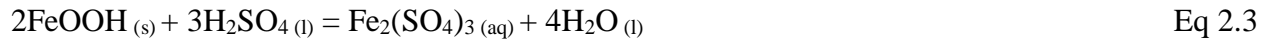
Figure 2.2 HPAL process flowsheet with mixed-sulfide precipitation [1]

The chemical reactions inside the autoclave are given by equations 2.1 - 2.5 [1]:

a) Leaching of nickel and cobalt:



b) Dissolution of goethite and precipitation of iron as hematite and jarosite



### 2.2.1.1 Mixed-Sulfide Precipitation

In a mixed-sulfide (MS) precipitation process (**Figure 2.2**), the leached slurry is allowed to boil in sequential flash tanks and then pre-neutralized with limestone to a pH of 1.0 [23]. The slurry is then passed through a 7-stage counter-current decantation circuit (CCD), which separates the PLS from the solid residues. The clarified solution is again neutralized to a pH of 3.3 to precipitate impurities, i.e., iron, aluminum, and chromium as hydroxides. Zinc and copper are removed from the solution as sulfides in a separate reactor by precipitating them selectively with hydrogen sulfide gas. Finally, the low impurity solution undergoes the sulfurization stage, where hydrogen sulfide gas is used to precipitate a mixed nickel-cobalt sulfide product. The MS product is then delivered to a refinery to recover pure nickel and cobalt metal.

The precipitation reaction of mixed nickel-cobalt sulfide is given by equation 2.6 [1]:



### 2.2.1.2 Mixed-Hydroxide Precipitation

In a mixed-hydroxide (MH) precipitation process (**Figure 2.3**), nickel and cobalt are precipitated as hydroxides, and sent for ammoniacal re-leach and refining [24]. In the first precipitation, the neutralized leach solution is reacted with magnesia slurry, which selectively precipitate nickel and cobalt as mixed hydroxides. The precipitation is selective over magnesium but not for elements such as iron, aluminum, and chromium. The resulting solution is then thickened and filtered to separate the MH cake. The liquids from the thickening and filtration process undergoes a secondary precipitation with lime to precipitate any remaining nickel and cobalt in the solution. The solids are recycled back to the autoclave discharge solution, while liquids end up in a tailing pond after waste treatment. Metallic nickel and cobalt are recovered from the MH cake by hydrometallurgical refining.

The precipitation reaction of mixed nickel-cobalt hydroxide is given by equation 2.7 [22]:

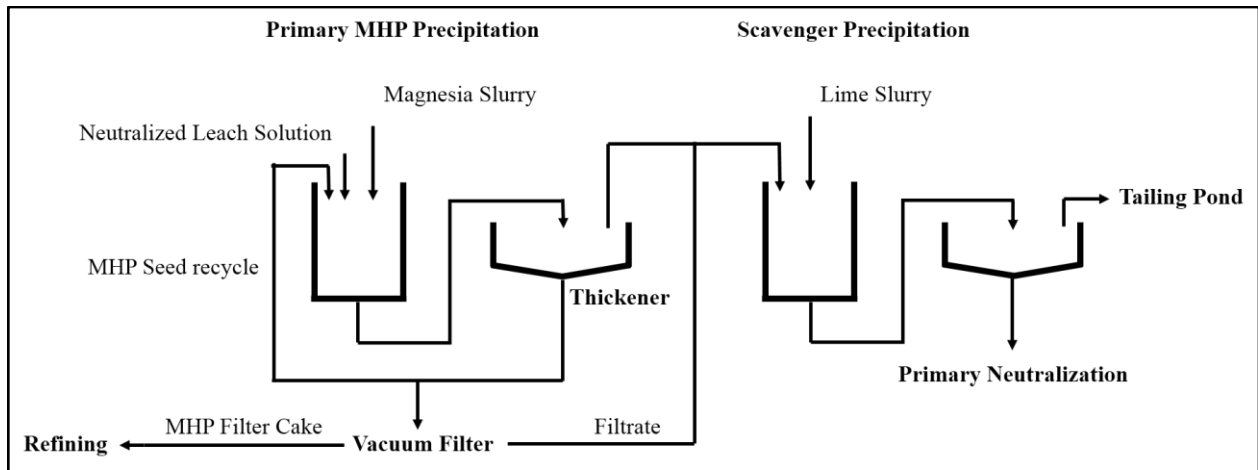
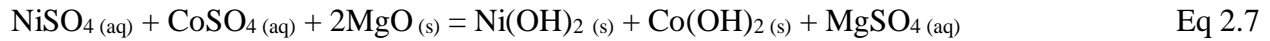
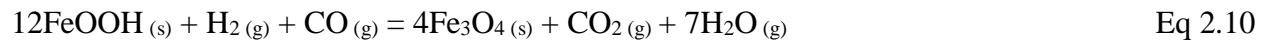
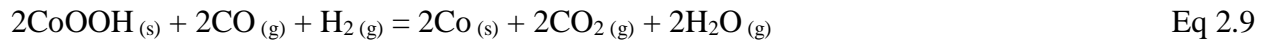


Figure 2.3 Mixed-hydroxide precipitation flowsheet [24]

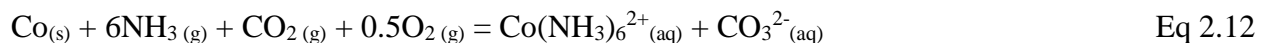
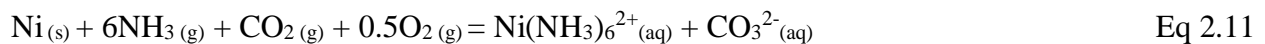
### 2.2.2 Caron Process (Yabulu Modification)

Caron process is a hybrid pyro-hydro metallurgical process to extract nickel from the laterite ores (**Figure 2.4**). It is primarily used for limonites but can also treat a mixture of limonite and saprolite. The process is extremely energy-intensive, and the overall nickel recovery is around 75 % [1]. The ore is dried, ground, and blended with heavy fuel oil before being calcined in a multiple hearth furnace operating above 700 °C in a reducing atmosphere. The nickel and cobalt oxides are reduced to metal, while the majority of iron exists as magnetite. Rotary cooler submerged partially in water bath cools the calcine to temperature below 200 °C. Subsequently, ammonia-ammonium carbonate solution leaches the calcine and selectively dissolve metallic nickel, cobalt, and iron. However, iron amine complex is unstable and rapidly precipitates as hydroxide upon reacting with oxygen [25].

The reduction reactions inside the multiple hearth furnace are given by equations 2.8 - 2.10 [1]:



The leaching of calcine by ammonia-ammonium carbonate solution is given by equations 2.11- 2.12 [1]:



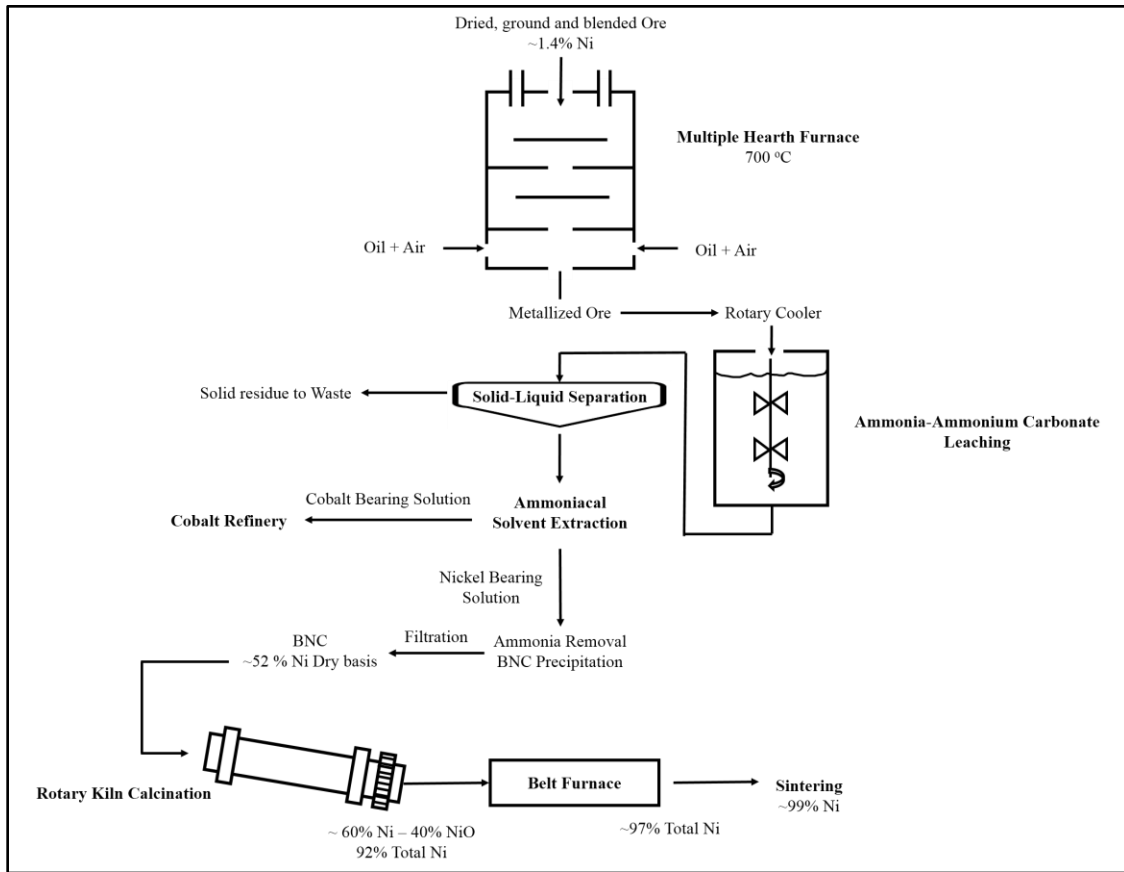


Figure 2.4 Caron process flowsheet with Yabulu modification [1, 23, 24]

The iron precipitates are removed from the solution by filtration, and copper is separated by ammoniacal solvent extraction. The purified solution is then boiled to remove ammonia and precipitate nickel as basic nickel carbonate (BNC), i.e., a mixed-carbonate-hydroxide solid. The BNC product contains 52 % nickel on a dry basis and after filtration, undergoes a series of high-temperature processes. At first, BNC is dehydrated, decomposed, and partially reduced in a rotary kiln. The calcine is a mixture of approximately 60 % nickel and 40 % nickel oxide with typically 92 % overall nickel content. The kiln product is blended with sawdust and reduced in a traveling belt furnace at 900 - 1000 °C temperature. The furnace product contains 97.5 % Ni, which is then sintered to achieve purity of more than 99 % nickel [26].

The precipitation of BNC by steam heating and its subsequent decomposition in a rotary kiln is given by equation 2.13 and 2.14, respectively [1]:



### 2.2.3 Blast or Submerged Arc Furnace Smelting

In the early 2000's, nickel pig iron (NPI) production gained a great deal of popularity in China due to the rapid rise in stainless steel demand and the soaring price of refined nickel. NPI offered a cheap alternative to the domestic demand for nickel by stainless steel producers. Several small iron blast furnace operators modified their processes to treat laterite ores. However, in 2014, Indonesia prohibited the export of laterite ores, which decreased the NPI production in China [27]. Furthermore, the strict environmental regulations, decrease in nickel prices, and several technical challenges have significantly decreased blast furnace smelting [3].

Nickel pig iron or low-grade ferronickel is essentially an iron-nickel alloy that has lower nickel content than traditional RKEF ferronickel. The process can treat low-grade limonite ores, generally containing less than 1 % nickel. The pig iron from the blast or submerged arc furnaces may contain up to 8 % and 15 % nickel, respectively [3, 26]. The production of NPI is very similar to conventional pig iron process. The ore, coke breeze, and fluxes are blended, and then sintered to form agglomerates. A blast or submerged arc furnace smelts the sintered product along with additional fluxes. The molten ferronickel is separated from the slag and refined for impurities before being poured into molds.

There are several technical challenges associated with sintering and smelting in the NPI process. The sintering consumes a large amount of coke breeze due to high moisture and refractory

materials in the ore. The smelting generates a vast amount of slag, consumes a high amount of energy, and delivers a ferronickel product with poor fluidity. The viscosity of slag is very high due to the presence of chromium oxide. The addition of fluxes, i.e., fluorite, severely erodes the refractory of the furnace, and yield poisonous gases. Moreover, the NPI contains a high level of harmful impurities, i.e., sulfur and phosphorus, which have to be removed before subsequent processing [3, 26].

#### **2.2.4 Rotary Kiln Electric Furnace Process (Ferronickel Production)**

The Rotary kiln - Electric Furnace (RKEF) process, shown in **Figure 2.5**, is the most commonly used pyrometallurgical technique for processing laterite ores and is mainly suited for saprolite deposits. In 2003, 70 % of nickel was being extracted from the laterites using the RKEF process, and it accounted for 30 % of the overall nickel production globally. In a standard operation, the feed is dried, calcined and partially reduced in a rotary kiln followed by smelting in an electric furnace. About 90 % of the smelting is done to produce a ferronickel alloy while the rest produces a sulfide matte [1, 11].

Smelting aims to selectively separate nickel as a metallic phase while rejecting the other oxides in the ore as slag. Under any reducing condition, the recovery of nickel as metal is the highest, followed by that of cobalt and iron. A small proportion of chromium and silicon may metalize as well, while all of the magnesia and alumina reports to the slag. Since the percentage of iron in the ore is an order of magnitude higher than nickel, the crude ferronickel alloy usually contains only 20 - 40 % nickel. More aggressive reducing conditions ensures higher nickel recovery but a lower nickel grade in ferronickel, and vice versa. Typically, the nickel recovery in RKEF process is higher than 90 % [1, 11].

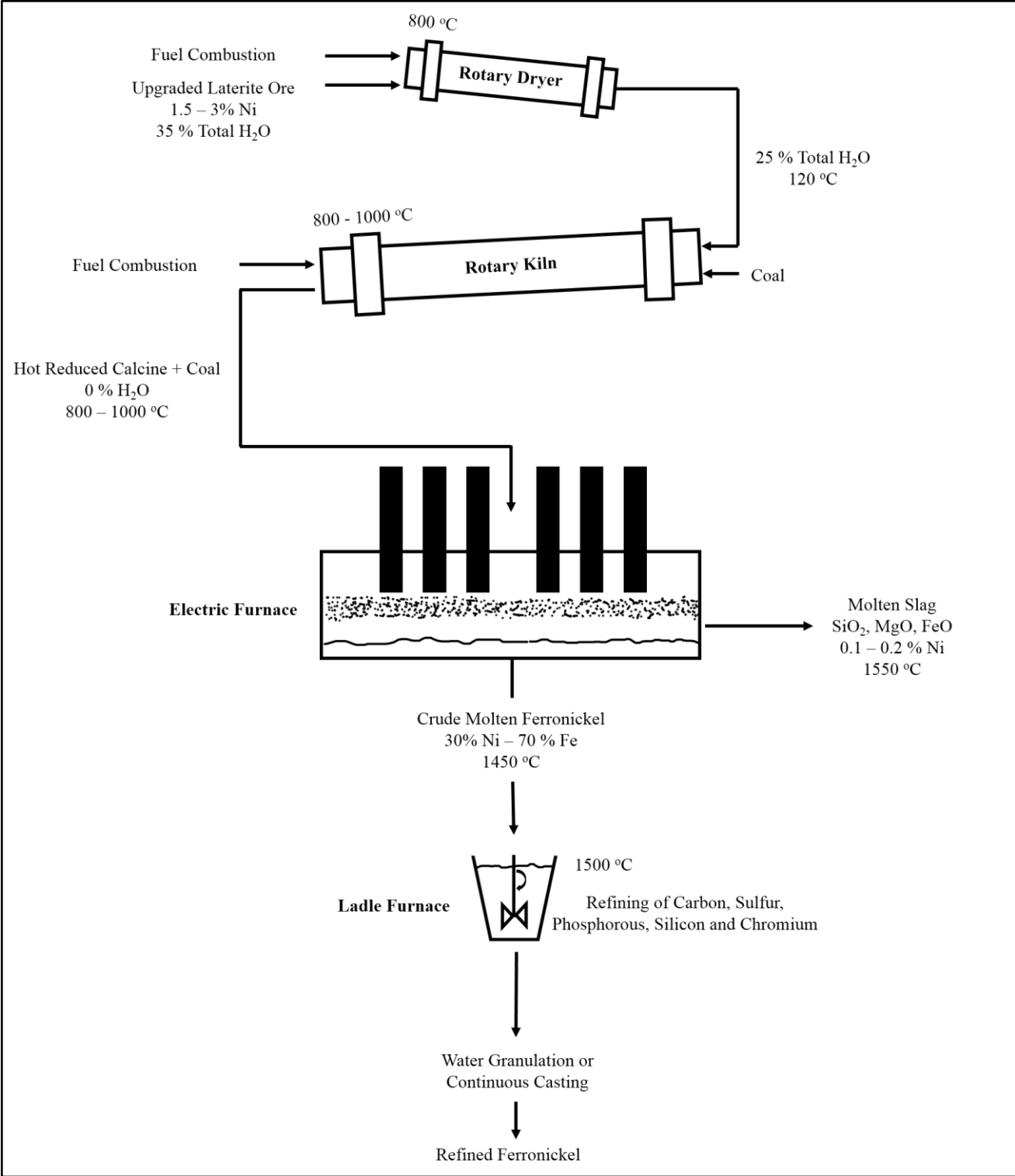


Figure 2.5 The process flowsheet of the RKEF route [1]

**Figure 2.5** shows the RKEF process flowsheet. In general, there are four main stages with following objectives:

1. *Drying*: removal of a significant portion of free moisture in the ore
2. *Calcination and Partial Reduction*: removal of remaining moisture and crystalline water in the ore, reduction of substantial portion of nickel and a controlled part of iron, and preheating the ore for smelting furnace
3. *Smelting*: complete reduction of nickel and separation of crude molten ferronickel from the slag phase
4. *Refining*: removal of impurities, i.e., sulfur, phosphorus, carbon, chromium, and silicon from crude ferronickel

The feed to the RKEF process is generally a magnesium-rich saprolite ore containing 1.5 - 3 % nickel, 15 % iron, 25 - 35 % free moisture, and 10 - 12 % crystalline water. Unlike sulfide ores, the beneficiation of laterite ores is very difficult. However, the nickel-rich weathered minerals are usually softer than the precursor rocks. Therefore, the ore is crushed, ground, and screened to separate soft nickel-rich particles. The nickel content in the upgraded ore generally increases only up to 1.2 to 2 times than the original ore [1, 27, 28].

#### **2.2.4.1 Drying**

The upgraded ore is wet, sticky, and has inconsistent moisture content. Rotary dryers usually 4 m in diameter and 30 m long, partially dries the ore [1]. Complete evaporation of water is not desired at this stage since the feed will become dusty and difficult to handle. Fuel combustion and recycled hot gases from calcination, smelting, and slag-cooling are used to heat the rotary dryer. The gases at about 600 - 800 °C interacts co-currently with the ore. The product is a dusty off-gas and partially dried ore with a consistent free moisture in the range of 15 - 20 %. The dust

is recovered from the off-gas in electrostatic precipitators and is recycled either to the dryer or calcination kiln [11, 29].

#### 2.2.4.2 Calcination and Partial Reduction

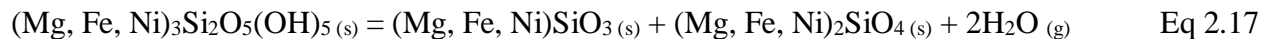
A slightly sloped rotary kiln, typically 5 m in diameter and 100 m long, receives the dried ore along with carbonaceous reductants [1]. The kiln is heated by partial combustion of fuels, e.g., coal, at the discharge end. The ore is slowly guided through the rotary kiln by internal lifters and interacts with hot reducing gases counter-currently, which eliminates the free moisture. The air fans and coal scoops along the length of the kiln controls the gas temperature and partial pressures of carbon monoxide and hydrogen [31]. At 700 °C, the lattice structure of hydrated magnesium silicates dissociates thermally, and yields highly reactive amorphous oxides while evaporating crystalline water. More than a quarter of nickel reduces to metal, while most of the Fe<sup>3+</sup> reduces to Fe<sup>2+</sup> minerals. The discharge temperature of calcine is between 800 - 1000 °C, and the off-gas temperature is between 250 - 400 °C. The dust in the off-gas accounts for almost 15 - 20 % of the kiln feed. It is recovered, pelletized, and recycled back to the calcination kiln. The bone-dry calcine, bearing enough coal for further reduction, is transferred to the smelting furnace [11, 29].

The chemical reaction in the rotary kiln can be summarized by equations 2.15 - 2.26 [1, 31]:

a) Complete evaporation of free moisture in the ore:



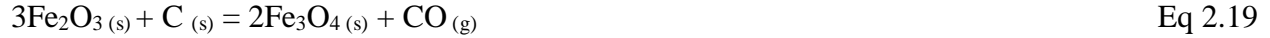
b) Thermal dissociation laterite minerals, i.e., goethite for limonite, and serpentine for saprolite:



c) Boudouard reaction:



d) Direct reduction of resulting oxides by carbon:



e) Indirect reduction of resulting oxides by reducing gases, i.e., carbon monoxide:



### 2.2.4.3 Smelting

During smelting, the nickel in the hot calcine is completely reduced to its metallic form. The crude ferronickel product typically contains 20 - 40 % nickel. Molten slag containing  $\text{SiO}_2$ ,  $\text{MgO}$  and  $\text{FeO}$  with an insignificant amount of nickel is also generated and floats on top. The crude molten ferronickel at 1450 - 1500 °C, is tapped from the lower taphole into a ladle, and transported for refining and casting. Molten slag at 1550 - 1600 °C, is tapped from high taphole and is either dumped as waste or granulated and sold as building material or metallurgical flux. The off-gas is fully combusted, dedusted, and released into the atmosphere or recycled back to the rotary dryer [1, 11, 29].

The chemical reactions in the smelting furnace can be summarized by equation 2.27 - 2.29 [1]:

a) Reduction of iron and nickel oxides to metallic state:



b) The melting and alloying of iron and nickel:



The composition of smelter slag depends on the feed and typically contains 40 - 55 % SiO<sub>2</sub>, 20 - 35 % MgO, 5 - 20 % FeO, 1 - 7 % CaO and 1 - 2 % Al<sub>2</sub>O<sub>3</sub> [1]. The slag is ionic and made up of cations such as Mg<sup>2+</sup> and Fe<sup>2+</sup>, and anion mainly SiO<sub>4</sub><sup>4-</sup>. The loss of nickel in the slag is minimal, and recovery in ferronickel is usually between 90 - 98 %. The nickel losses can be further minimized by increasing nickel content of the feed, tapping slag at higher temperatures and adding enough carbon for complete reduction of nickel oxide.

Industrial furnaces are either rectangular with six carbon electrodes or round with three electrodes [1]. These electrodes are consumed during the smelting process by oxidation of carbon and are regenerated at the top by welding. A high amount of current flows between suspended electrodes and Joule heating provides the energy for melting the calcine.

Most of ferronickel producers practice the shielded arc method nowadays [33], which enables the transfer of the power directly from the arc to the calcine (**Figure 2.6**). The electric current passes from one electrode of a pair to the other electrode through the air gap and slag. Almost 80 % of the energy is provided by Joule heating in the air gaps where it is readily available for heating and melting the solid calcine. The shielded arc method minimizes the energy requirements, prevents overheating of refractories, and increases the rate of melting. In contrast,

the immersed electrode method superheats the slag bath, which results in melting of the overlaying calcine. It has several disadvantages, i.e., higher heat and electrical energy losses, higher consumption of electrode, faster degradation of refractories, and larger size and cost for the required electrode.

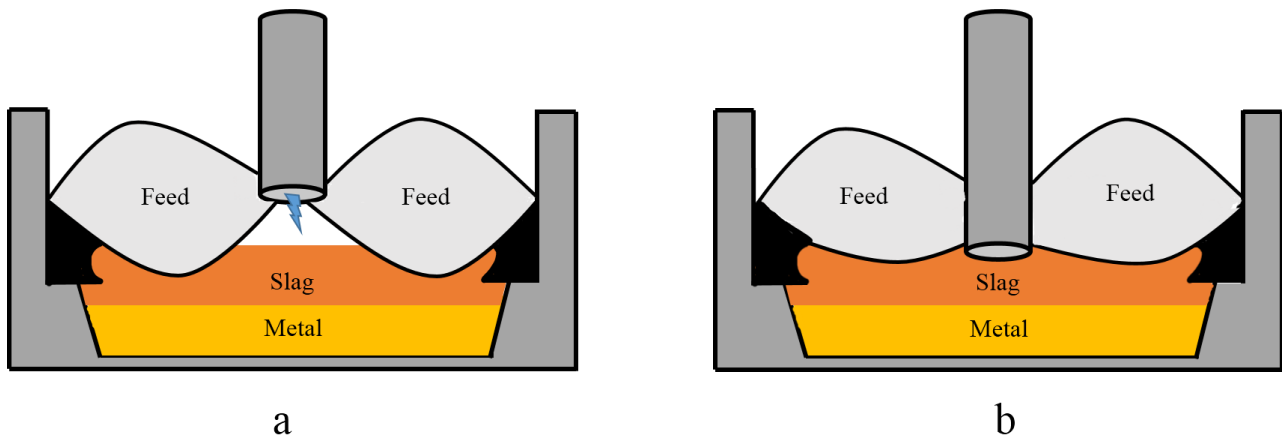


Figure 2.6 (a) Shielded-arc electric furnace (b) Immersed electrode electric furnace [33]

#### 2.2.4.4 Refining

The crude ferronickel from the smelter may contain up to 0.06 % phosphorus and 1 % sulfur, whereas the desired ferronickel product must contain less than 0.02 % phosphorus and 0.05 % sulfur. Impurities such as carbon and silicon may sometime also be above the acceptable limits. A ladle heated up to 1550 - 1600 °C is used to do all of the refining operations on freshly tapped ferronickel. It physically moves through each of the refining station, i.e., dephosphorization, desulfurization, and decarburization [1].

Lime and oxygen are added into molten ferronickel to remove phosphorus as calcium phosphate. Lime is added into the ladle before and during the refining process for efficient mixing while oxygen is blown deep into ferronickel by refractory-coated stainless-steel lances [1]. Phosphorus is brought down to the acceptable limit by careful removal of the floating slag.

Similarly, calcium carbide is added into ferronickel to remove sulfur as calcium sulfide. However, lime, calcium carbonate, sodium carbonate, and sodium peroxide may also be added to remove sulfur. Oxygen is injected into the molten ferronickel to remove impurities such as carbon and silicon. The refined ferronickel is then either granulated or cast into small ferrocones or large ingots [11, 29].

Equations 2.30 - 2.32 present the reactions for phosphorus, sulfur, and carbon removal, respectively [1]:



### 2.2.5 Rotary Kiln Electric Furnace Process (Matte Production)

Occasionally, the RKEF route is employed to produce an iron-nickel sulfide matte. Two primary producers of sulfide matte are PT Inco in Indonesia and Le Nickel in New Caledonia. In the PT Inco process, molten sulfur is added at the discharge end of the rotary kiln to sulfurize the ore (**Figure 2.7**). The exit temperature of sulfurized calcine is 700 °C, and it typically contains 2 % nickel, 20 % iron, and 1 % sulfur. An electric furnace at 1400 °C melts the calcine, and it forms a molten matte containing 26 % nickel, 63 % iron and 10 % sulfur. The recovery of nickel in the matte is usually higher than 93 %. Peirce-Smith converter (**Figure 2.8**) is used to remove iron from the furnace matte. Most of the iron and some sulfur is oxidized by adding silica as flux and blowing oxygen into the converter. The reactions in the Peirce-Smith converter are highly exothermic and requires no external heat. The product from convertor contains 78 % nickel, 1 %

iron, and 20 % sulfur. The matte is solidified into small granules and sent for roasting operations [1, 33].

The sulfurization reaction in the rotary kiln are given by equations 2.33 and 2.34 [1]:



The main reactions in Peirce-Smith converter are given by equations 2.35 and 2.36 [1]:



At Le Nickel, sulfide matte is produced by the conversion of about 20 % of the refined ferronickel. A Peirce-Smith converter is charged with refined ferronickel from the RKEF process along with molten sulfur. A continuous-belt mold caster casts the molten matte into ingots. These ingots are then shipped for chloride leaching to produce high purity nickel chemicals [1].

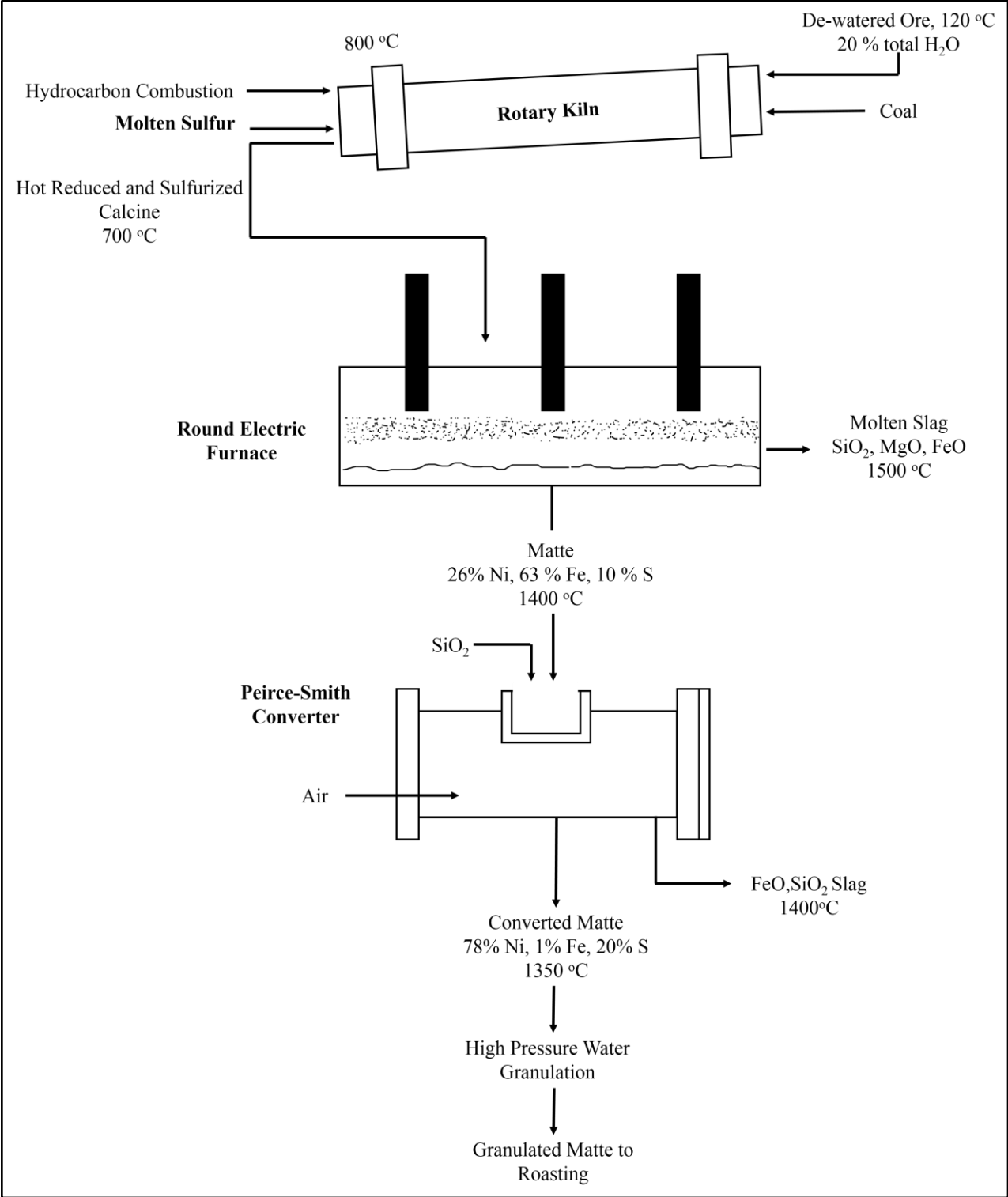


Figure 2.7 PT Inco sulfide-matte smelting flowsheet [1]

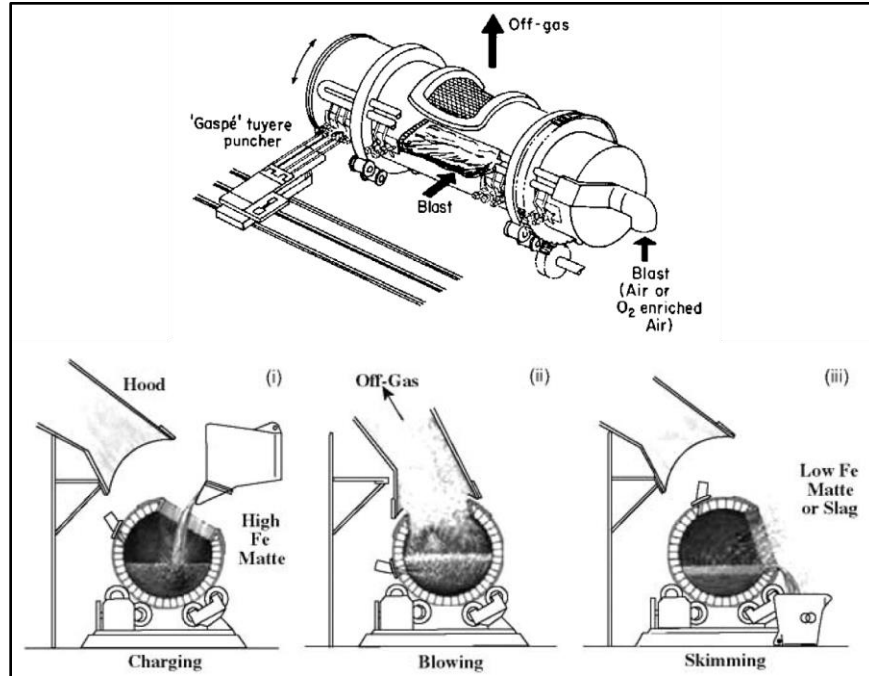


Figure 2.8 Peirce-Smith converter [1]

### 2.2.5.1 Roasting of Sulfide Matte

The sulfide-matte is roasted to eliminate sulfur and produce a product for stainless steel and other industries. The first step is oxidation roasting of sulfide-matte in fluidized-bed roasters to produce a nickel oxide product. This product is then re-roasted in a reducing environment to obtain nickel as metal. The oxidation roasting is carried out in fluidized-bed roasters, typically in two stages: primary and secondary (**Figure 2.9**). The primary step is auto-thermal, where granules of sulfide matte are oxidized by oxygen-enriched air in a highly exothermic reaction. The process is controlled at 1050 °C by water spraying to prevent overheating. The product from the primary oxidation contains 0.4 % sulfur, which is then re-roasted. The secondary roasting is done at 1000 °C and relies on hydrocarbon combustion [1, 34, 35].

The oxidation roasting of sulfide matte is given by equation 2.37:



The final roasted product typically contains 76 % nickel, 23 % oxygen, 0.5 % iron, and 0.003 % sulfur. The product is cooled and sent either for reduction roast to obtain melting grade nickel or sometimes directly sent for stainless steel production. The off-gas is always de-dusted to recycle the nickel-bearing solids to the roaster. The SO<sub>2</sub> in the off-gas is captured and converted into sulfuric acid.

The reduction roasting is done to recover nickel in metallic form. The roaster operates at 1000 °C and is heated by air-deficient hydrocarbon combustion to create a reducing environment. The final product contains 95 - 97 % nickel. The nickel oxide reacts with carbon monoxide and hydrogen and reduces to metallic nickel. The recovery of nickel in oxidation and reduction roasting is almost always 100 % [1].

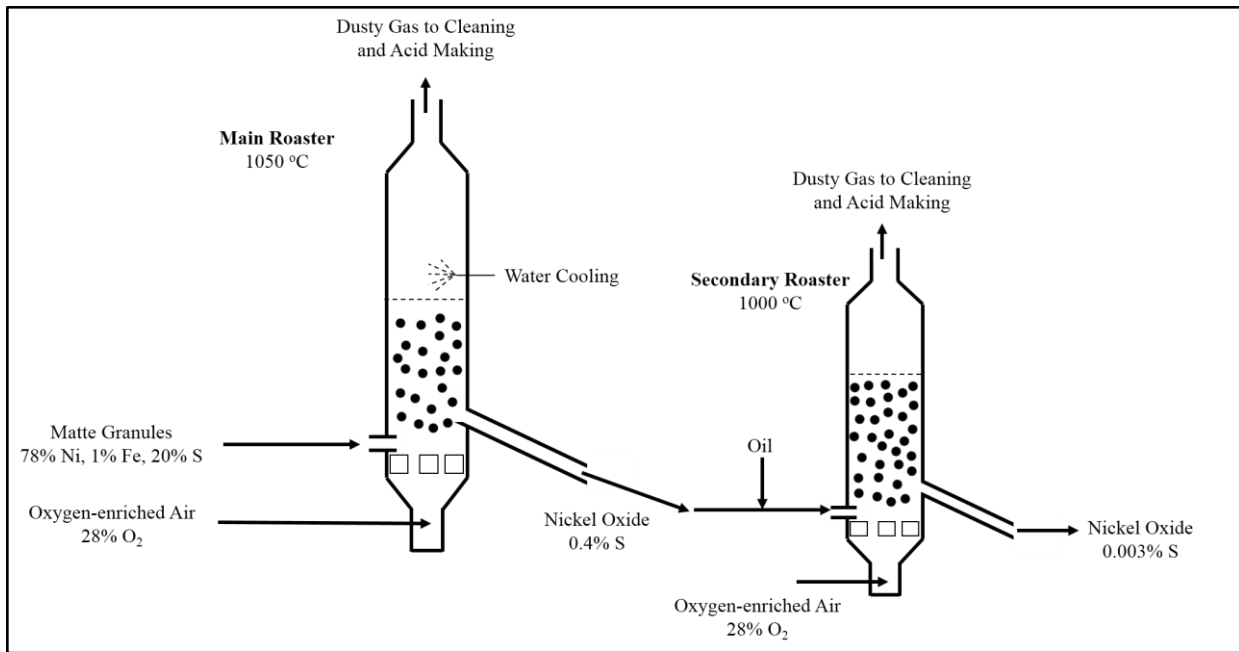


Figure 2.9 Oxidation roasting of sulfide-matte [1]

### 2.3 The Behavior of Laterite Ores in Carbo-Sulfurizing Gas Mixture

There is limited literature available on the behavior of nickel laterites in reducing gas mixtures that contain SO<sub>2</sub>. The most relevant studies have been carried out for bauxite ores to sulfurize hematite in the presence of CO-SO<sub>2</sub> gas mixtures. These studies were aimed at selective removal of iron by sulfurization and subsequent chlorination to improve the aluminum content of bauxite ores. These past studies may be used to understand the behavior of nickel laterites in a reducing atmosphere that contains SO<sub>2</sub>. **Table 2.1** lists the possible sulfurization reactions at 900 °C for iron and nickel oxides in the ore. The highly negative values of ΔG° for Equation 2.38 and 2.39 dictates that, in theory, some of the Fe<sub>2</sub>O<sub>3</sub> and NiO in the ore may sulfurize in the presence of CO-SO<sub>2</sub> gas mixtures.

Table 2.1 Possible sulfurization reactions for Fe<sub>2</sub>O<sub>3</sub> and NiO at 900 °C in CO-SO<sub>2</sub> system

Equation	Reaction	ΔG° <sub>900</sub> (KJ/mol SO <sub>2</sub> )
2.38	$1/2 \text{Fe}_2\text{O}_3 \text{ (s)} + 7/2 \text{CO (g)} + \text{SO}_2 \text{ (g)} = \text{FeS (s)} + 7/2 \text{CO}_2 \text{ (g)}$	-185.4
2.39	$\text{NiO (s)} + 3\text{CO (g)} + \text{SO}_2 \text{ (g)} = \text{NiS (s)} + 3\text{CO}_2 \text{ (g)}$	-186.1

The sulfurization of hematite, to selectively remove iron from minerals was proposed as a beneficiation method for ferruginous bauxite ores. Fink and Marchi (1938) were first to suggest such a procedure when they converted Fe<sub>2</sub>O<sub>3</sub> to FeS by adding elemental sulfur at high temperatures, followed by chlorination of this product to remove 90 % of iron oxides in the ore [37]. Holliday and Milne (1975) explored the possibility of upgrading bauxites by using CO-SO<sub>2</sub> gas mixtures instead of elemental sulfur. They found rapid sulfurization rates at 720 °C for a 7:3 CO-SO<sub>2</sub> gas mixture. The iron level was 5.3 % initially; however, it was brought down to approximately 0.1 - 0.3 % after chlorination of FeS to FeCl<sub>3</sub> [38].

Bolsaitis and Nagata (1980) studied the kinetics of gas-solid reactions between Fe<sub>2</sub>O<sub>3</sub> and CO-SO<sub>2</sub> gas mixtures by thermogravimetric analysis (TGA). The temperature range for the study was between 500 - 900 °C, and the composition of CO-SO<sub>2</sub> mixtures were between X<sub>CO</sub> = 0.4 - 0.92 (where X is the gas molar ratio). The sample size was about 0.2 g, and the gas flow rate was 1130 ml/min (STP). The overall conversion of Fe<sub>2</sub>O<sub>3</sub> to FeS was given by a reduction and sulfurization process. The dominant sulfurizing agents were found to be S<sub>2</sub> and COS, and the kinetic behavior of both species were found to be very similar [39]. The authors summarized the chemical reactions in the system by the following equations:

a) Gas-phase equilibria:



b) Reduction of hematite to magnetite as given by Eq 2.23

c) Sulfurization of magnetite by S<sub>2</sub> and COS:

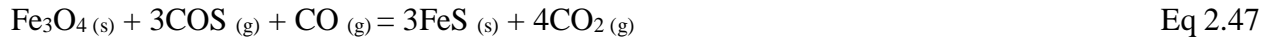


**Figure 2.10** shows equilibrium partial pressures of each constituent in the CO-SO<sub>2</sub> system. The most pronounced change in partial pressures of S<sub>2</sub> and COS occur over the range of X<sub>CO</sub> = 0.6 - 0.8. At X<sub>CO</sub> ≤ 0.4, S<sub>2</sub> is the only dominant sulfurizing agent, while at X<sub>CO</sub> ≥ 0.92, COS is the most dominating species. It is noteworthy that, at X<sub>CO</sub> ≲ 0.8, hematite will only reduce to magnetite, while for higher X<sub>CO</sub>, further reduction to wustite may happen.

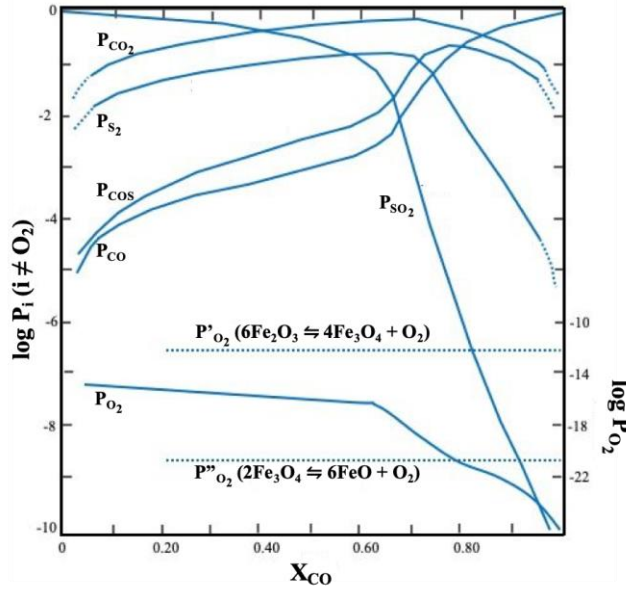


Figure 2.10 Equilibrium partial pressure of gaseous components at 700 °C in CO-SO<sub>2</sub> system of various compositions [39]

**Figure 2.11** shows TGA curves at 700 °C for various gas compositions. The most important feature of this diagram is the virtually similar curves obtained for  $X_{CO}$  between 0.57 to 0.77. As discussed earlier, in this region, the most noticeable changes in  $P_{S_2}$  and  $P_{COS}$  occur. Hence, it may be concluded that both  $S_2$  and  $COS$  are active sulfurizing agents. In general, for all curves, an initial weight decrease corresponding to the reduction of hematite to magnetite can be observed, which is followed by an increase in weight representing the conversion of magnetite to  $FeS$ . At  $X_{CO} = 0.4$ , a decrease is observed in the rate of reduction, sulfurization, and overall conversions. At  $X_{CO} = 0.92$ , four distinct features are found in the curve [39]:

- 1) A swift reduction region that proceeds beyond  $Fe_3O_4$  and indicates possible conversion to wustite as given by Eq 2.24
- 2) A region dominated by simultaneous reduction - sulfurization reactions
- 3) A region dominated by sulfurization reaction

4) The slope for sulfurization region is very similar to the slope observed for  $X_{CO} = 0.4$ ; which further explains that  $S_2$  and  $COS$  have very similar sulfurization activity

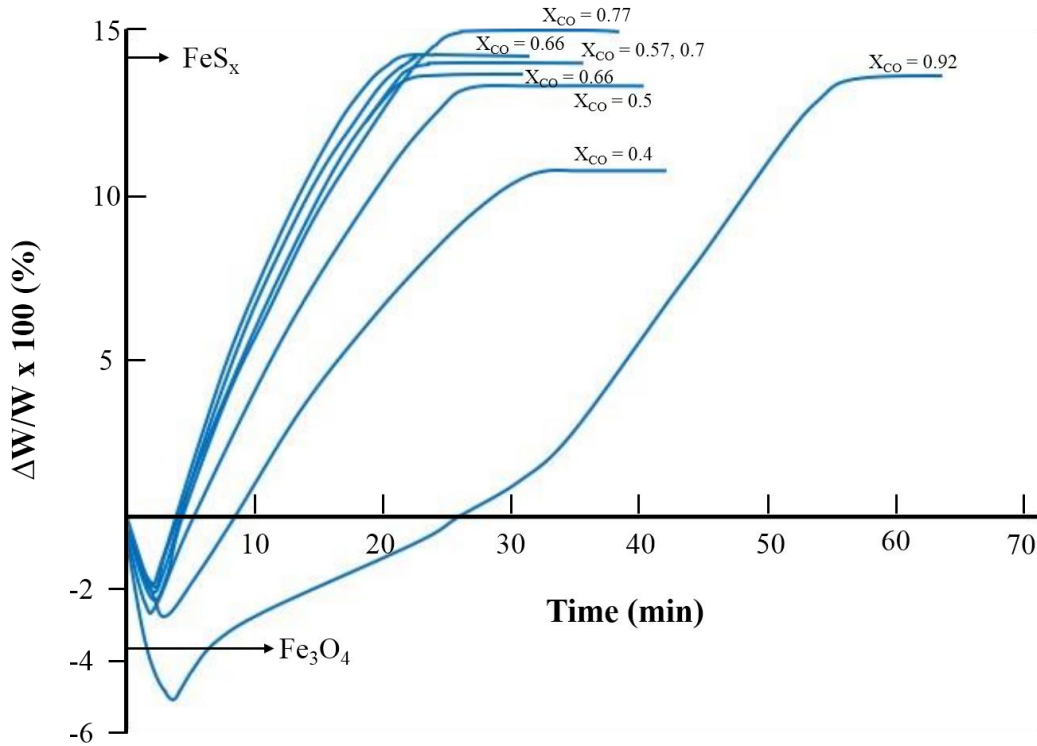


Figure 2.11 TGA curves of  $Fe_2O_3$  samples at  $700\text{ }^\circ\text{C}$  in  $CO-SO_2$  atmosphere with various compositions [39]

**Figure 2.12** shows the TGA curves at  $X_{CO} = 0.66$  for various temperatures. At a temperature of  $600\text{ }^\circ\text{C}$  and above, authors found a rapid reduction of hematite followed by nucleation and growth of the sulfide phase. At a temperature of  $550\text{ }^\circ\text{C}$ , both reduction and sulfurization take place simultaneously and at considerably lower rates. Almost negligible reduction occurred at  $500\text{ }^\circ\text{C}$ , and hematite was sulfurized directly to  $FeS$  at a prolonged rate. In the light of the above kinetic analysis and morphological observations, the authors concluded that the rate-controlling step of the overall carbo-sulfurization process is the diffusion of  $S_2$  and  $COS$  through  $FeS$  crystals.

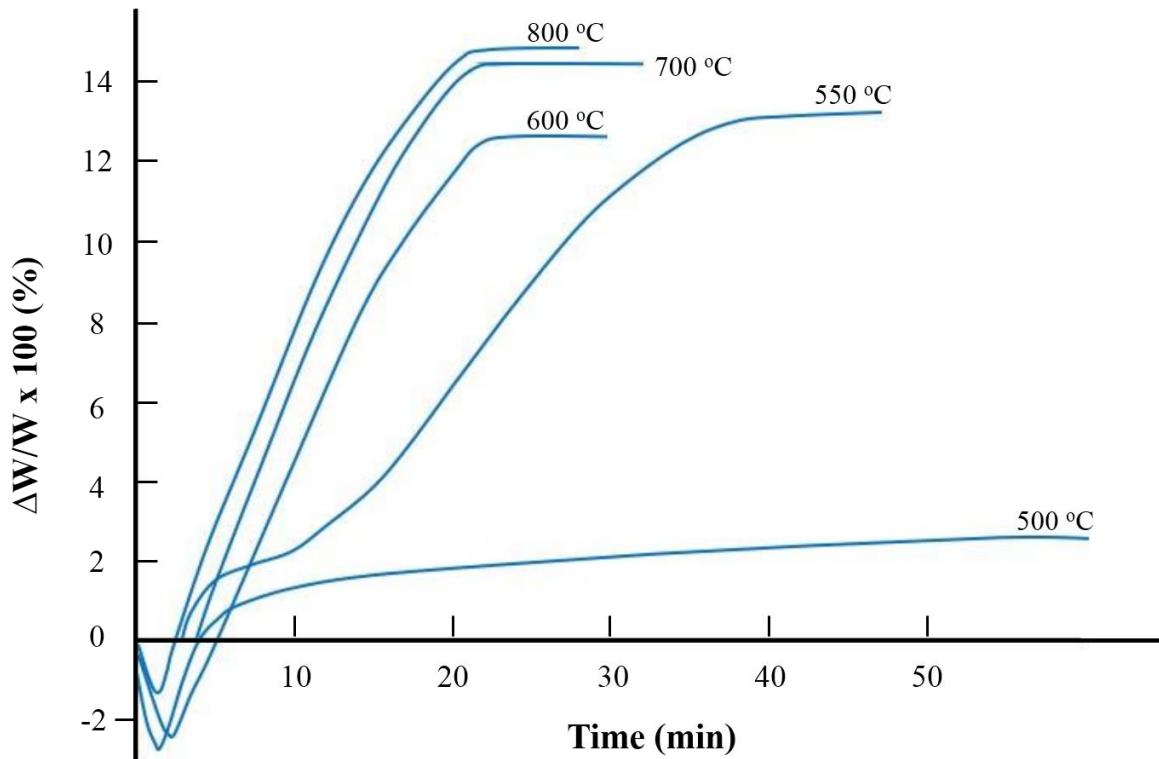


Figure 2.12 TGA curves of  $\text{Fe}_2\text{O}_3$  samples at  $X_{\text{CO}} = 0.66$  for various temperatures [39]

Nagata and Bolsaitis (1987) conducted a similar study for hematite contained in a laterite ore and compared the results with those obtained for pure hematite. The TGA curves at 700 °C (**Figure 2.13**) were plotted for CO-SO<sub>2</sub> system of various compositions. The laterite ore was composed of 25.9 % Al<sub>2</sub>O<sub>3</sub>, 38.5 % Fe<sub>2</sub>O<sub>3</sub>, 31.3 % SiO<sub>2</sub>, and 4.6 % TiO<sub>2</sub>. The time for sulfide nucleation was similar in both cases; however, no reduction was observed in the case of the laterite. The absence of reduction was attributed to the inhibition of magnetite nucleation, possibly due to impurities in hematite grains. Furthermore, the rates of sulfurization were found to be faster for laterite samples, probably because of the higher specific surface area [40].

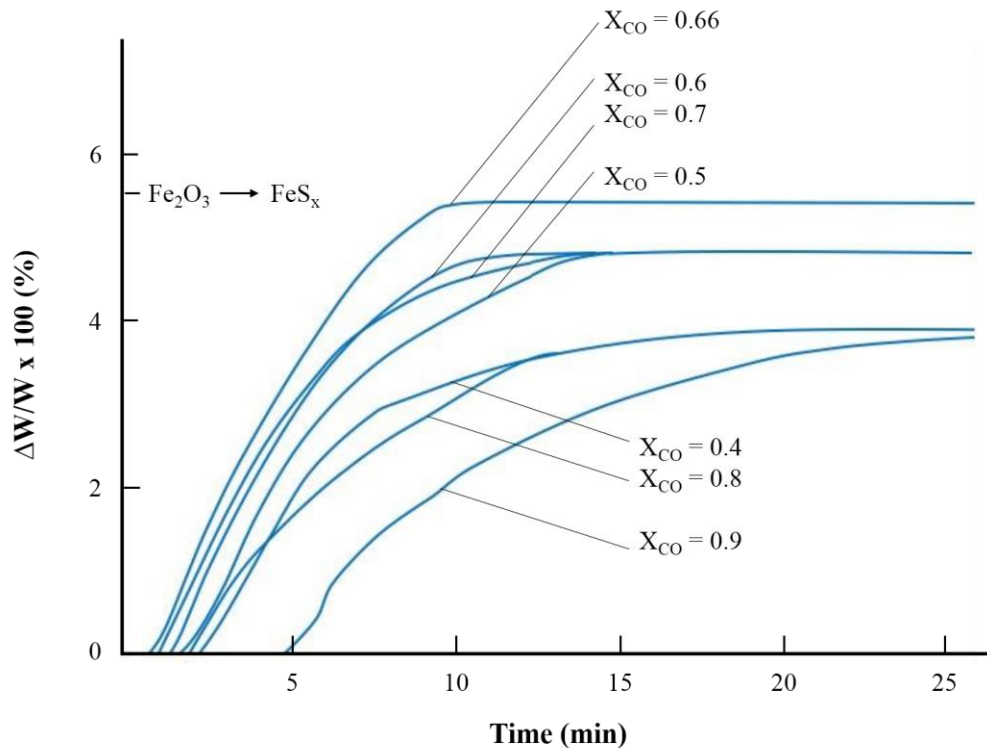


Figure 2.13 TGA curves of laterite samples at 700 °C in CO-SO<sub>2</sub> system of various composition [40]

Previous studies on reduction-sulfurization of iron oxides were conducted with an ultimate goal of selective removal of iron from various minerals such as bauxite or ilmenite to increase valuable metal content of the ore. It should be noted that the partial pressure of SO<sub>2</sub> in these studies were significantly higher than the ones generated from oxidation of the sulfur as an impurity element in the fuel. This study investigates the effect of the presence of low SO<sub>2</sub> content in the furnace atmosphere, on the sulfur content of the calcine.

## 2.4 Scope and Objectives

Sulfur is one of the most harmful impurities in nickel products. It can form non-metallic inclusions, which deteriorates the mechanical properties of the alloy [41]. Crude ferronickel from the RKEF process may contain up to 1 % sulfur, which is significantly higher than the desired range of 0.05 % sulfur in the final ferronickel product [14]. Generally, a ladle furnace is used to

remove sulfur from crude ferronickel by adding reagents such as calcium carbide. As discussed earlier, using calcium carbide imposes an additional reagent cost which will affect the economics of the process.

Typically, laterite ores contain an insignificant amount of sulfur [42], so it is expected that most of the sulfur in crude ferronickel originates from the coal added as the fuel and the reductant during calcination in the rotary kiln. The slim profits of RKEF process are pushing producers to use low-quality coals, which generally contains high concentrations of sulfur [15]. It is hypothesized that during calcination of laterites in the rotary kiln, sulfur present as an impurity in the rotary kiln fuel is oxidized and transferred to the calcine. Therefore, there is a need to study the effect of sulfur in the rotary kiln fuels on the sulfur content of the calcine.

The main objectives of this study are to examine the following:

- The effect of the composition of the coal added as rotary kiln fuel on the composition of the calcine.
- The effect of the kiln atmosphere (e.g.,  $P_{CO}$ ,  $P_{CO_2}$ ) on the composition of the calcine.
- The effect of the flow rate of the reducing gas mixture on the composition of the calcine.

## Chapter 3: Materials and Methods

### 3.1 Materials

The laterite ore used in this study was provided by FLSmidth and was originally obtained from a Brazilian deposit. Coal was added as a reductant in each experiment and was obtained from the Coal and Mineral Processing Laboratory at UBC. Following reagents were used in digestion of the calcine: Potassium hydroxide (KOH, 89 % purity, VWR chemicals), nitric acid (HNO<sub>3</sub>, 69.7 % purity, VWR chemicals), Methanol (CH<sub>3</sub>OH, 99.8 % purity, VWR chemicals), and Bromine (Br, 99.8 % purity, Alfa Aesar).

### 3.2 Characterization of Raw Materials

The chemical assay of the raw ore was determined by Bureau Veritas Minerals (BVM) in Vancouver and is given in **Table 3.1**. The test sample was dried at 105 °C to remove free moisture before being fused in a platinum crucible with lithium tetraborate flux. The fused sample was cast in a disc and was analyzed by x-ray fluorescence (XRF) to determine the percentage of each component in the raw ore. Another portion of the test sample was roasted at 1000 °C to determine the loss on ignition (LOI). The mineralogy of the raw ore was determined by x-ray diffraction (XRD) using Bruker D8 Focus Diffractometer with CoK $\alpha$  radiation source within the range of 2 $\theta$  values of 3° to 80°. Based on the XRD results presented in **Figure 3.1**, the major crystalline phases in the raw ore are identified as nontronite, lizardite, doyleite, goethite, quartz, trevorite, and hematite. The ore is characterized as a mixture of smectite and saprolite due to the presence of nontronite and lizardite, as well as the relatively low magnesia content.

The proximate analysis of coal was carried out according to ASTM standards D3175, D3174, and D3173, to determine volatiles, ash, and moisture contents, respectively. The fixed

carbon was found by difference. The total carbon and sulfur contents were determined using LECO analysis. The chemical composition of coal is given in **Table 3.2**.

Table 3.1 Chemical assay of the raw ore

Component	Wt. %
Fe <sub>2</sub> O <sub>3</sub>	34.6
SiO <sub>2</sub>	36.7
MgO	8.74
Al <sub>2</sub> O <sub>3</sub>	5.88
Cr <sub>2</sub> O <sub>3</sub>	1.62
TiO <sub>2</sub>	0.1
CaO	0.03
P <sub>2</sub> O <sub>5</sub>	0.013
K <sub>2</sub> O	<0.005
Ni	1.87
Co	0.118
Cu	0.01
Zn	0.045
LOI	9.3

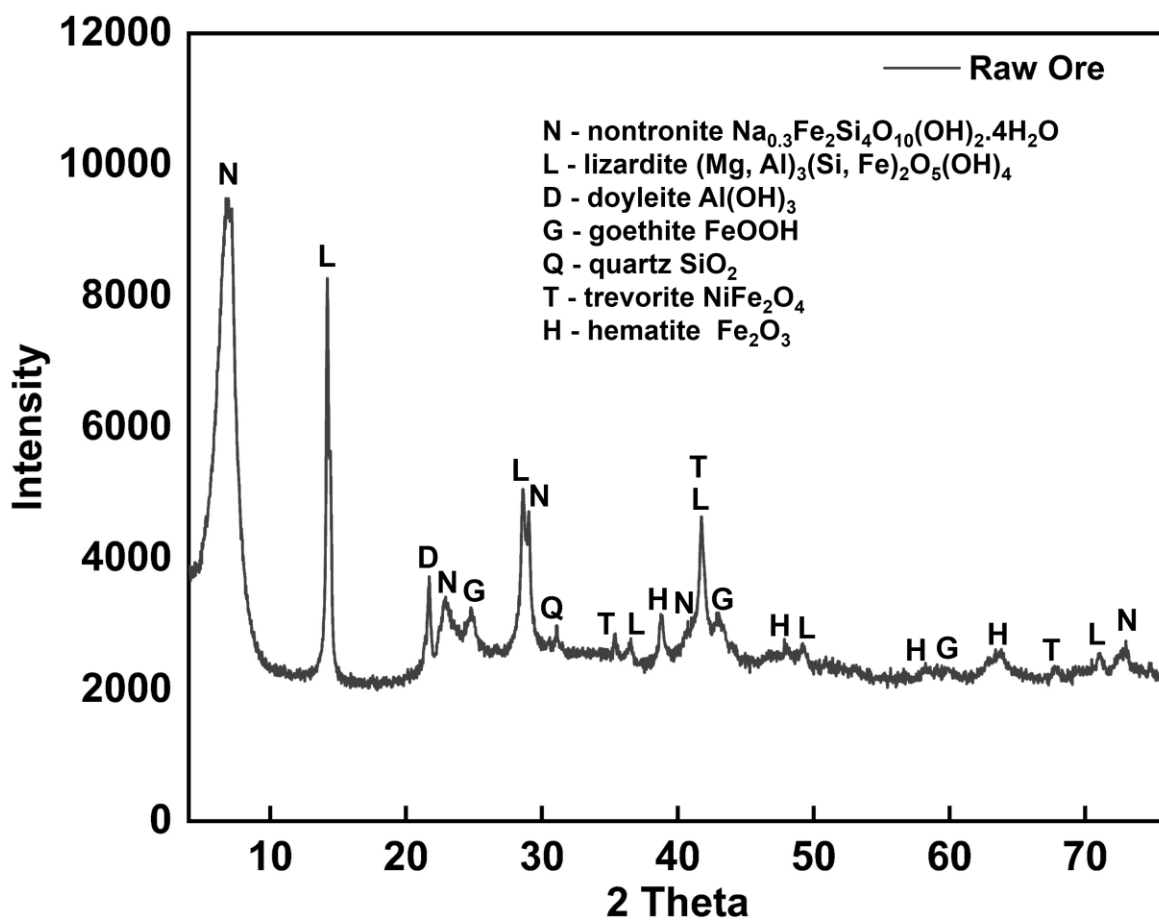


Figure 3.1 XRD pattern of the raw ore

Table 3.2 Composition of the coal added as the reductant

Component	Wt. %	Test Method
Volatile Matter	25.34	ASTM D3175
Ash	7.08	ASTM D3174
Moisture	2.76	ASTM D3173
Fixed Carbon	64.82	By Difference
Total Carbon	77.74	LECO
Total Sulfur	0.43	LECO

### 3.3 Preliminary Processing of the Raw Materials

The as-received laterite ore was dried in an oven, shown in **Figure 3.2 a**, at 70 °C for 24 hours to remove free moisture. The free moisture was found to be 29 % in the raw ore. The ore (3 kg) and the coal (500 g) were ground in a Fritsch Pulverisette Mortar Grinder Mill (shown in **Figure 3.2 b**) separately for 4 minutes. A sieve of 300 µm opening (no. 50 mesh size) was used to screen the ground material. Any oversize material was crushed again until 100 % of the sample passed through the sieve. **Figure 3.3 a-d** shows the as-received, dried, and ground ore, as well as ground coal, respectively. The particle size distribution analysis was carried out by dry-sieving 200 g of ore through a sieve stack with the following screen openings (µm): 710, 600, 500, 425, 300, 212, 180, 125 and 75. **Figure 3.4** shows the particle size distribution of the ore, and it is evident that 80 % of the ground ore was smaller than 212 µm ( $P_{80} = 212 \mu\text{m}$ ). The feed samples for experiments were prepared by mixing 50 g of ground ore with 5 g of coal and were stored in polymer containers sealed with parafilm before calcination and high-temperature experiments.

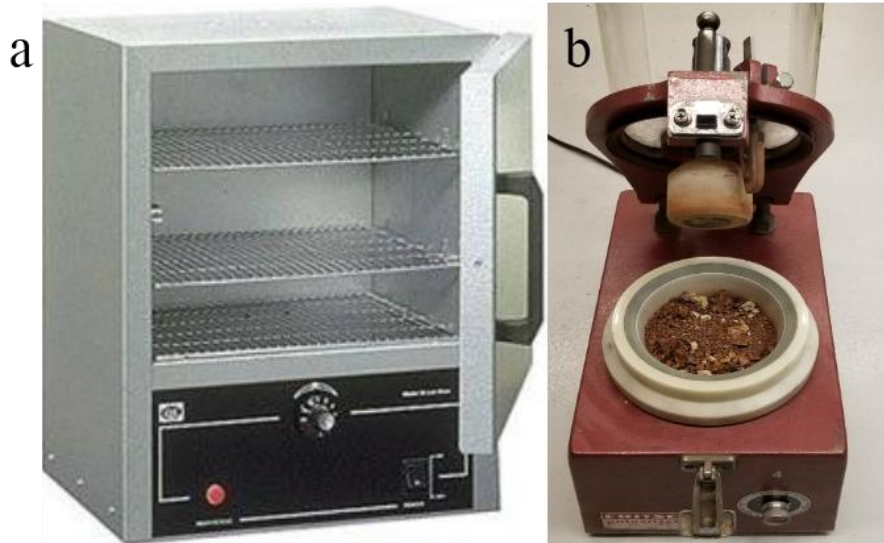


Figure 3.2 (a) Oven (b) Mortar grinder mill



Figure 3.3 (a) As-received ore (b) Dried ore (c) Ground ore (d) Ground coal

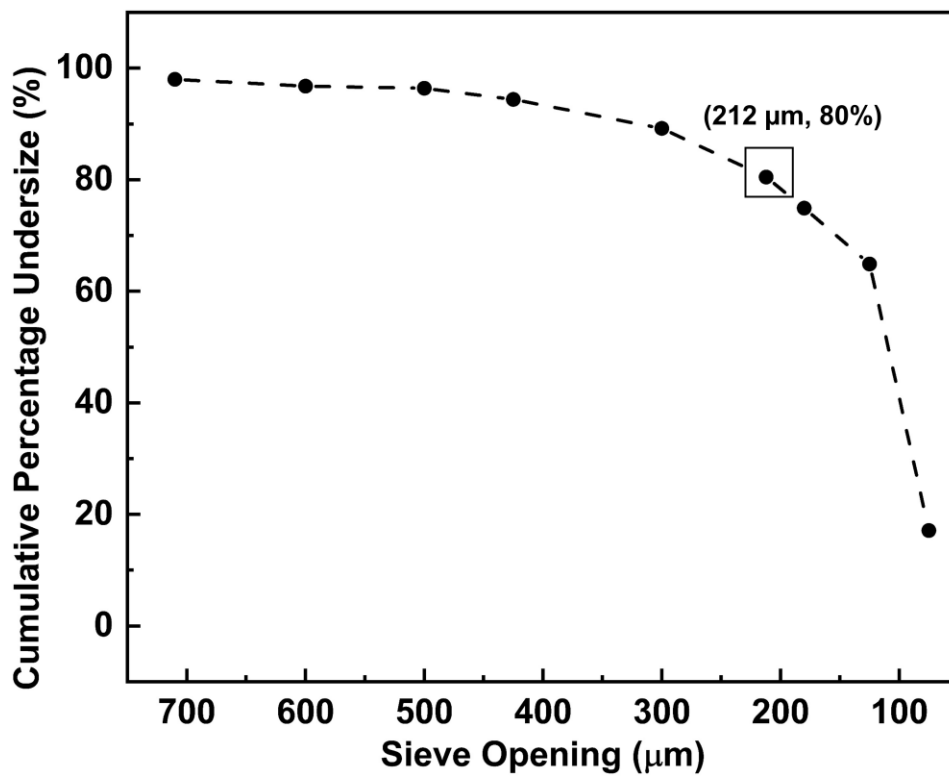


Figure 3.4 Particle size distribution of the ground ore

### 3.4 Calcination and Partial Reduction Experiments

A Nabertherm RSRB 80 - 750/11 furnace was used to conduct all the experiments. The furnace had a 1400 mm long quartz reactor with tapered ends. The heated zone of the reactor was 750 mm in length and 76 mm in diameter. An additional thermocouple was used once to determine the proximity of temperature inside the reactor and the one shown by the furnace controller. **Figure 3.5** shows that both temperatures were reasonably close during the complete heat cycle up to a maximum temperature of 700 °C.

A gas supply system was designed and connected to the furnace to provide a mixture of following gases: carbon monoxide (CO), carbon dioxide (CO<sub>2</sub>), nitrogen (N<sub>2</sub>), and sulfur dioxide (SO<sub>2</sub>). Alicat Scientific gas mass flow controllers (MC and MCS series) were used to inject the desired amount of each gas into the furnace. The MC series controllers are suitable to handle non-corrosive gases, i.e., CO, CO<sub>2</sub>, and N<sub>2</sub>, while MCS series controllers are built with special materials to handle corrosive gases, e.g., SO<sub>2</sub>. The gases through the mass controllers were mixed in a cylindrical column filled with glass beads to achieve a homogenous mixture as the input reducing gas. A ceiling-mounted extraction arm was used to collect the exit gases on the other end of the furnace. The level of hazardous gases inside the lab was continuously monitored by alarm devices to avoid any safety incidents. **Figure 3.6** shows the gas injection setup for the furnace experiments. **Figure 3.7 a** and **b** show the complete experimental setup and quartz reactor, respectively.

The prepared feed samples composed of 50 g of the ore and 5 g of coal were fed to the quartz reactor at room temperature. The feed was heated to 900 °C at 450 °C/hour under a neutral atmosphere. The neutral atmosphere inside the reactor was maintained by flowing 1 L/min of N<sub>2</sub> at room temperature for 15 min and then 200 ml/min of N<sub>2</sub> during ramp-up. The feed was kept at 900 °C for 2 hours in the presence of a CO-CO<sub>2</sub>-SO<sub>2</sub>-N<sub>2</sub> gas mixture followed by cooling to room

temperature under neutral atmosphere. The total flow rate of the gas mixture was kept constant at 292 ml/min. The flow rates of individual gases were varied to simulate the combustion product of rotary kiln fuels. **Table 3.3** lists the experiments and their parameters when the total flow rate of the reducing gas mixtures was 292 ml/min. Experiments 13 - 18 presented in **Table 3.3** were repeated by lowering the total flow rate of the input gas mixtures from 292 to 176 ml/min for constant calcination time of 2 hours. The modified flow rates for individual gases are presented in **Table 3.4**. The overall temperature cycle for furnace experiments is shown in **Figure 3.8**.

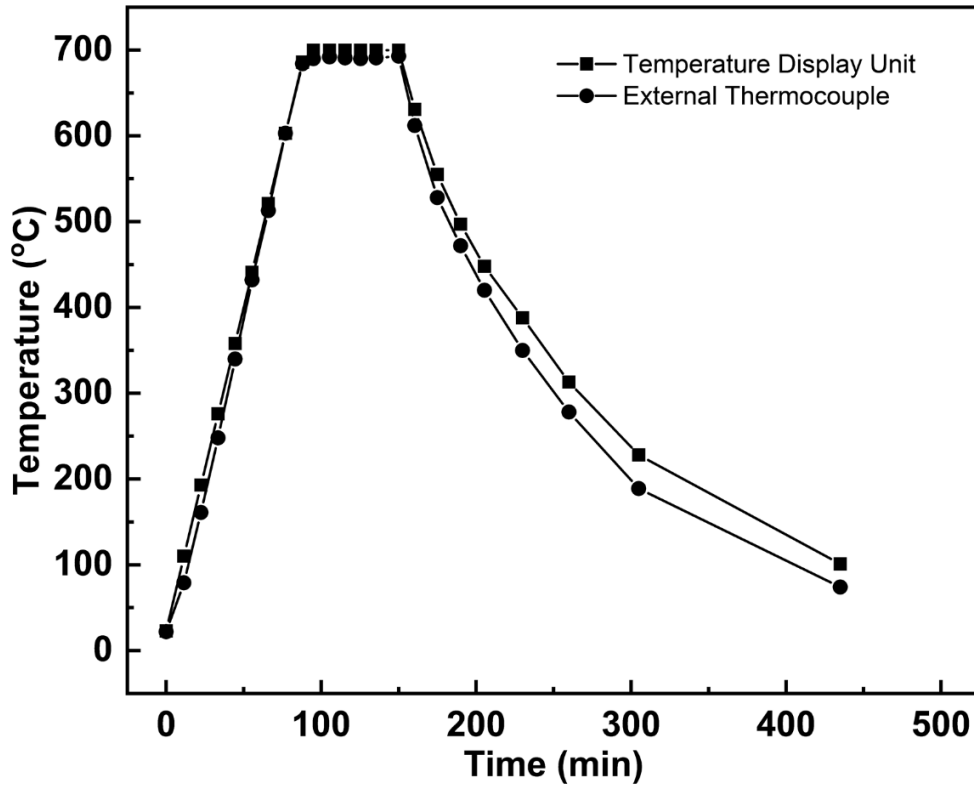


Figure 3.5 Furnace temperature calibration by comparing the values obtained from internal and external thermocouple

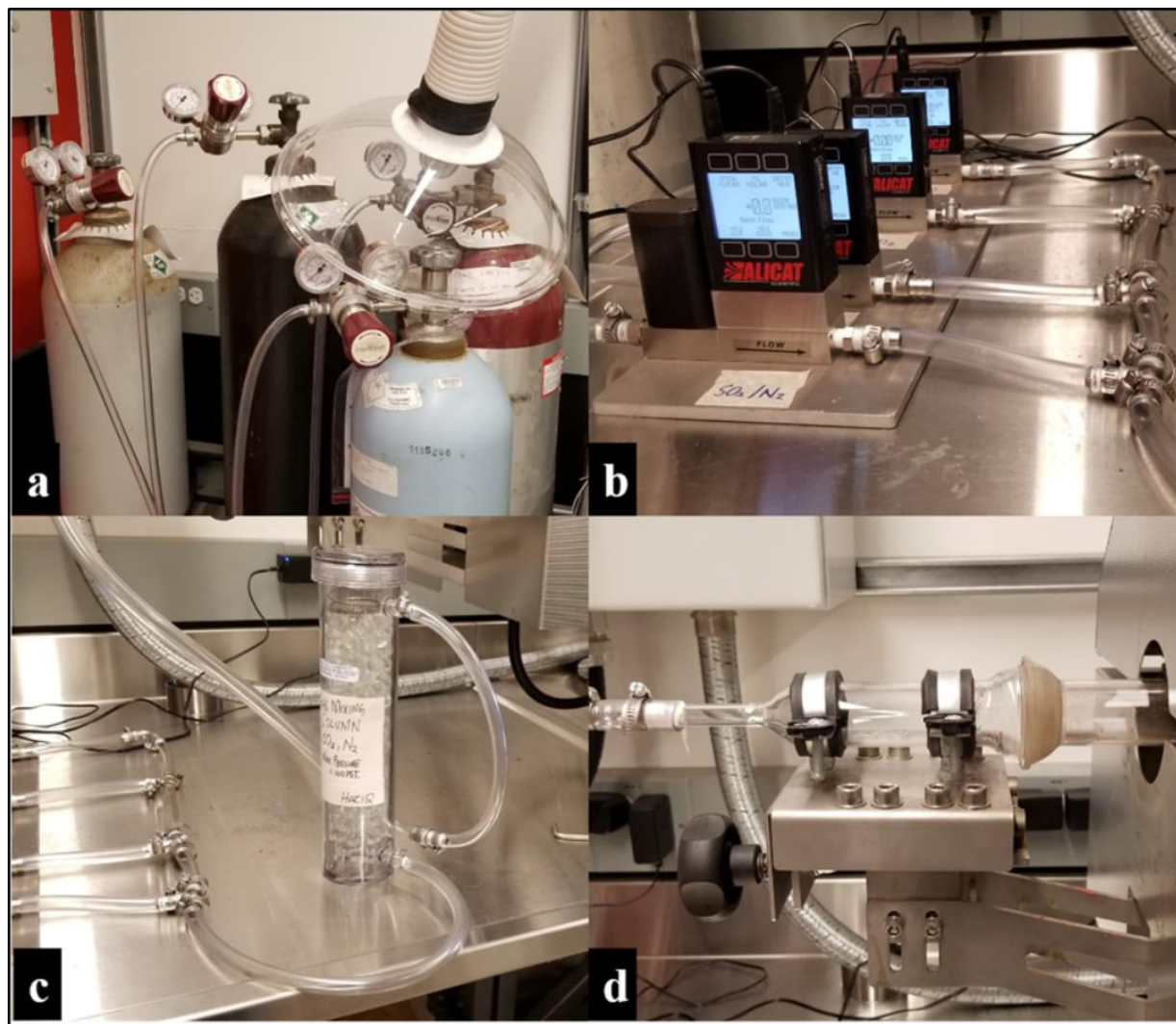


Figure 3.6 (a) Gas cylinders (b) Mass flow controllers (c) Gas mixing column (d) Gas inlet to the furnace

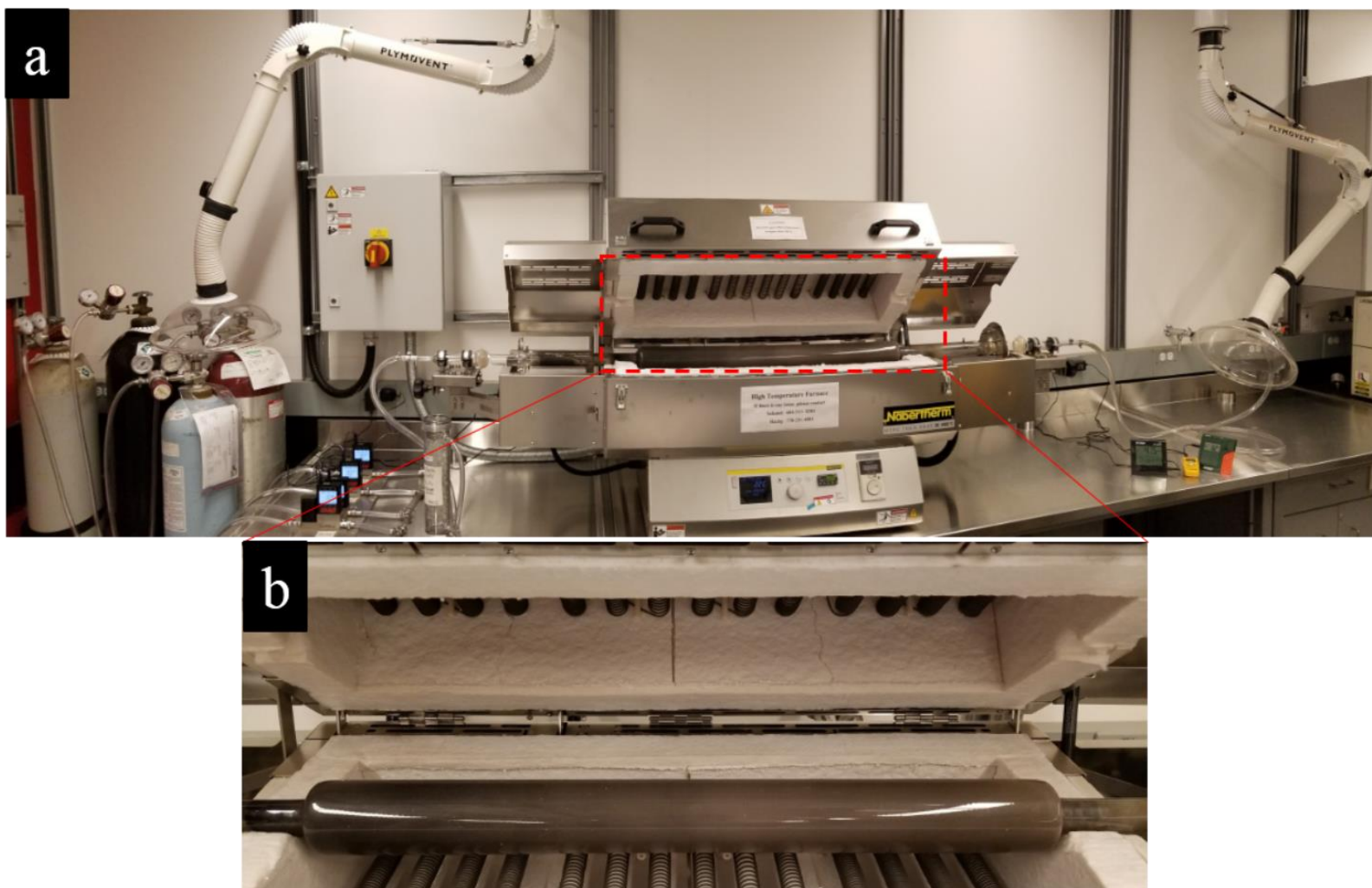


Figure 3.7 (a) Complete experimental setup (b) Quartz reactor

Table 3.3 The gas flow rates for the calcination and partial reduction experiments at 900 °C and 2-hour residence time with total input flow rate of 292 ml/min

Experiment No.	CO/CO <sub>2</sub>	CO (ml/min)	CO <sub>2</sub> (ml/min)	SO <sub>2</sub> (ml/min)	N <sub>2</sub> (ml/min)	P <sub>CO</sub> (atm)	P <sub>SO<sub>2</sub></sub> (atm)
1	60/40	112	74	0	106	0.39	0
2		112	74	2.1	103.9	0.39	0.0072
3		112	74	4.2	101.8	0.39	0.0144
4		112	74	6.4	99.6	0.39	0.0216
5		112	74	8.5	97.5	0.39	0.0288
6		112	74	10.6	95.4	0.39	0.0360
7	70/30	131	56	0	106	0.45	0
8		131	56	2.1	103.9	0.45	0.0072
9		131	56	4.2	101.8	0.45	0.0144
10		131	56	6.4	99.6	0.45	0.0216
11		131	56	8.5	97.5	0.45	0.0288
12		131	56	10.6	95.4	0.45	0.0360
13	80/20	149	37	0	106	0.51	0
14		149	37	2.1	103.9	0.51	0.0072
15		149	37	4.2	101.8	0.51	0.0144
16		149	37	6.4	99.6	0.51	0.0216
17		149	37	8.5	97.5	0.51	0.0288
18		149	37	10.6	95.4	0.51	0.0360
19	90/10	168	19	0	106	0.57	0
20		168	19	2.1	103.9	0.57	0.0072
21		168	19	4.2	101.8	0.57	0.0144
22		168	19	6.4	99.6	0.57	0.0216
23		168	19	8.5	97.5	0.57	0.0288
24		168	19	10.6	95.4	0.57	0.0360
25	100/0	187	0	0	106	0.63	0
26		187	0	2.1	103.9	0.63	0.0072
27		187	0	4.2	101.8	0.63	0.0144
28		187	0	6.4	99.6	0.63	0.0216
29		187	0	8.5	97.5	0.63	0.0288
30		187	0	10.6	95.4	0.63	0.0360

Table 3.4 The gas flow rates for the calcination and partial reduction experiments at 900 °C and 2-hour residence time with total input flowrate of 176 ml/min

Experiment No.	CO/CO <sub>2</sub>	CO (ml/min)	CO <sub>2</sub> (ml/min)	SO <sub>2</sub> (ml/min)	N <sub>2</sub> (ml/min)	P <sub>CO</sub> (atm)	P <sub>SO<sub>2</sub></sub> (atm)
31		89.7	22.3	0	63.62	0.51	0
32		89.7	22.3	1.27	62.35	0.51	0.0072
33	80/20	89.7	22.3	2.54	61.08	0.51	0.0144
34		89.7	22.3	3.81	59.81	0.51	0.0216
35		89.7	22.3	5.08	58.54	0.51	0.0288
36		89.7	22.3	6.35	57.27	0.51	0.0360

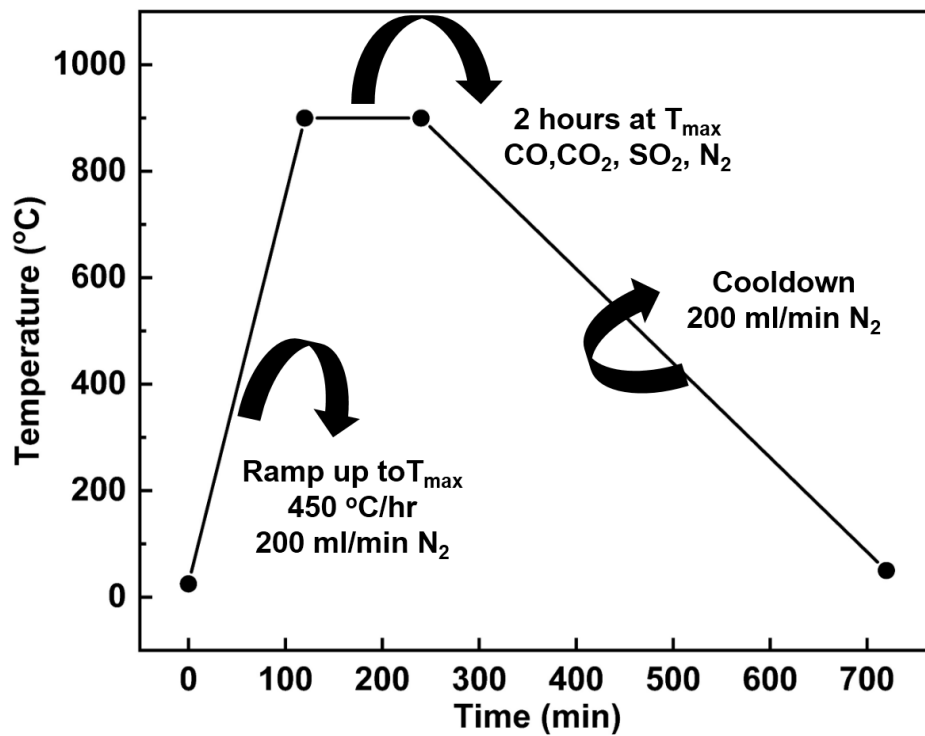


Figure 3.8 Temperature cycle for calcination and partial reduction experiments

### 3.5 Chemical Analysis

#### 3.5.1 Inductively Coupled Plasma - Atomic Emission Spectroscopy

Inductively Coupled Plasma - Atomic Emission Spectroscopy (ICP-AES) was used to measure the concentration of sulfur, iron, and nickel in the calcine. The calcine was first ground in a ball mill grinder for 15 minutes (**Figure 3.9**). Since silicates are not acid-soluble, an alkali salt fusion process was carried out at high temperature to achieve near-total digestion. Approximately 0.2 g of ground calcine was mixed with 3 g of potassium hydroxide (KOH) and added into a zirconium crucible. The crucible was covered with a lid and heated in a muffle furnace (**Figure 3.10**) to a temperature of 500 °C for 1 hour. After heating, the crucible was allowed to cool to room temperature in a desiccator to avoid exposure to air and humidity. 100 ml of 6 M nitric acid was used to digest the fused calcine. The solution was filtered using Whatman No.1 cellulose filters. **Figure 3.11** shows reduced calcine, KOH pellets, zirconium crucible, and leached solution after filtration, respectively. A Varian 725-ES ICP spectrometer was used to analyze the solution. The concentration of sulfur was measured directly by analyzing 10 ml of the leached solution. The equation for the conversion of sulfur concentration in the solution (mg/L) to the concentration in the solid calcine (wt. %) is given below:

$$C_{\text{sulfur}} (\text{wt.}\%) = \frac{C_{S \text{ in solution}} \left( \frac{\text{mg}}{\text{L}} \right) \times V_{\text{solution}} (\text{L})}{W_{\text{digested calcine}} (\text{mg})} \times 100 \quad \text{Eq 3.1}$$

Where  $C_{S \text{ in solution}}$  is the concentration of sulfur in the leach solution measured by ICP-AES,  $V_{\text{solution}}$  is the total volume of the solution (i.e., 100 ml), and  $W_{\text{digested calcine}}$  is the mass of calcine digested in the solution (i.e., 0.2 g).

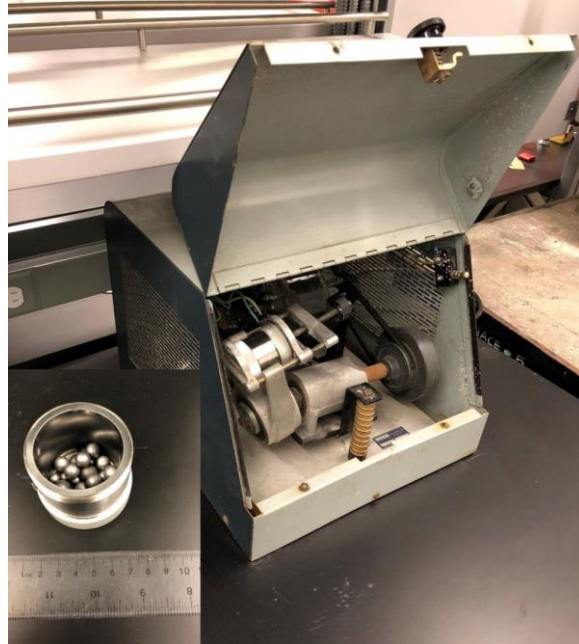


Figure 3.9 Ball mill grinder



Figure 3.10 Muffle furnace

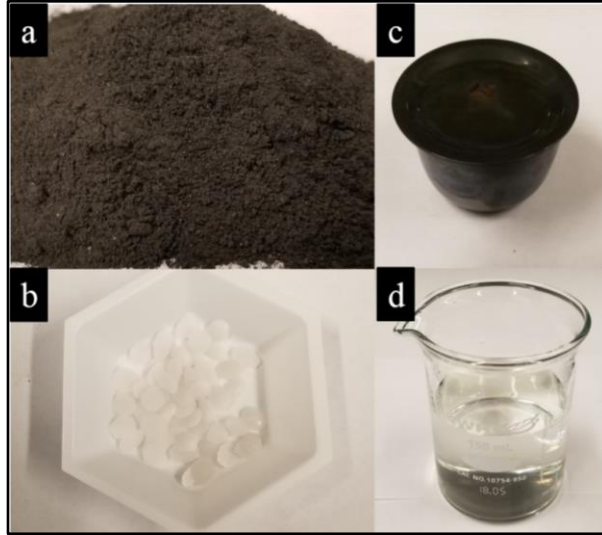


Figure 3.11 (a) Reduced calcine (b) KOH pellets (c) Zirconium crucible (d) Leached solution

The leach solution was diluted 20 times by adding 0.5 ml solution into 9.5 ml of 6 M nitric acid. The total iron and nickel concentration were measured by testing the resulting solution. The equation for the conversion of iron and nickel concentration in the solution (mg/L) to the total concentration in the solid calcine (wt.%) is given below:

$$C_{\text{Fe/Ni}} (\text{wt.}\%) = \frac{C_{\text{Fe/Ni in solution}} \left( \frac{\text{mg}}{\text{L}} \right) \times V_{\text{solution}} (\text{L})}{W_{\text{digested calcine}} (\text{mg})} \times F_{\text{dil}} \times 100 \quad \text{Eq 3.2}$$

Where  $C_{\text{Fe/Ni in solution}}$  is the concentration of iron or nickel in the leach solution,  $V_{\text{solution}}$  is the total volume of the solution (i.e., 100 ml),  $W_{\text{digested calcine}}$  is the mass of calcine digested in the solution (i.e., 0.2 g), and  $F_{\text{dil}}$  is the dilution factor (i.e., 20).

The bromine-methanol leach was used to determine the sum of nickel/iron present as metallic and sulfide form in the calcine. The bromine-methanol leach is very selective to dissolve pure metals and sulfides but does not dissolve oxides [32]. Calcined samples weighing 0.25 g were added into 50 ml of the 5 % bromine - 95 % methanol solution and stirred for 20 min at room temperature. The solution was then filtered using Whatman No.1 cellulose filters. The filter paper

was washed with 50 ml of deionized water. The filtrate was then diluted by adding 3 ml of solution into 47 ml of deionized water. The iron and nickel concentration were measured by testing 10 ml of the resulting solution. The equation for the conversion of concentration of iron and nickel in the solution (mg/L) to the sum of metallic and sulfurized iron/nickel in the solid calcine (wt.%) is given below:

$$C_{\text{metallic \& sulfide (wt.\%)}} = \frac{C_{\text{Fe/Ni in solution}} \left(\frac{\text{mg}}{\text{L}}\right) \times V_{\text{solution}}(\text{L})}{W_{\text{digested calcine}}(\text{mg})} \times F_{\text{dil}} \times 100 \quad \text{Eq 3.3}$$

Where  $C_{\text{Fe/Ni in solution}}$  is the concentration of iron or nickel in the bromine - leach solution,  $V_{\text{solution}}$  is the total volume of the solution (i.e., 100 ml),  $W_{\text{digested calcine}}$  is the mass of calcine digested in the solution (i.e., 0.25 g), and  $F_{\text{dil}}$  is the dilution factor (i.e., 50/3).

The sum of metallic and sulfurized iron/nickel in the calcine is determined by the equation 3.4.

$$\text{Sum of metallic \& sulfurized iron/nickel (\%)} = \frac{C_{\text{Metallic \& sulfide (wt.\%)}}}{C_{\text{Fe/Ni (wt.\%)}}} \times 100 \quad \text{Eq 3.4}$$

### 3.5.2 X-ray Diffraction, Scanning Electron Microscopy and Energy Dispersive X-ray Spectroscopy

The calcine was analyzed by x-ray diffraction (XRD) to characterize its mineralogy. Bruker D8 Focus diffractometer with  $\text{CoK}\alpha$  radiation source collected continuous diffraction data within the range of  $2\theta$  values of  $3^\circ$  to  $80^\circ$ . The X-ray diffractogram was analyzed using the International Centre for Diffraction Database. FEI Quanta with large area EDX was used to study the morphology and elemental composition of the calcine.

## Chapter 4: Thermodynamic Analysis

### 4.1 Model Description

The equilibrium module of HSC Chemistry 6.0 [43] is utilized to estimate the multi-component equilibrium composition of the current system. The input species and their amounts corresponding to the experimental conditions and the expected output species are specified to determine the equilibrium system in the furnace. In these calculations, the activity coefficient values are assumed to be constant and equal to 1. The software utilizes Gibbs energy minimization method to calculate the equilibrium amount of all species at 900 °C [44]. **Table 4.1** lists all the species considered in the thermodynamic simulation.

Table 4.1 List of all the considered species in thermodynamic analysis

Gas	Solids			
	Oxides	Sulfides	Ferronickel	Coal
CO	SiO <sub>2</sub>			
CO <sub>2</sub>	NiO			
N <sub>2</sub>	Fe <sub>2</sub> O <sub>3</sub>			
SO <sub>2</sub>	Fe <sub>3</sub> O <sub>4</sub>	NiS		
S	FeO	NiS <sub>2</sub>	Ni	C
S <sub>2</sub>	Fe <sub>2</sub> SiO <sub>4</sub>	Ni <sub>3</sub> S <sub>2</sub>	Fe	S
SO	FeSiO <sub>3</sub>	FeS		
COS	MgO	FeS <sub>2</sub>		
CS <sub>2</sub>	Mg <sub>2</sub> SiO <sub>4</sub>			
	MgSiO <sub>3</sub>			
	NiFe <sub>2</sub> O <sub>4</sub>			

The input stream consists of raw ore, coal, and a gas mixture containing CO, CO<sub>2</sub>, N<sub>2</sub>, and SO<sub>2</sub> at 900 °C. The mineralogy of the raw ore (**Table 3.1**) and the amounts of the ore and coal selected in the model calculations are the same as the ones used in the actual experiments, i.e., 50 g and 5 g, respectively. Free moisture, crystalline water, and volatiles in the ore and coal are assumed to have already evaporated at elevated temperature. Molar quantities are used to define

all of the input components. The specific amounts of gas for a 2-hour experiment ( $V_{\text{gas,exp}}$ ) are calculated from the flow rates presented in **Table 3.3**. To further elucidate the effect of the total gas volume, modeling calculations are also carried out at lower volumes, i.e., one-fourth ( $1/4 V_{\text{gas,exp}}$ ) and one-eighth ( $1/8 V_{\text{gas,exp}}$ ) of the experimental values. Thermodynamic modeling at various partial pressures of CO and SO<sub>2</sub> ( $P_{\text{CO}}$  and  $P_{\text{SO}_2}$ ) predicts the change in sulfur content of the calcine (% S), nickel and iron grade (i.e., % nickel/iron in the ferronickel alloy), and metallization and sulfurization of iron and nickel.

HSC software was used to obtain equilibrium partial pressures of the input gas mixtures (containing CO, CO<sub>2</sub>, N<sub>2</sub>, and SO<sub>2</sub>) at 900 °C. Four experimental mixtures were studied (Experiments 8, 12, 20, and 24). The initial amount of each gas species was calculated for a 2-hour experiment from the flow rates presented in **Table 3.3**. The results of HSC modeling are shown in **Table 4.2**. It is noticeable that at equilibrium conditions, SO<sub>2</sub> transforms into COS and S<sub>2</sub>, and the partial pressure of COS is significantly higher than S<sub>2</sub>. At constant  $P_{\text{CO}}$ , i.e., experiments 8 and 12 as well as 20 and 24, increasing  $P_{\text{SO}_2}$  enhances the partial pressure of COS. Similarly, at constant  $P_{\text{SO}_2}$ , i.e., experiments 8 and 20 as well as 12 and 24, increasing  $P_{\text{CO}}$  results in higher partial pressure of COS.

**Table 4.3** presents the overall sulfurization reactions for all the oxides and reduced species in the nickel laterite ores. It also shows the reactions associated with the evolution of intermediate gaseous products, i.e., S<sub>2</sub> and COS. Furthermore, it presents the reactions of the original oxides and their reduced forms with the intermediate gas species. Since the COS content of the gas mixture is significantly higher than that of S<sub>2</sub>, sulfurization reactions with COS are expected to be the ones that govern FeS formation. From the thermodynamic point of view, sulfurization of Fe<sub>2</sub>O<sub>3</sub>

and NiO are more favorable than their reduced species. However, the sulfurization of Fe is thermodynamically more favorable than FeO and Fe<sub>3</sub>O<sub>4</sub>.

It should be emphasized that the simulations are based on pure thermodynamic modeling, which does not account for kinetics, since the module used, only minimizes the Gibbs free energy of the system. As a result, kinetics considerations are not accounted for appropriately. This model also does not consider the continuous supply of the gas mixture from outside the system and the removal of the gaseous compounds from the furnace.

Table 4.2 Initial and equilibrium partial pressure of different components of the gas mixtures at 900 °C

<b>Experiment</b>		<b>CO (Vol%)</b>	<b>CO<sub>2</sub> (Vol%)</b>	<b>N<sub>2</sub> (Vol%)</b>	<b>SO<sub>2</sub> (Vol%)</b>	<b>COS (Vol %)</b>	<b>S<sub>2</sub> (Vol%)</b>
<b>8</b>	<b>Initial</b>	38.31	25.43	35.53	0.73	-	-
	<b>Equilibrium</b>	36.44	27.07	35.79	-	0.66	0.04
<b>12</b>	<b>Initial</b>	38.31	25.43	32.57	3.69	-	-
	<b>Equilibrium</b>	29.60	33.78	33.60	-	2.27	0.75
<b>20</b>	<b>Initial</b>	57.26	6.48	35.53	0.73	-	-
	<b>Equilibrium</b>	55.56	8.03	35.70	-	0.69	0.02
<b>24</b>	<b>Initial</b>	57.26	6.48	32.57	3.69	-	-
	<b>Equilibrium</b>	48.71	14.33	33.61	-	2.90	0.45

Table 4.3 Standard Gibbs free energies of the reactions between species containing iron/nickel in the laterite ore and CO-SO<sub>2</sub> atmosphere at 900 °C

<b>Reaction</b>	<b>Overall Sulfurization Reactions</b>	<b><math>\Delta G^{\circ}_{900^{\circ}\text{C}}</math> (KJ/mol SO<sub>2</sub>)</b>
1	$1/2 \text{Fe}_2\text{O}_3 + 7/2 \text{CO} + \text{SO}_2 = \text{FeS} + 7/2 \text{CO}_2$	-185.4
2	$1/3 \text{Fe}_3\text{O}_4 + 10/3 \text{CO} + \text{SO}_2 = \text{FeS} + 10/3 \text{CO}_2$	-167.4
3	$\text{FeO} + 3\text{CO} + \text{SO}_2 = \text{FeS} + 3\text{CO}_2$	- 165.6
4	$\text{Fe} + 2\text{CO} + \text{SO}_2 = \text{FeS} + 2\text{CO}_2$	- 172.7
5	$\text{NiO} + 3\text{CO} + \text{SO}_2 = \text{NiS} + 3\text{CO}_2$	- 186.1
6	$\text{Ni} + 2\text{CO} + \text{SO}_2 = \text{NiS} + 2\text{CO}_2$	- 139.1
<b>Reaction</b>	<b>Formation of Intermediate Gas Species</b>	<b><math>\Delta G^{\circ}_{900^{\circ}\text{C}}</math> (KJ/mol SO<sub>2</sub>)</b>
7	$3\text{CO} + \text{SO}_2 = \text{COS} + 2\text{CO}_2$	-83.6
8	$2\text{CO} + \text{SO}_2 = 1/2 \text{S}_2 + 2\text{CO}_2$	-84.7
<b>Reaction</b>	<b>Reactions with COS</b>	<b><math>\Delta G^{\circ}_{900^{\circ}\text{C}}</math> (KJ/mol COS)</b>
9	$1/2 \text{Fe}_2\text{O}_3 + 1/2 \text{CO} + \text{COS} = \text{FeS} + 3/2 \text{CO}_2$	-101.8
10	$1/3 \text{Fe}_3\text{O}_4 + 1/3 \text{CO} + \text{COS} = \text{FeS} + 4/3 \text{CO}_2$	-83.8
11	$\text{FeO} + \text{COS} = \text{FeS} + \text{CO}_2$	-82.3
12	$\text{Fe} + \text{COS} = \text{FeS} + \text{CO}$	-85.3
13	$\text{NiO} + \text{COS} = \text{NiS} + \text{CO}_2$	-102.5
14	$\text{Ni} + \text{COS} = \text{NiS} + \text{CO}$	-55.5
<b>Reaction</b>	<b>Reactions with S<sub>2</sub></b>	<b><math>\Delta G^{\circ}_{900^{\circ}\text{C}}</math> (KJ/mol S<sub>2</sub>)</b>
15	$\text{Fe}_2\text{O}_3 + 3\text{CO} + \text{S}_2 = 2\text{FeS} + 3\text{CO}_2$	-201.3
16	$2/3 \text{Fe}_3\text{O}_4 + 8/3 \text{CO} + \text{S}_2 = 2\text{FeS} + 8/3 \text{CO}_2$	-165.4
17	$2\text{FeO} + 2\text{CO} + \text{S}_2 = 2\text{FeS} + 2\text{CO}_2$	-161.8
18	$2\text{Fe} + \text{S}_2 = 2\text{FeS}$	-175.9
19	$2\text{NiO} + 2\text{CO} + \text{S}_2 = 2\text{NiS} + 2\text{CO}_2$	-202.6
20	$2\text{Ni} + \text{S}_2 = 2\text{NiS}$	-108.7

## 4.2 Model Results

The models predict that NiS and FeS are the only thermodynamically stable sulfide species in the calcine. It further inferred that all of the sulfur in the input stream that may exist either as gaseous or in solid phase is completely converted to iron and nickel sulfides. **Figure 4.1** shows the effect of  $P_{SO_2}$  in the input gas mixture on the sulfur content of the calcine. The % S in the calcine increases linearly by increasing  $P_{SO_2}$  in the gas mixture and reaches a maximum value of approximately 4 %. According to thermodynamic simulations, increasing  $P_{CO}$  in the gas mixture negligibly increases the % S in the calcine. The effect of the amount of the gas mixture on % S in the calcine is evident and found to be in direct relation. In other words, purging lower flow rates of the gas mixture that represents the freeboard gas results in decreased sulfur content in the calcine.

**Figure 4.2 a-c** shows that the improvement of nickel grade (i.e., nickel in ferronickel alloy) is directly related to  $P_{SO_2}$ , which validates the formation FeS in the calcine. Increasing  $P_{SO_2}$  promotes the formation of FeS, which results in lower Fe (**Figure 4.2 d-f**) and higher Ni grades. In Contrast, at constant  $P_{SO_2}$ , the nickel grade decreases by increasing  $P_{CO}$  because of enhanced metallization of iron. The nickel grade reduces by lowering the amount of the gas mixture, possibly due to low iron sulfurization, which in turn promotes iron metallization.

**Figure 4.3 a-f** shows the effect of  $P_{SO_2}$  on the metallization of nickel and iron. The metallization of iron and nickel decreases by increasing the  $P_{SO_2}$ . At constant  $P_{SO_2}$ , increasing  $P_{CO}$  enhances the metallization of both iron and nickel. **Figure 4.4 a-f** shows that the sulfurization of nickel and iron increases with  $P_{SO_2}$ . The increase in  $P_{CO}$  slightly affects the iron sulfurization; however, it noticeably decreases the nickel sulfurization. The decrease in nickel sulfurization can

be associated with the sulfurization of NiO, i.e., reaction 5 in **Table 4.3**, being thermodynamically more favorable compared with that of Ni, i.e., reaction 6 in **Table 4.3**. In other words, the Gibbs free energy of the sulfurization reaction is lower for NiO than Ni, i.e., -186.1 vs. -139.1 kJ/mol NiS. Higher  $P_{\text{CO}}$  leads to higher Ni and lower NiO content, which in turn results in lower sulfurization of nickel.

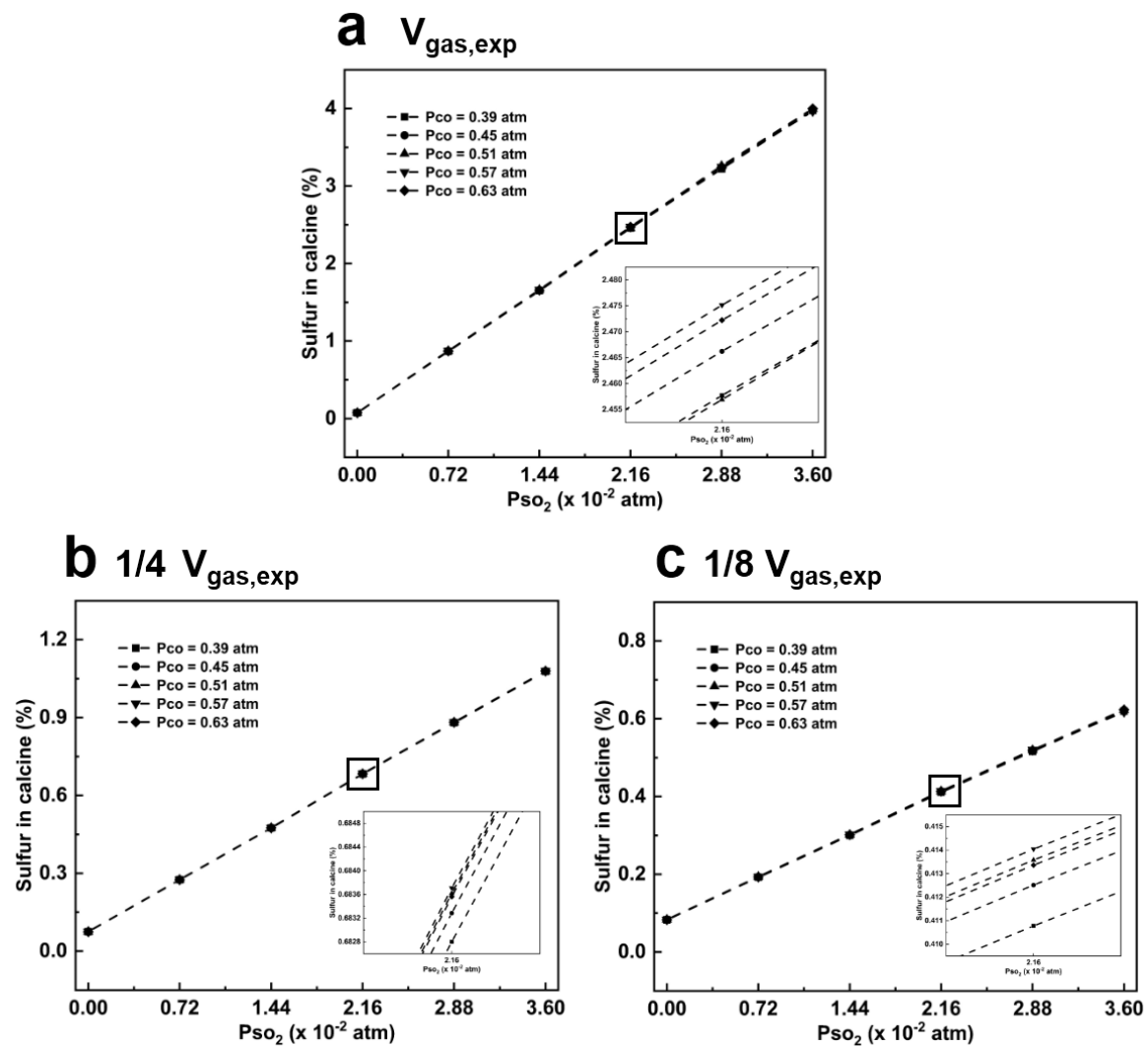


Figure 4.1 Predicted sulfur content of the calcine produced at 900 °C for various amount of gas mixtures (a) experimental amounts listed in Table 3.3 (b) one - fourth of the experimental amounts (c) one - eighth of the experimental amounts

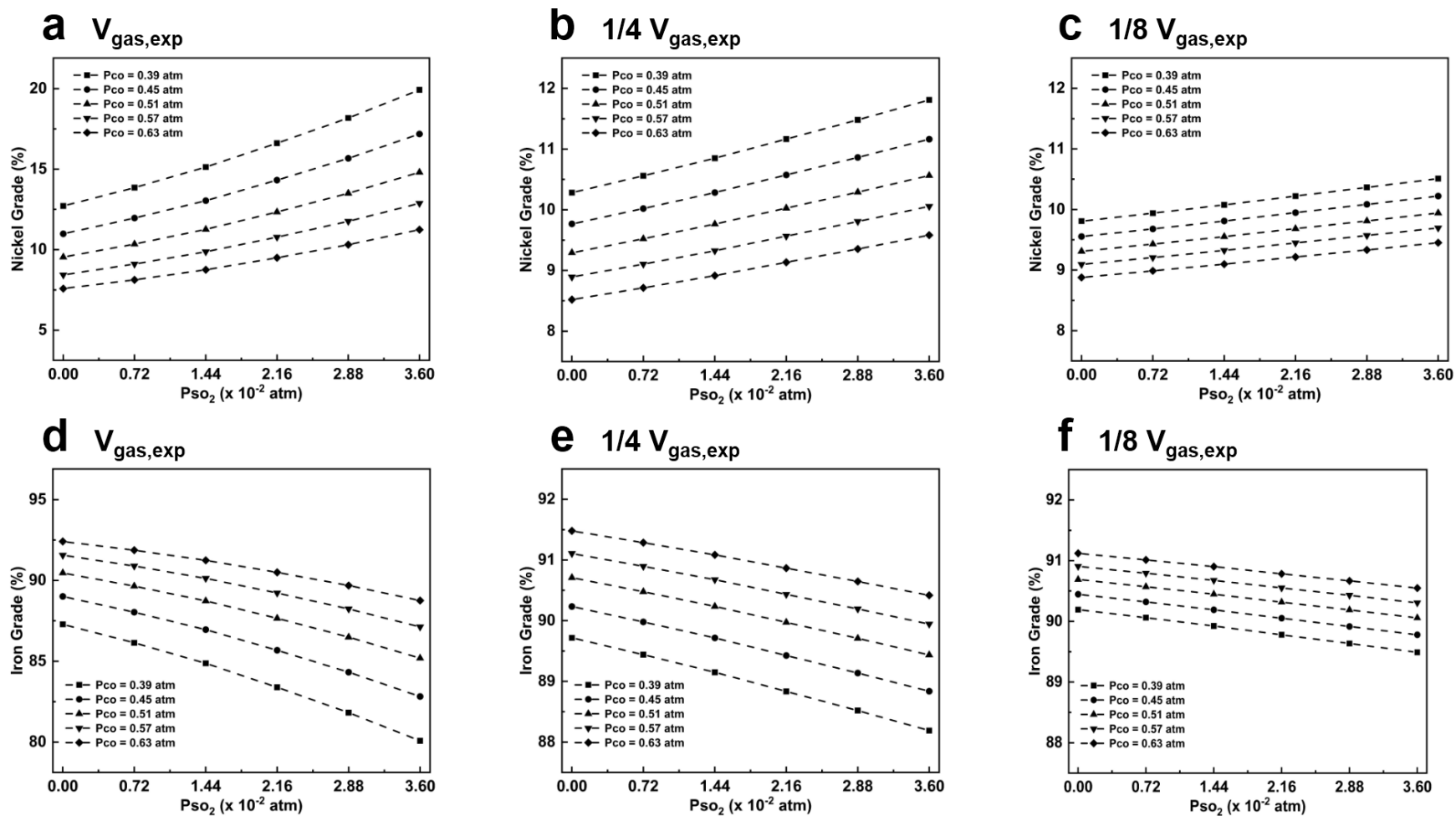


Figure 4.2 Predicted grades (i.e., percentages of iron and nickel in ferronickel alloy) at 900 °C for experiments listed in Table 3.3 (a-c) nickel (d-f) iron

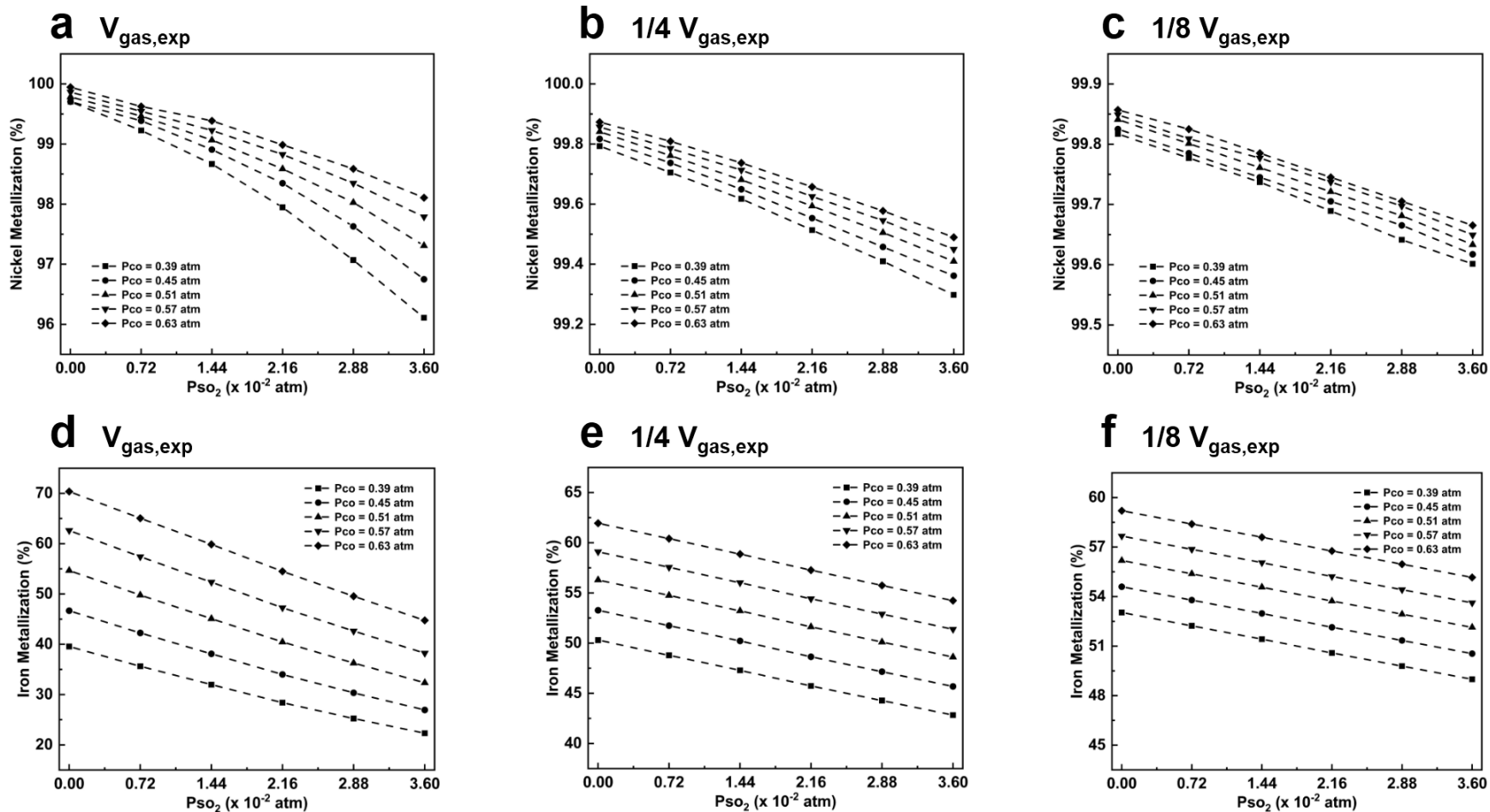


Figure 4.3 Predicted metallization of nickel/iron at 900 °C for experiments listed in Table 3.3 (a-c) nickel (d-f) iron

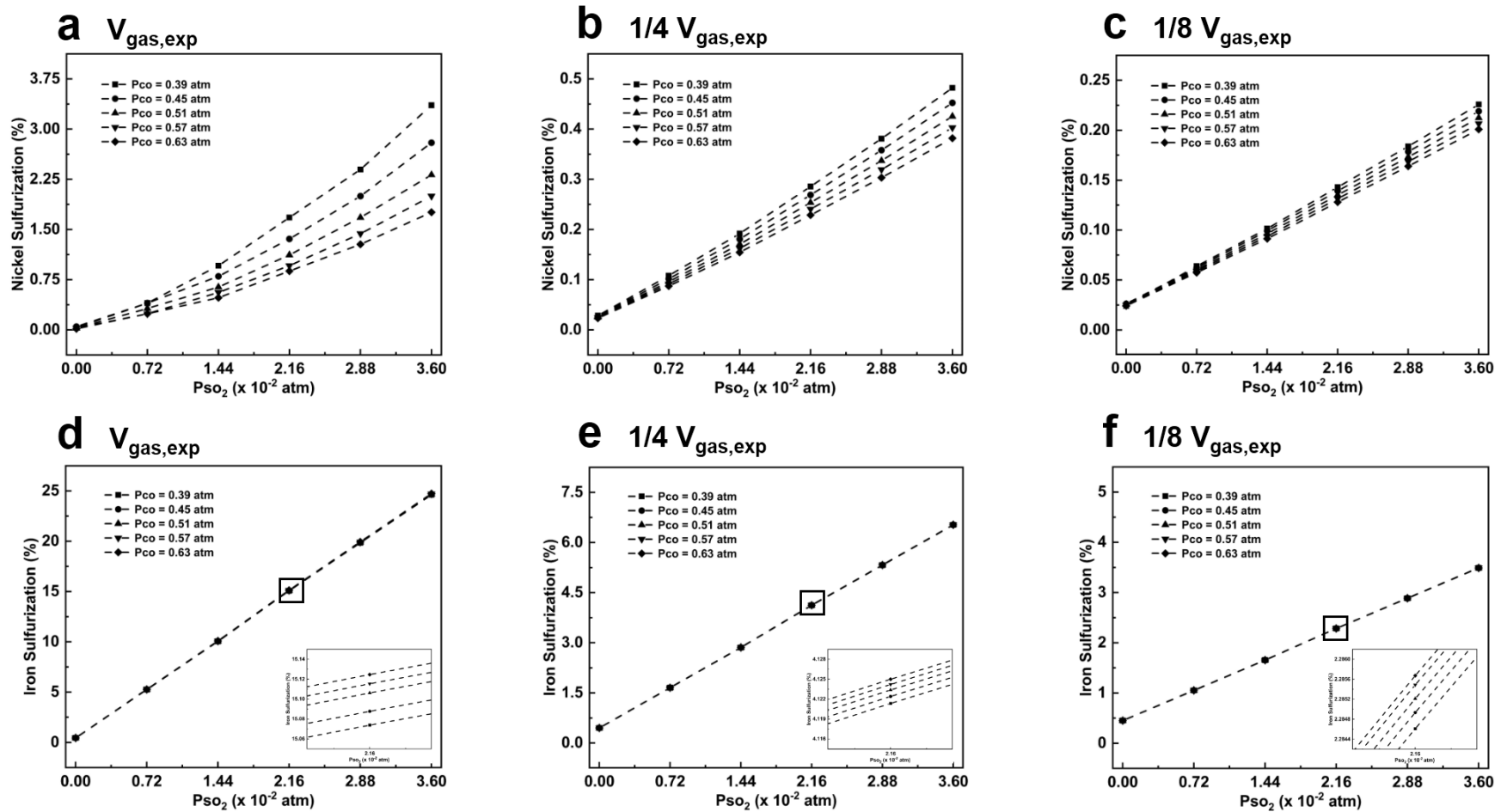


Figure 4.4 Predicted sulfurization of nickel/iron at 900 °C for experiments listed in Table 3.3 (a-c) nickel (d-f) iron

## Chapter 5: Experimental Results and Discussion

The sulfurization of laterite ore using various reducing gas mixtures has been investigated. The gas mixtures are intended to simulate the combustion products of rotary kiln fuels (i.e., coal). The sulfur content of the calcine is measured at various  $P_{SO_2}$  and  $P_{CO}$  values presented in **Table 3.3**. The impact of the flow rate of the input gas on the sulfur content of the calcine is investigated by lowering the flowrate for the experiments listed in **Table 3.4**. X-ray diffraction is used to confirm the reduction of the ore in the rotary kiln and to identify sulfur-containing products. The bromine - methanol leach test is employed to determine the sum of iron and nickel present as metallic and sulfide form in the calcine at various  $P_{SO_2}$  values. Finally, energy dispersive spectroscopy is used to investigate the composition of the calcine.

### 5.1 The Effect of $P_{SO_2}$ on the Sulfur Content of the Calcine

**Figure 5.1 - 5.5** shows the effect of  $P_{SO_2}$  in the input gas mixture on the sulfur content of the calcine. At constant  $P_{CO}$ , the % S in the calcine was found to be in direct relation with  $P_{SO_2}$  in the input gas mixture. The sulfur in calcine is found to be lowest at  $P_{SO_2} = 0$  atm, i.e., when there is no sulfur in the coal used as rotary kiln fuel. The % S in calcine continuously increases by increasing  $P_{SO_2}$  and reaches its highest at  $P_{SO_2} = 0.0360$  atm, which is equivalent to 10 % S in the coal. **Figure 5.6** compares experimentally obtained % S values with results obtained by the thermodynamic modelling. It is observed that the experimental amounts are lower than the thermodynamic predictions due to the kinetic limitations.

The increase in sulfur content of the calcine by increasing  $P_{SO_2}$  can be explained by a possible reaction sequence, as discussed by Bolsaitis and Nagata [38, 39], and the thermodynamic discussion presented in **Chapter 4**. In a reducing gas mixture,  $SO_2$  reacts with CO and form

gaseous products, i.e., COS and S<sub>2</sub>, according to reactions 7 and 8 shown in **Table 4.3**. These gaseous species are the intermediate products of the calcine sulfurization. Bolsaitis and Nagata observed that when X<sub>CO</sub> is higher than 0.92 in a CO-SO<sub>2</sub> gas mixture, COS is the most dominant intermediate gas species. Thermodynamic simulations in this study predicted similar results, and P<sub>COS</sub> was found to be significantly higher than P<sub>S<sub>2</sub></sub> for four different experimental gas mixtures (**Table 4.2**). However, it should be noted that both COS and S<sub>2</sub> are active sulfurization agents that react with iron, nickel, and their oxides and produce sulfur-containing compounds as given by reactions 9 - 20 in **Table 4.3**. In a nutshell, an increase in the SO<sub>2</sub> content of the combustion product of rotary kiln fuel promotes the sulfurization of the laterite ore during calcination.

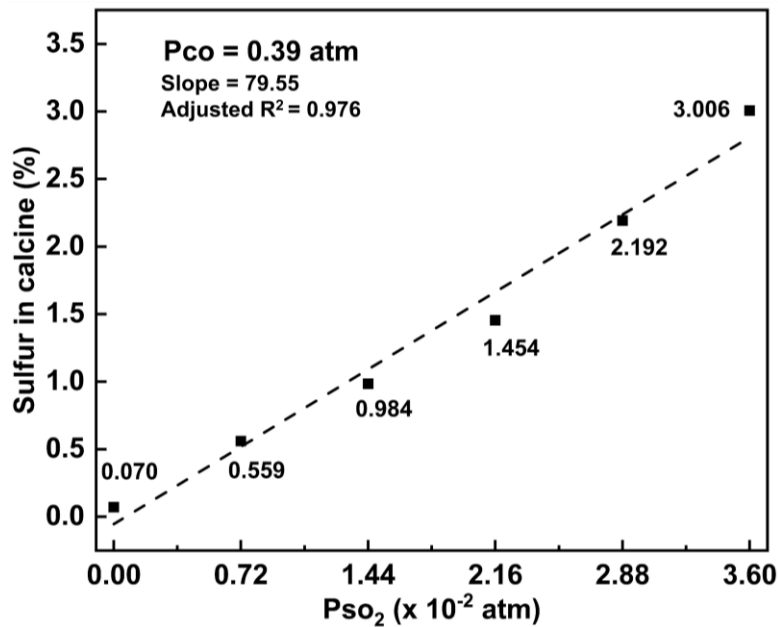


Figure 5.1 The effect of P<sub>SO<sub>2</sub></sub> on the sulfur content of the calcine produced at 900 °C and P<sub>CO</sub> = 0.39 atm

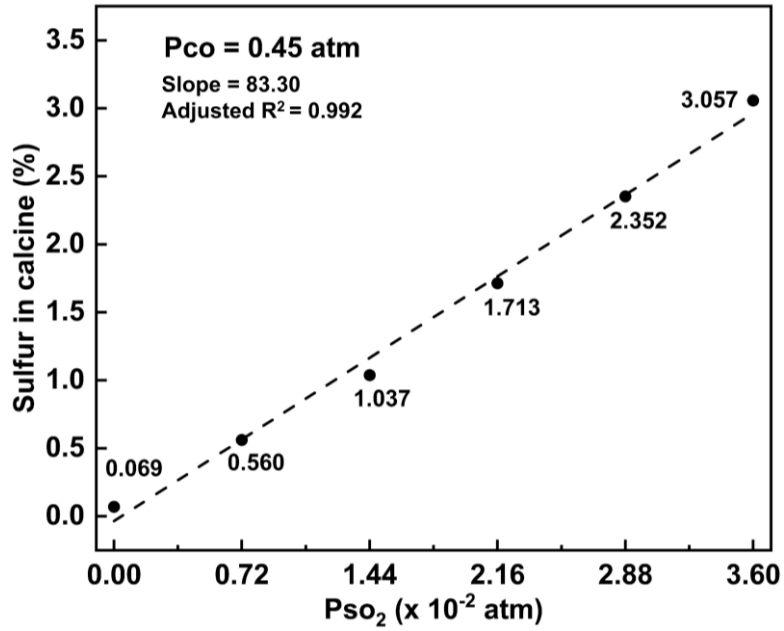


Figure 5.2 The effect of P<sub>SO<sub>2</sub></sub> on the sulfur content of the calcine produced at 900 °C and P<sub>CO</sub> = 0.45 atm

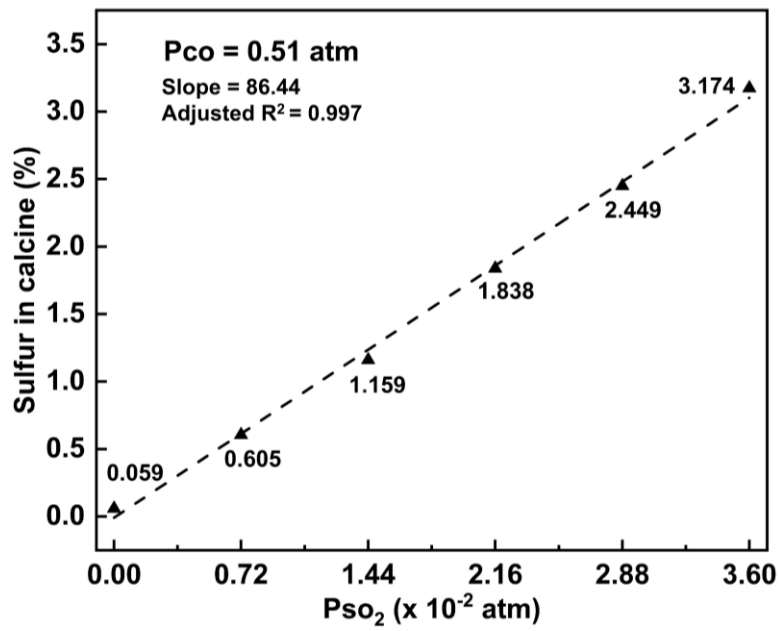


Figure 5.3 The effect of P<sub>SO<sub>2</sub></sub> on the sulfur content of the calcine produced at 900 °C and P<sub>CO</sub> = 0.51 atm

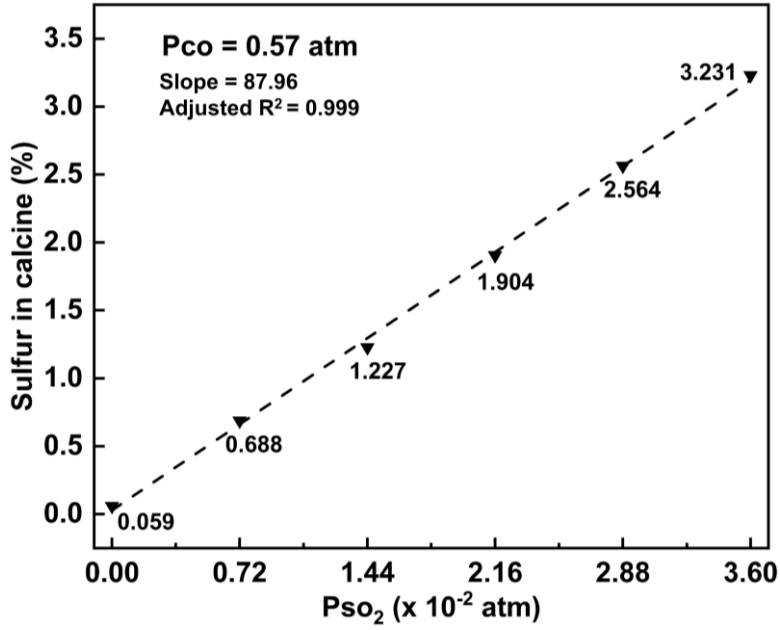


Figure 5.4 The effect of P<sub>SO<sub>2</sub></sub> on the sulfur content of the calcine produced at 900 °C and P<sub>CO</sub> = 0.57 atm

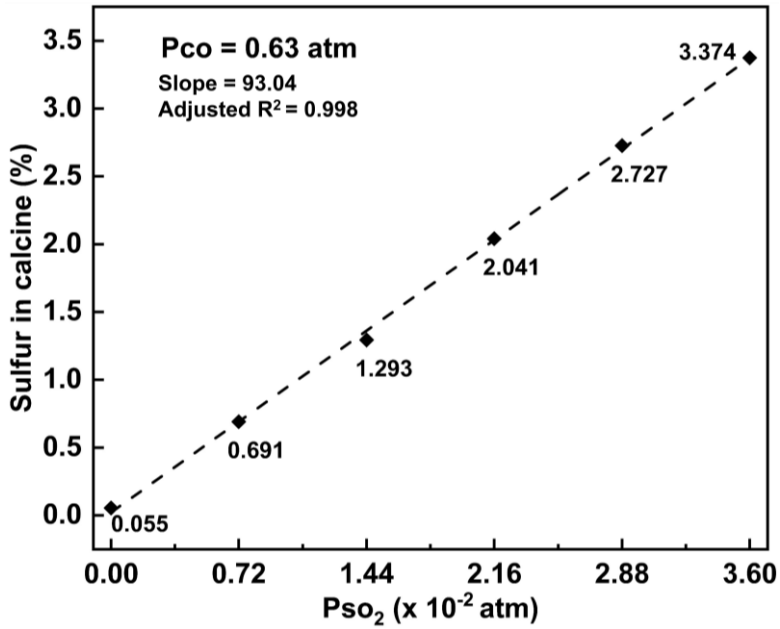


Figure 5.5 The effect of P<sub>SO<sub>2</sub></sub> on the sulfur content of the calcine produced at 900 °C and P<sub>CO</sub> = 0.63 atm

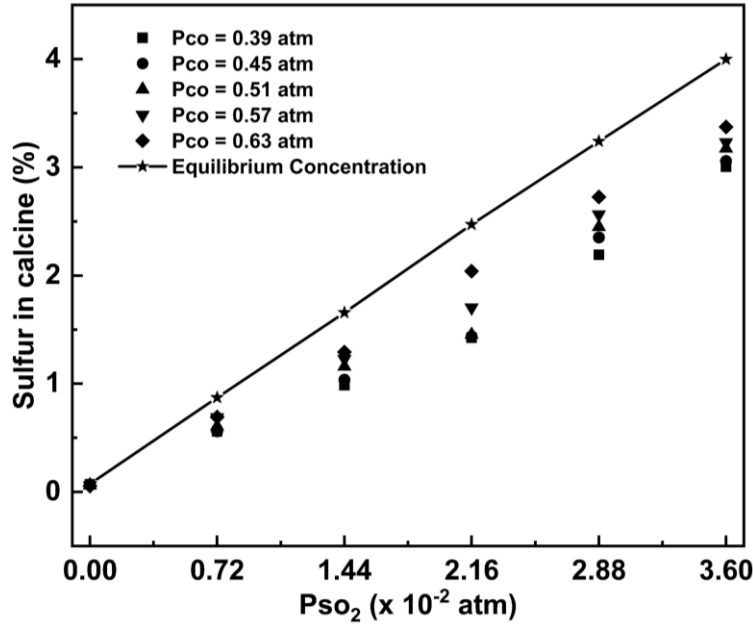


Figure 5.6 Comparison of experimentally obtained % S values with thermodynamic simulations

## 5.2 The Effect of $P_{CO}$ on the Sulfur Content and Sulfur Deportation in the Calcine

It is noteworthy that the slope of regression lines in **Figure 5.1 - 5.5** increases with increasing  $P_{CO}$  in the input gas mixtures. This implies a relation between the sulfur content of the calcine and  $P_{CO}$ . The effect of  $P_{CO}$  on % S in the calcine at constant  $P_{SO_2}$  is investigated experimentally and plotted in **Figure 5.7 - 5.12**. The data points obtained from the linear regression lines (shown in **Figure 5.1 - 5.5**) are overlaid on the experimentally obtained values. Lastly, the deportation of sulfur given by equation 5.1 is plotted separately in **Figure 5.7 - 5.12**.

$$\% \text{ Sulfur Deportation} = \frac{\text{Mass of sulfur in the calcine}}{\text{Total mass of input sulfur}} \times 100 \quad \text{Eq. 5.1}$$

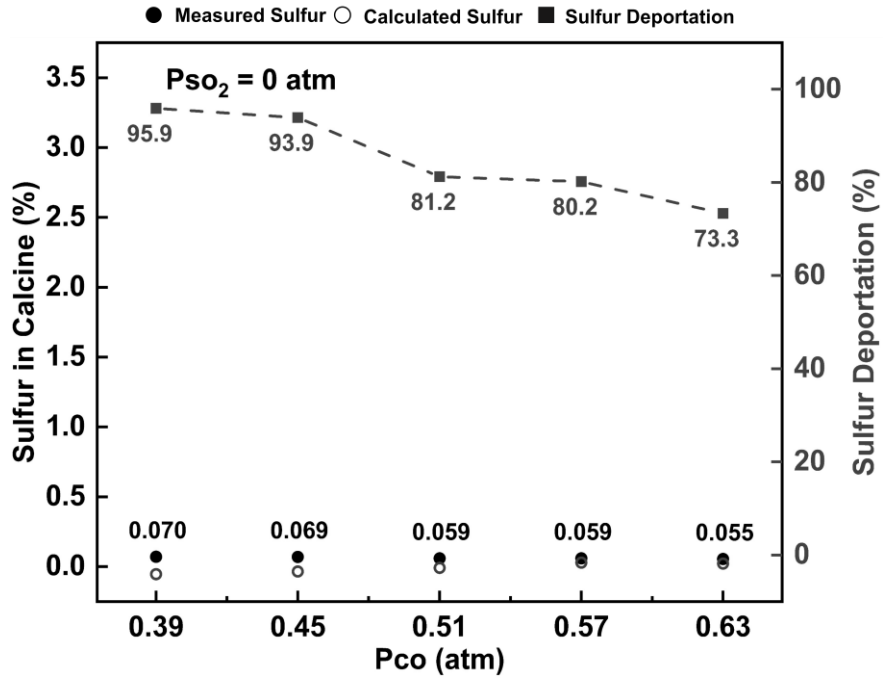


Figure 5.7 The effect of  $P_{CO}$  on the sulfur content and sulfur deportation of the calcine produced at 900 °C and  $P_{SO_2} = 0$  atm

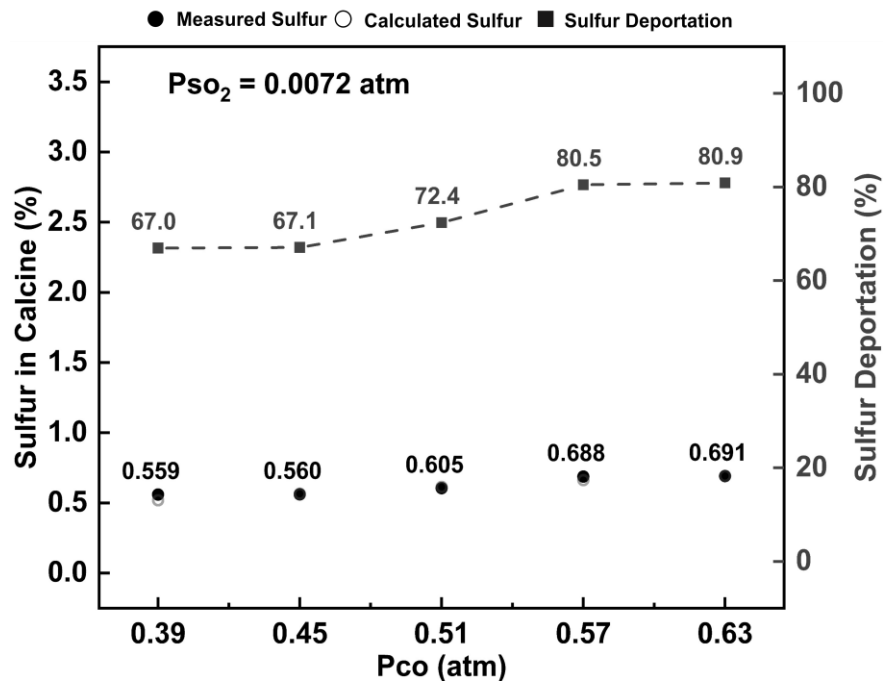


Figure 5.8 The effect of  $P_{CO}$  on the sulfur content and sulfur deportation of the calcine produced at 900 °C and  $P_{SO_2} = 0.0072$  atm

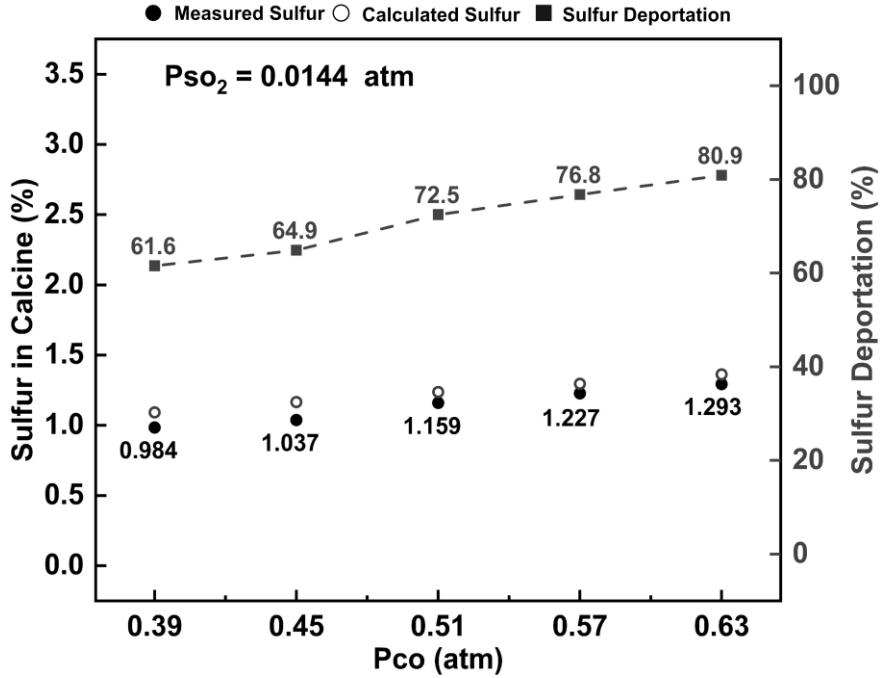


Figure 5.9 The effect of  $P_{CO}$  on the sulfur content and sulfur deportation of the calcine produced at 900 °C and  $P_{SO_2} = 0.0144$  atm

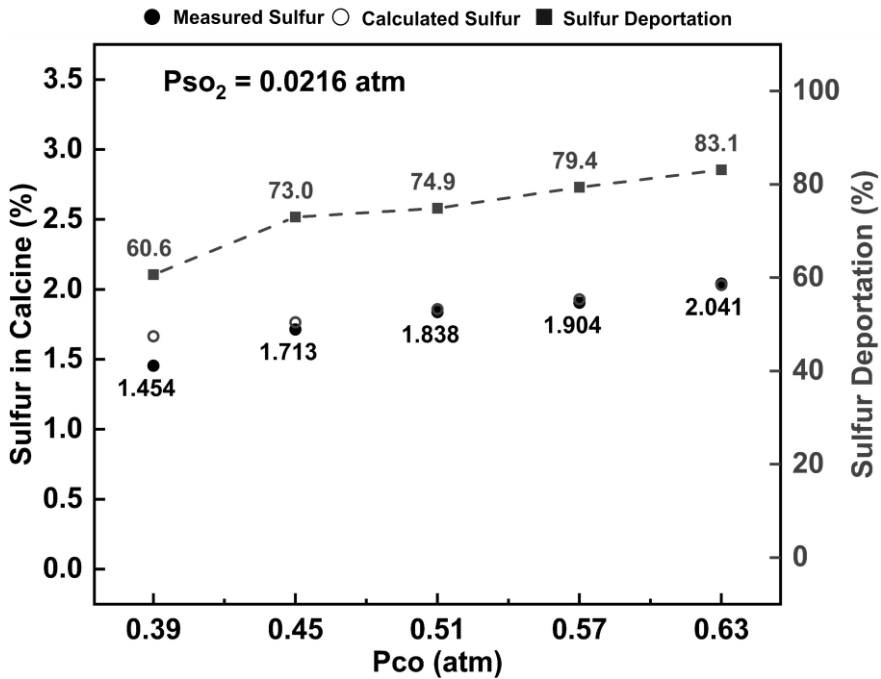


Figure 5.10 The effect of  $P_{CO}$  on the sulfur content and sulfur deportation of the calcine produced at 900 °C and  $P_{SO_2} = 0.0216$  atm

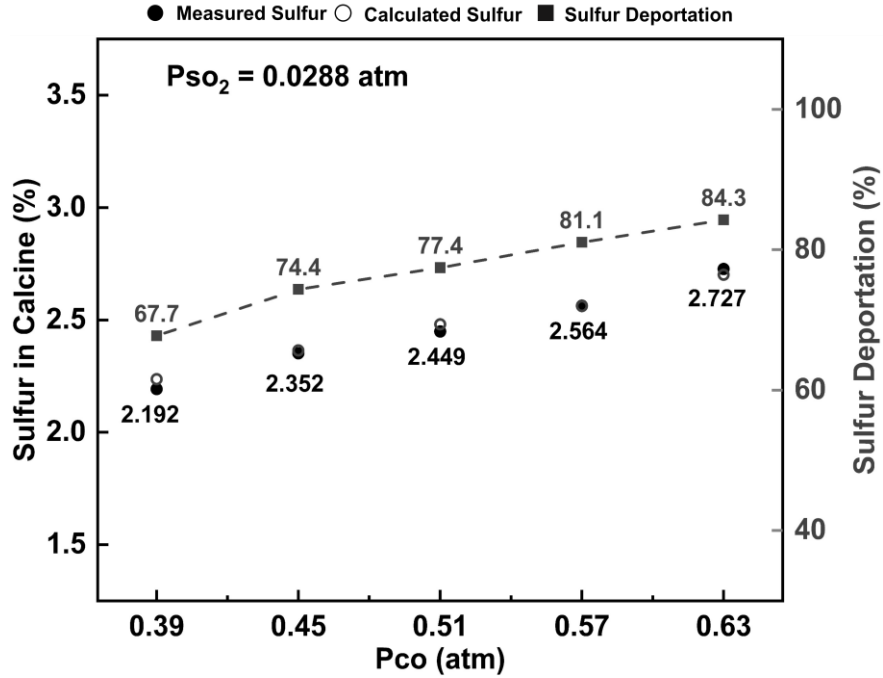


Figure 5.11 The effect of  $P_{CO}$  on the sulfur content and sulfur deportation of the calcine produced at 900 °C and  $P_{SO_2} = 0.0288$  atm

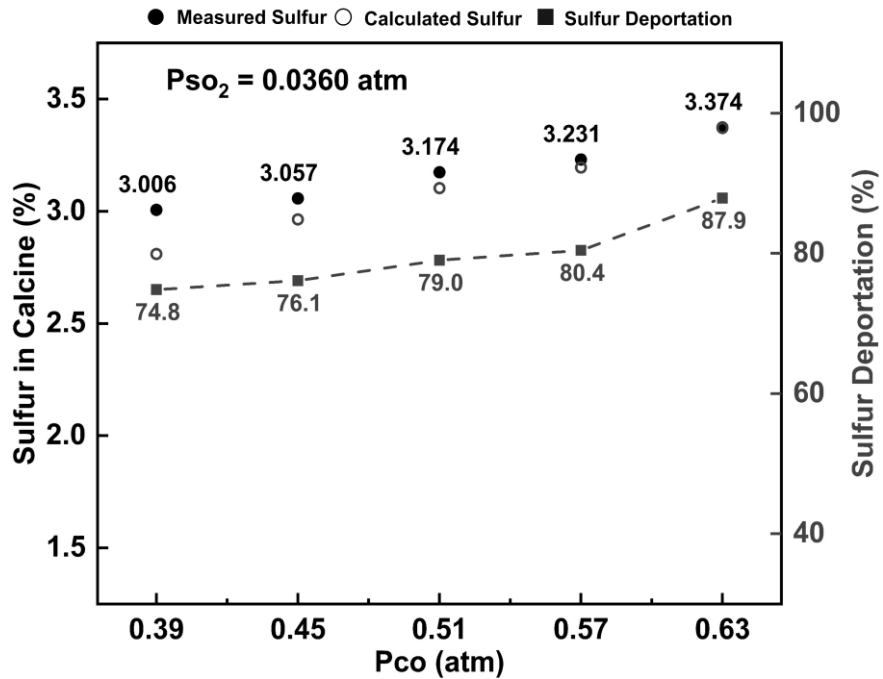


Figure 5.12 The effect of  $P_{CO}$  on the sulfur content and sulfur deportation of the calcine produced at 900 °C and  $P_{SO_2} = 0.0360$  atm

The % S in the calcine at  $P_{\text{SO}_2} = 0$  atm (**Figure 5.7**) slightly decreases by increasing  $P_{\text{CO}}$  in the input gas. Similarly, the deportation of sulfur also reduces by increasing the  $P_{\text{CO}}$  values. The sulfur in the ore and coal is usually found to be in the form of pyrite ( $\text{FeS}_2$ ) [45]. Hence, the marginal decrease in % S in the calcine may be attributed to the reaction of pyrite with carbon monoxide to form COS as given by the equation 5.2. However, it should be noted that the COS generated can react with the ore again and form sulfide species as provided by reactions 9 -14 in **Table 4.3**. Hence, even though the % S and % sulfur deportation decreases with increasing  $P_{\text{CO}}$ , it is negligibly small due to the re-utilization of COS to generate sulfide products.



**Figure 5.8 - 5.12**, shows the variation in % S in the calcine and % sulfur deportation with changing  $P_{\text{CO}}$ . At constant values of  $P_{\text{SO}_2}$  between 0.0072 and 0.0360 atm, the % S in the calcine and % sulfur deportation increases with increasing  $P_{\text{CO}}$ . According to the reactions given in **Table 4.3**, the evolution of COS is promoted by the increasing  $P_{\text{CO}}$  in the input gas mixtures, and as a result, the overall generation of sulfide products increase. In other words, increasing  $P_{\text{CO}}$  in the input gas mixtures can increase  $P_{\text{COS}}$ , which subsequently enhances the sulfurization of the calcine.

A model is developed to predict % S in the calcine as a function of both  $P_{\text{SO}_2}$  and  $P_{\text{CO}}$  by using the sum of square error minimization technique. The % S in the calcine, is predicted by the model according to equation 5.3. The values predicted by the model are overlaid on experimental values in **Figure 5.13**. It can be seen that the modeled and measured values are in excellent agreement with each other.

$$\% \text{ S} = 51.9 P_{\text{SO}_2} + 66.4 P_{\text{CO}} \quad \text{Eq. 5.3}$$

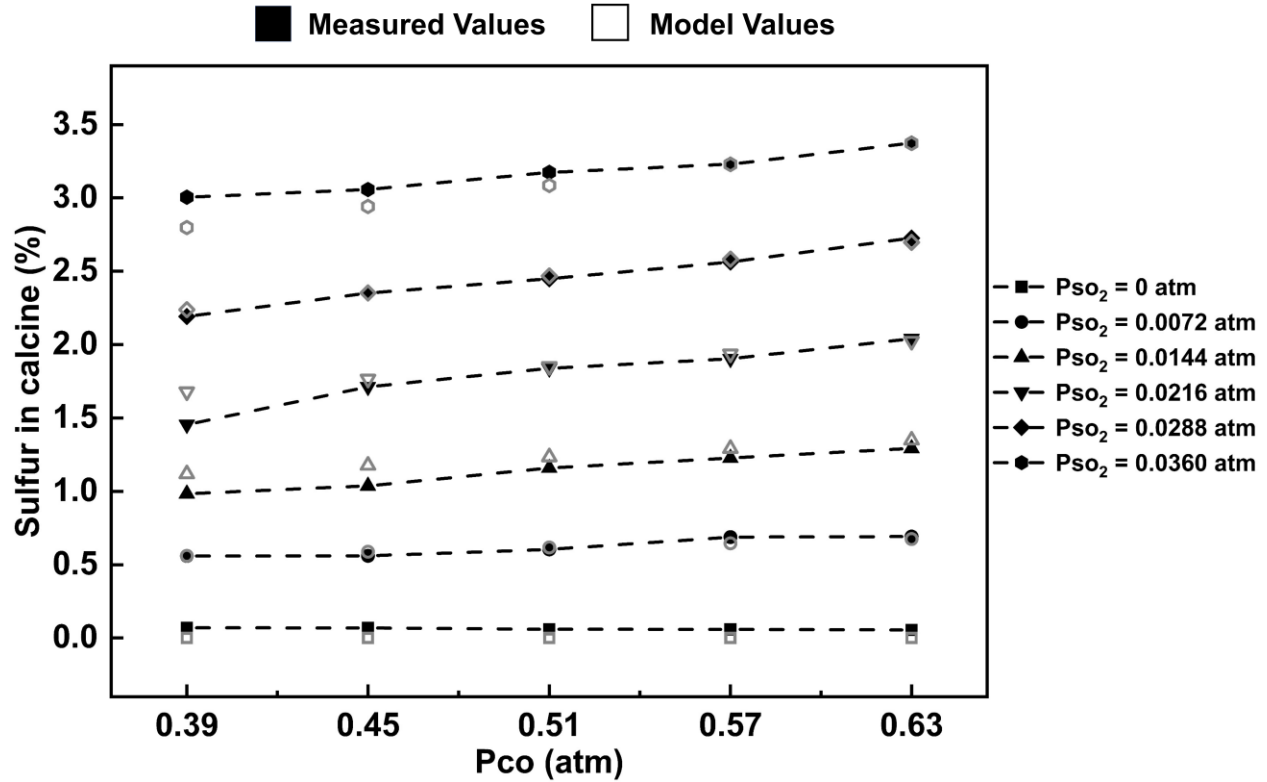


Figure 5.13 Comparison of experimentally obtained % S values with those predicted by the model

### 5.3 The Effect of the Flow Rate of the Input Gas on % S in the Calcine

**Figure 5.14** shows the change in % S in the calcine as a function of  $P_{SO_2}$  for the two different flow rates, i.e., 292 and 176 ml/min at a fixed  $P_{CO}$  value of 0.51 atm. Similarly, **Figure 5.15** shows variation in % sulfur deportation as a function of  $P_{SO_2}$  for these flow rates. Decreasing the flow rate of input gas mixtures in the furnace results in lower sulfur content of the calcine, as evident in **Figure 5.14**. There are two possible explanations for the decrease in % S in the calcine: i) The decline is mostly associated with lower amount of the sulfurization gas, i.e.,  $SO_2$ , which may react with the ore to form sulfide species ii) In addition, there might be some kinetic limitations associated with lower flow rate. Sulfur deportation (%) plotted in **Figure 5.15**, decreases by lowering the input gas volume. Hence, it is assumed that the gas flow rate may affect

reaction kinetics, and gas-solid mass transfer coefficient could be a rate-controlling factor under such applied conditions.

The gas-solid mass transfer coefficient,  $k_g$ , for a spherical particle in an uninterrupted gas flow can be calculated according to Ranz and Marshall correlation presented in equation 5.4 with the Reynolds ( $Re$ ) and Schmidt ( $Sc$ ) number defined with equations 5.5 and 5.6 respectively [46]. Increasing gas flow rate increases gas velocity, which results in higher  $Re$  number. Based on Ranz and Marshall correlation, higher gas velocity results in a higher mass transfer coefficient. In other words, faster mass transfer at higher flow rates is partially responsible for the higher sulfur content of the calcine.

$$Sh = \frac{k_g d_s}{D} = 2.0 + 0.6Re^{\frac{1}{2}}Sc^{\frac{1}{3}} \quad \text{Eq. 5.4}$$

$$Re = \frac{\rho_g v d_s}{\mu_g} \quad \text{Eq. 5.5}$$

$$Sc = \frac{\mu_g}{\rho_g D} \quad \text{Eq. 5.6}$$

Where  $d_s$  is the diameter of the particle,  $D$  is the diffusion coefficient,  $v$  is the gas velocity,  $\rho_g$  is the density and  $\mu_g$  is the viscosity of the gas phase.

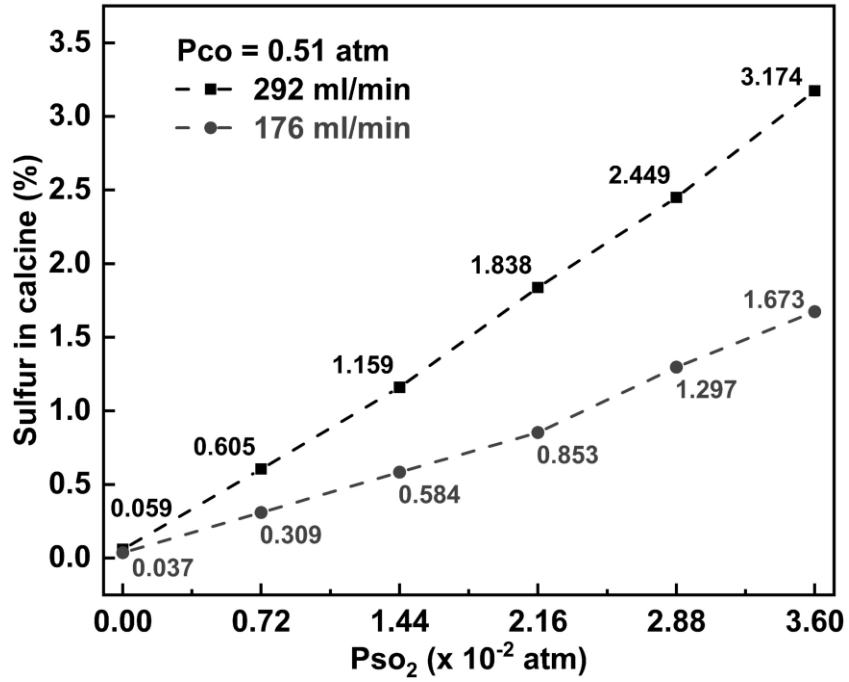


Figure 5.14 The effect of gas flow rate on % S in the calcine for a 2-hour residence time at 900 °C

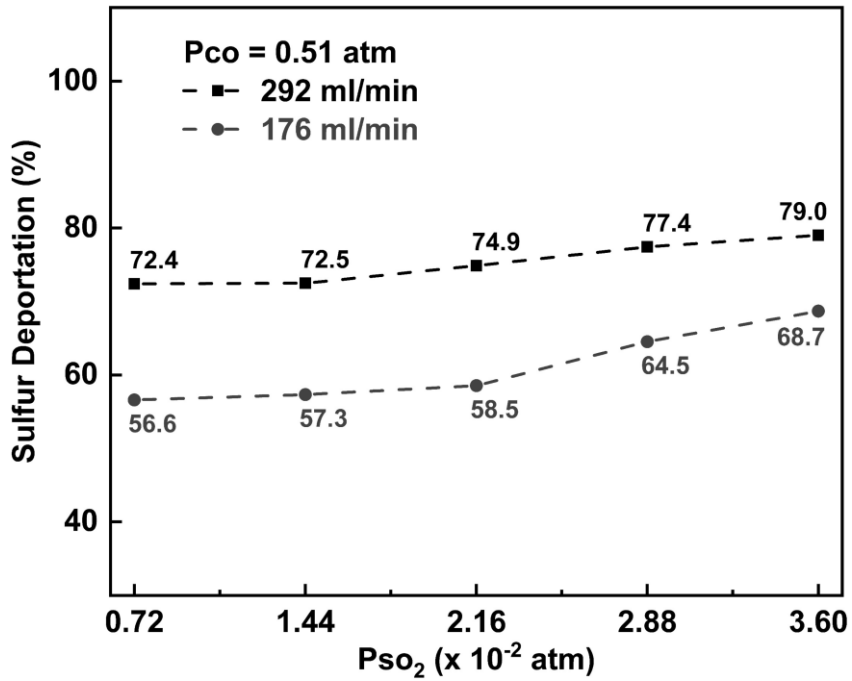


Figure 5.15 The effect of gas flow rate on % sulfur deportation in the calcine for a 2-hour residence time at 900 °C

#### 5.4 X-ray Diffraction of the Calcine

The X-ray diffraction analysis was performed on three different calcine samples to ascertain the mineralogy of the product, as shown in **Figure 5.16, 5.17, and 5.18**, respectively. The tested samples were calcined at constant  $P_{\text{SO}_2} = 0.0360$  atm, and  $P_{\text{CO}} = 0.39, 0.51$  and  $0.63$  atm, respectively. The major iron-bearing minerals in all of the tested samples were found to be forsterite and fayalite, where iron is present as  $\text{Fe}^{+2}$  in the crystalline structure. Since, iron in the raw ore was present in the form of nontronite, lizardite, and goethite, i.e.,  $\text{Fe}^{+3}$  minerals, the formation of forsterite and fayalite indicates the reduction of iron from  $\text{Fe}^{+3}$  to  $\text{Fe}^{+2}$  state. The formation of olivine group minerals is also justified by Hallet's (1997) study, where it was found that minerals such as lizardite and smectite (nontronite) undergoes dehydroxylation in the temperature range of  $500 - 800$  °C and recrystallizes to olivine above  $800$  °C [47].

The only sulfur-containing compound found by XRD analysis was pyrrhotite,  $\text{Fe}_{11}\text{S}_{12}$ . A noteworthy feature in **Figure 5.16 - 5.18** is the increase in the intensities of pyrrhotite and ferronickel peaks by increasing the  $P_{\text{CO}}$  in input gas. Pyrrhotite and ferronickel peaks are highlighted in these figures. It can be seen that the peak intensities are the lowest at  $P_{\text{CO}} = 0.39$  atm and the highest at  $P_{\text{CO}} = 0.63$  atm. XRD results are in line with the findings of ICP analysis presented in **Figure 5.7 - 5.12**, where % S in the calcine was found to be in direct relation with  $P_{\text{CO}}$ . Similarly, metallic content in the calcine, i.e., ferronickel, is observed to be in direct relation with  $P_{\text{CO}}$  according to the XRD results.

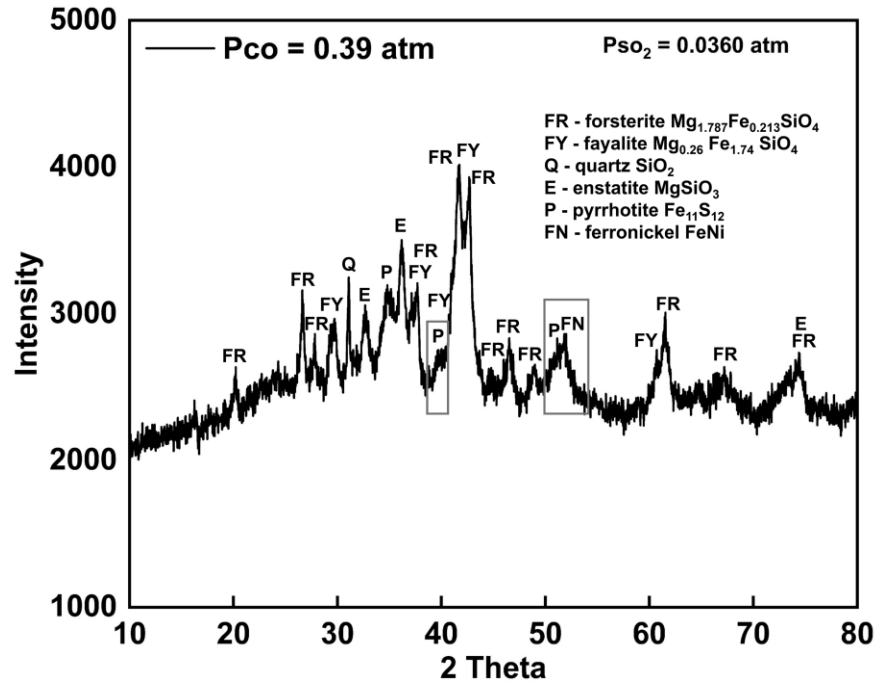


Figure 5.16 XRD pattern of the calcine produced at 900 °C under  $P_{SO_2} = 0.0360 \text{ atm}$  and  $P_{CO} = 0.39 \text{ atm}$

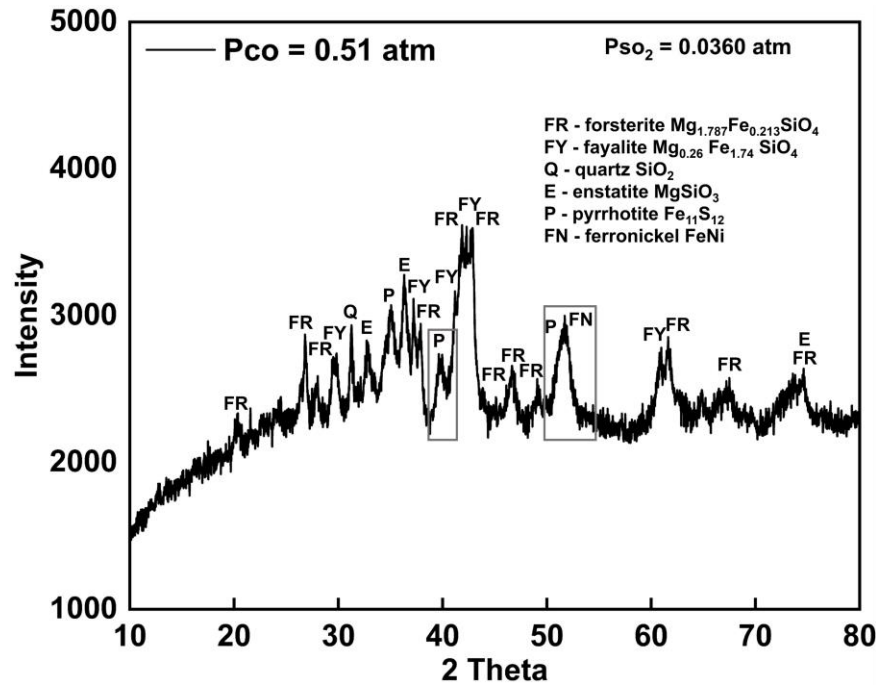


Figure 5.17 XRD pattern of the calcine produced at 900 °C under  $P_{SO_2} = 0.0360 \text{ atm}$  and  $P_{CO} = 0.51 \text{ atm}$

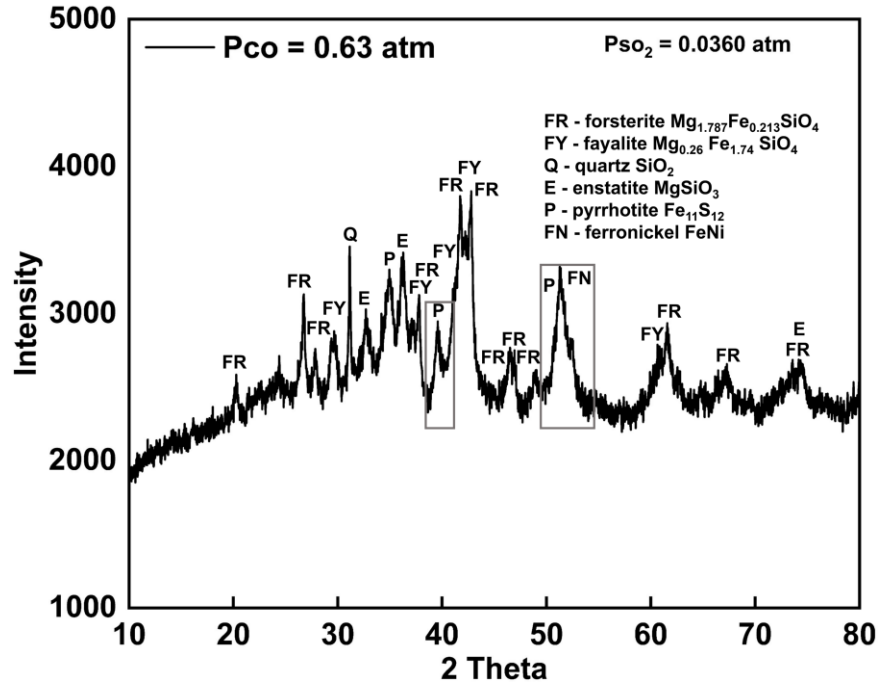


Figure 5.18 XRD pattern of the calcine produced at 900 °C under  $P_{SO_2} = 0.0360 \text{ atm}$  and  $P_{CO} = 0.63 \text{ atm}$

### 5.5 The Effect $P_{SO_2}$ on Sum of Metallized and Sulfurized Iron and Nickel

The bromine - methanol leach test was performed for six calcine samples to find the sum of iron/nickel present in metallic and sulfide forms. The bromine - methanol solution is very selective in dissolving metallics and sulfides but does not dissolve oxides [32]. **Figure 5.19** shows the effect of increasing  $P_{SO_2}$  in the input gas mixtures on the sum of iron/nickel present as metal and sulfide in the calcine. The partial pressure of CO for all the tested samples was constant and equal to 0.63 atm.

At  $P_{SO_2} = 0 \text{ atm}$ , the metallization for both iron and nickel are found to be unexpectedly low. Moreover, opposed to the thermodynamic predictions, the metallization for nickel is less than that for iron. A possible explanation for both phenomena can be found in Hallet's (1997) study. The reducing gases in the current study were injected into the furnace upon reaching 900 °C. Hallet explained that minerals such as lizardite and nontronite undergo dehydroxylation in the

temperature range of 500 - 800 °C. Dehydroxylation results in an amorphous phase in which NiO is most susceptible to reduction. However, above 800 °C, recrystallization into olivine may occur and would require extreme reducing conditions to metalize nickel [47]. A slightly higher iron metallization can be explained by the presence of goethite in the ore (**Figure 3.1**), which can reduce to wustite under experimental conditions. Hallet elucidated that reduction to iron metal from wustite would occur before nickel metallization should the formation of olivine happen during calcination.

The percentage of oxides converted to metallic state and sulfides for iron/nickel increases by increasing  $P_{SO_2}$  in the input gas mixtures. This can be attributed to higher sulfurization in the calcine by increasing  $P_{SO_2}$ , which yields a higher percentage of iron and nickel sulfides. Nickel conversion exceeds that for iron at  $P_{SO_2}$  higher than 0.0072 atm. This may imply higher recovery of nickel from within the olivine structure by increasing  $P_{SO_2}$ . In other words, it may be possible that it is easier to sulfurize NiO entrapped within olivine structure than to reduce it to nickel metal.

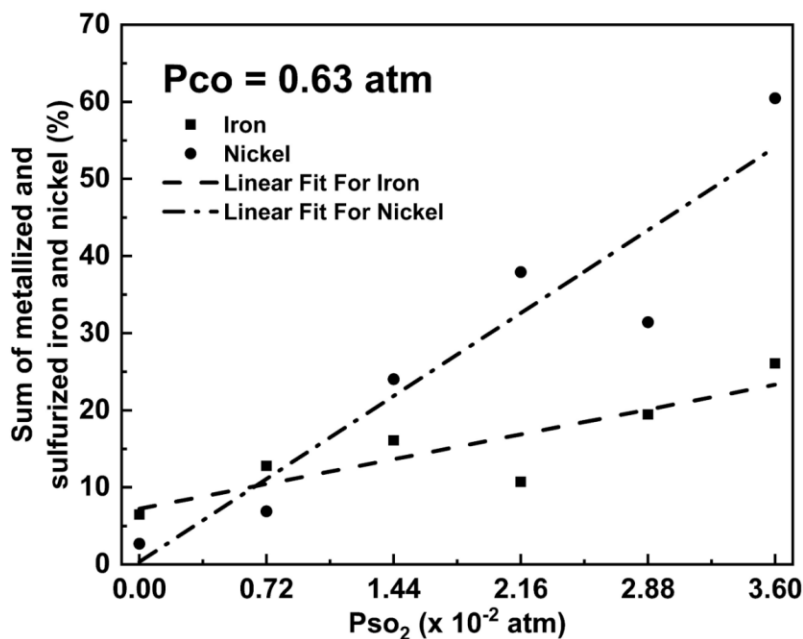


Figure 5.19 Sum of metallized and sulfurized iron/nickel in the calcine produced at 900 °C

## 5.6 Energy Dispersive Analysis of the Calcine

EDS analysis was done for a single calcine sample, i.e., Experiment 16, given in **Table 3.3** where  $P_{CO}$  and  $P_{SO_2}$  in the input gas mixture were 0.51 and 0.0216 atm, respectively. Initially, the map of sulfur was obtained to identify the areas with high sulfur concentrations. **Figure 5.20 a** show the SEM image of the sample, and **b-f** shows EDS mapping on the same image for iron, sulfur, silicon, and magnesium. **Table 5.1** lists the atomic concentrations of various elements for six selected points in **Figure 5.20 a**, which seemed to be more abundant in sulfur. The presence of sulfur in the sample is further confirmed by EDS analysis, as shown in **Figure 5.20 c** and **Table 5.1**.

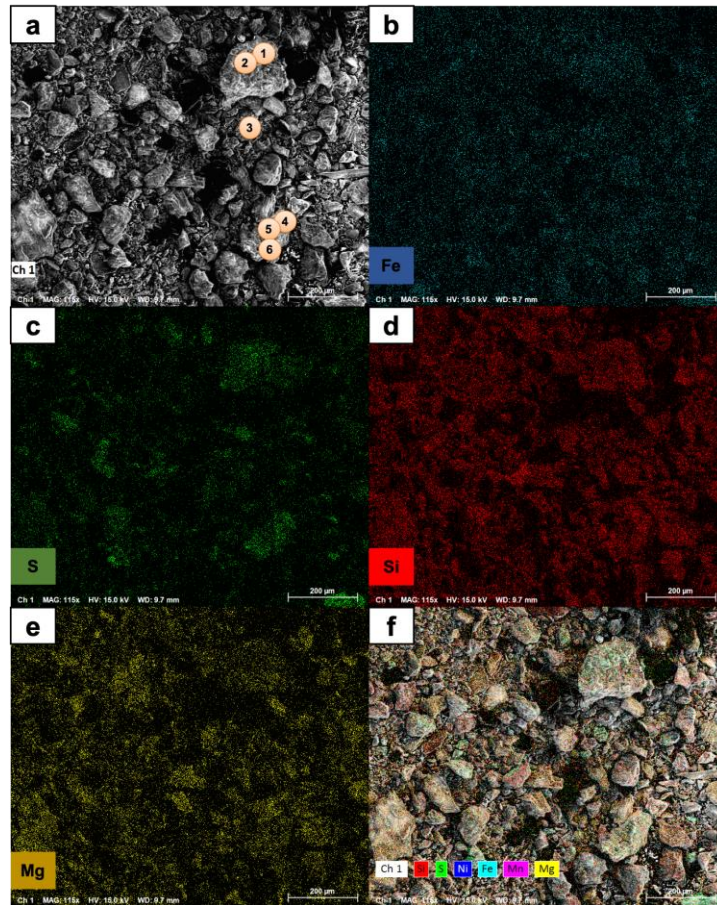


Figure 5.20 (a) SEM image of the calcine produced at 900 °C under  $P_{CO} = 0.51$  atm and  $P_{SO_2} = 0.0216$  atm (b-f) EDS mapping of iron, sulfur, silicon, and magnesium

Table 5.1 % Atomic concentration on selected points for calcine produced at 900 °C under  $P_{CO}$  and  $P_{SO_2}$  equal to 0.51 and 0.0216 atm, respectively

<b>Point</b>	<b>Oxygen</b>	<b>Silicon</b>	<b>Magnesium</b>	<b>Aluminum</b>	<b>Iron</b>	<b>Sulfur</b>
<b>1</b>	53.76	16.33	5.51	2.36	9.19	12.84
<b>2</b>	51.34	16.09	9.00	2.64	8.74	12.2
<b>3</b>	52.95	16.66	13.45	3.35	5.54	8.05
<b>4</b>	58.57	19.04	6.66	2.32	4.57	8.66
<b>5</b>	54.79	19.15	8.90	2.44	5.59	9.13
<b>6</b>	53.24	21.50	8.77	1.82	6.19	8.44

## Chapter 6: Conclusion

The behavior of nickel laterite ore in the CO-CO<sub>2</sub>-N<sub>2</sub>-SO<sub>2</sub> gas mixtures is investigated to understand the effect of the sulfur content of the fuel on the % S in the calcine. At constant P<sub>CO</sub>, the % S in the calcine is found to be directly proportional to P<sub>SO<sub>2</sub></sub> in the input gas mixtures. In other words, the higher the amount of sulfur in the coal used as the fuel, the higher the sulfur content of the resulting calcine. Similarly, at constant P<sub>SO<sub>2</sub></sub>, the sulfur content of the calcine and sulfur deportation increases with higher P<sub>CO</sub> in the input gas. This implies that the reducing atmosphere of the furnace contributes to sulfur transfer to the calcine. However, an exceptional case is observed at P<sub>SO<sub>2</sub></sub> = 0 atm, where the sulfur content and sulfur deportation slightly decrease by increasing P<sub>CO</sub> in the input gas. The findings of this study confirm the formation of sulfides during nickel laterite calcination in various CO-CO<sub>2</sub>-N<sub>2</sub>-SO<sub>2</sub> gas mixtures at 900 °C. An equation is developed to fit the experimentally obtained data given as:

$$\% S = 51.9 P_{SO_2} + 66.4 P_{SO_2} P_{CO}$$

At constant P<sub>SO<sub>2</sub></sub> and P<sub>CO</sub>, the % S in the calcine and % sulfur deportation is found to decrease by lowering the flow rate of the input gas mixtures. The gas-solid mass transfer coefficient is considered to be the rate-controlling factor in the tested range of the input gas flow rates. However, further investigation is required to understand the effect of the flow rate on the overall sulfurization process.

The x-ray diffraction analysis confirmed the presence of forsterite, fayalite, ferronickel, and pyrrhotite in the calcine. The intensity of the obtained peaks for pyrrhotite and ferronickel increase with P<sub>CO</sub> in the input gas.

At constant  $P_{CO}$ , the sum of metallized and sulfurized iron/nickel is found to increase with  $P_{SO_2}$ . The meager percentage for nickel at  $P_{SO_2} = 0$ , can be explained by the presence of olivine minerals, which can interlock NiO in its crystal structure and thus inhibit reduction. However, by increasing  $P_{SO_2}$ , the metallized and sulfurized content of nickel increases dramatically, possibly suggesting the convenience of sulfurizing NiO from within the olivine structure.

## Chapter 7: Future Work

In the current study, the CO (in the input gas) to Fe<sub>2</sub>O<sub>3</sub> molar ratio was selected as five times higher than the stoichiometrically required amount to reduce all Fe<sup>3+</sup> to Fe<sup>2+</sup> minerals. Similar studies can be conducted for lower CO to Fe<sub>2</sub>O<sub>3</sub> ratios. Furthermore, the calcination-partial reduction temperature was fixed at 900 °C, and reducing gases were only purged after the maximum temperature was reached. The XRD analysis of the calcined samples shows the formation of olivine minerals, which subsequently explains very low metallization of nickel. Thus, for future experimentations, it is recommended to examine the temperature between 750 °C and 900 °C. This methodology can avoid the interlocking of NiO within olivine structure and thus improve the reduction of nickel to metallic state. Lastly, the metallization of nickel and iron in a sulfurizing atmosphere needs to be studied in further detail to understand the effect of higher sulfur in fuels on the overall performance of rotary kiln calcination.

## References

- [1] F. K. Crundwell, M. S. Moats, V. Ramachandran, T. G. Robinson, and W. G. Davenport, *Extractive Metallurgy of Nickel, Cobalt and Platinum-Group Metals*. Elsevier, 2011.
- [2] G. Li, H. Jia, J. Luo, Z. Peng, Y. Zhang, and T. Jiang, “Ferronickel Preparation from Nickeliferous Laterite by Rotary Kiln-Electric Furnace Process,” in *Characterization of Minerals, Metals, and Materials*, Springer International Publishing, 2016, pp. 143–150.
- [3] M. Rao, G. Li, T. Jiang, J. Luo, Y. Zhang, and X. Fan, “Carbothermic Reduction of Nickeliferous Laterite Ores for Nickel Pig Iron Production in China: A Review,” *JOM*, vol. 65, no. 11, pp. 1573–1583, 2013.
- [4] N. Campagnol, K. Hoffman, A. Lala, and O. Ramsbottom, “The Future of Nickel: A Class Act,” 2017.
- [5] International Nickel Study Group, “The World Nickel Factbook,” 2018.
- [6] A. D. Dalvi, W. G. Bacon, and R. C. Osborne, “The Past and the Future of Nickel Laterites,” in *PDAC 2004 International Convention, Trade Show & Investors Exchange*, 2004.
- [7] D. R. Swinbourne, “Understanding Ferronickel Smelting From Laterites Through Computational Thermodynamics Modeling,” *Mineral Processing and Extractive Metallurgy*, vol. 123, no. 3, pp. 127–140, 2014.
- [8] C. Butt and D. Cluzel, “Nickel Laterite Ore Deposits: Weathered Serpentinites,” *Elements*, vol. 9, no. 2, pp. 123–128, 2013.
- [9] A. Bunjaku, “The Effect of Mineralogy, Sulfur, and Reducing Gases on the Reducibility of Saprolitic Nickel Ores,” Aalto University, 2013.

- [10] R. Elliott, F. Rodrigues, C. A. Pickles, and J. Peacey, "A Two-Stage Thermal Upgrading Process For Nickeliferous Limonitic Laterite Ores," *Canadian Metallurgical Quarterly*, vol. 54, no. 4, pp. 395–405, 2015.
- [11] R. S. B. Elliott, "A Study on the Role of Sulfur in Thermal Upgrading of Nickeliferous Laterite Ores," Queen's University, 2015.
- [12] A. E. M. Warner, C. M. Díaz, A. D. Dalvi, P. J. Mackey, and A. V Tarasov, "JOM World Nonferrous Smelter Survey, Part III: Nickel: Laterite," *JOM*, vol. 58, no. 4, pp. 11–20, 2006.
- [13] T. Norgate and S. Jahanshahi, "Assessing the Energy and Greenhouse Gas Footprints of Nickel Laterite Processing," *Minerals Engineering*, vol. 24, no. 7, pp. 698–707, 2011.
- [14] C. Red, R. Matthias Pfennig, S. Fritsch, and H. Muller, "Refining of Ferronickel," in *The Thirteenth International Ferroalloys Congress Efficient Technologies in Ferroalloy Industry*, 2013, vol. 229.
- [15] A. Ma, S. Mostaghel, and K. Chattopadhyay, "Review of Applicable Desulfurization Models For Crude Ferronickel Refining," *Mineral Processing and Extractive Metallurgy*, vol. 127, no. 1, pp. 10–28, 2018.
- [16] R. A. Bergman, "Nickel Production from Low-Iron Laterite Ores: Process Descriptions," *CIM Bulletin*, vol. 96, no. 1072, pp. 127–138, 2003.
- [17] N. Brand, C. R. M. Butt, and M. Elias, "Nickel Laterites: Classification and Features," *Journal of Australian Geology and Geophysics*, vol. 17, no. 4, pp. 81–88, 1998.
- [18] G. M. Mudd, "Global Trends and Environmental Issues in Nickel Mining: Sulfides versus Laterites," *Ore Geology Reviews*, vol. 38, no. 1, pp. 9–26, 2010.
- [19] M. P. Foose, "Nickel-Mineralogy and Chemical Composition of Some Nickel-Bearing

- Laterites in Southern Oregon and Northern California,” in *Contributions to Commodity Geology Research (US Geological Survey Bulletin : 1877)*, US Government Printing Office, 1992, pp. E1–E24.
- [20] A. Manceau and G. Calas, “Nickel-Bearing Clay Minerals: II. Intracrystalline Distribution of Nickel: An X-ray Absorption Study,” *Clay Minerals*, vol. 21, no. 3, pp. 341–360, 1986.
- [21] B. I. Whittington and D. Muir\*, “Pressure Acid Leaching of Nickel Laterites: A Review,” *Mineral Processing and Extractive Metallurgy Review*, vol. 21, no. 6, pp. 527–599, 2000.
- [22] J. Kyle, “Nickel Laterite Processing Technologies - Where to Next?,” in *ALTA Nickel-Cobalt-Copper Conference*, 2010.
- [23] O. Nakai, M. Kawata, Y. Kyoda, and N. Tsuchida, “Commissioning of Coral Bay Nickel Project,” in *ALTA Nickel-Cobalt Conference*, 2006.
- [24] J. Vaughan, W. Hawker, and D. White, “Chemical Aspects of Mixed Nickel-Cobalt Hydroxide Precipitation and Refining,” in *ALTA Nickel-Cobalt-Copper Conference*, 2011.
- [25] J. E. Fittock, “Nickel and Cobalt Refining at QNI Pty Ltd, Yabulu, QLD,” in *AUSIMM Monograph 19*, 1992, pp. 1–47.
- [26] M. A. Rhamdhani, J. Chen, T. Hidayat, E. Jak, and P. Hayes, “Advances in Research on Nickel Production Through the Caron Process,” in *European Metallurgical Conference*, 2009.
- [27] P. Prasetyo, “The Effect of Entry into Force of the Mining Law 2009 Began January 2014 in the Production of NPI (Nickel Pig Iron) in China,” *IOP Conference Series: Materials Science and Engineering*, vol. 285, 2018.
- [28] E. Keskinilic, “Nickel Laterite Smelting Processes and Some Examples of Recent Possible

- Modifications to the Conventional Route,” *Metals*, vol. 9, no. 9, 2019.
- [29] K. Quast, J. N. Connor, W. Skinner, D. J. Robinson, and J. Addai-Mensah, “Preconcentration Strategies in the Processing of Nickel Laterite Ores Part 1: Literature review,” *Minerals Engineering*, vol. 79, pp. 261–268, 2015.
- [30] M. Adams *et al.*, “Piloting of the Beneficiation and Epal Circuits for Ravensthorpe Nickel Operations,” in *International Laterite Nickel Symposium*, 2004, pp. 193–202.
- [31] S. Kashani-Nejad and I. Candy, “Modeling of Nickel Laterite Kiln Processing - A Conceptual Overview,” in *Nickel and Cobalt 2005: Challenges in Extraction and Production: Proceedings of the International Symposium on Nickel and Cobalt*, CIM, 2005, pp. 231–246.
- [32] F. M. Rodrigues, “Investigation Into The Thermal Upgrading of Nickeliferous Laterite Ore,” Queen’s University, 2013.
- [33] N. Voermann, T. Gerritsen, I. Candy, F. Stober, and A. Matyas, “Developments in Furnace Technology for Ferro-Nickel Production,” in *Tenth International Ferroalloys Congress*, 2004.
- [34] C. Doyle, “The Steps Required to Meet Production Targets at PT Inco, Indonesia: A New Innovative Business Strategy,” in *International Laterite Nickel Symposium*, 2004, pp. 667–684.
- [35] H. Ishiyama and Y. Hirai, “Fluid Bed Roasting at Tokyo Nickel Company,” in *Proceedings of the Nickel-Cobalt International Symposium*, 1997, pp. 133–140.
- [36] K. Adham and C. Lee, “Process Design Considerations For the Fluidized Bed Technology Applications in the Nickel Industry,” *CIM Bulletin*, 2018.

- [37] C. G. Fink and V. S. Marchi, "Beneficiating Ferruginous Bauxites Through Chlorination," *Transactions of The Electrochemical Society*, vol. 74, no. 1, pp. 469–494, 1938.
- [38] R. D. Holliday and D. J. Milne, "Experimental Evaluation of Routes for Purification of Bauxite by Gas-Solid Reactions," *Industrial & Engineering Chemistry Process Design and Development*, vol. 14, no. 4, pp. 447–452, 1975.
- [39] P. Bolsaitis and K. Nagata, "Kinetics of Sulfidization of Iron Oxide with SO<sub>2</sub>-CO Mixtures of High Sulfur Potential," *Metallurgical Transactions B*, vol. 11, no. 2, pp. 185–197, 1980.
- [40] K. Nagata and P. Bolsaitis, "Selective Removal of Iron Oxide from Laterite by Sulphurization and Chlorination," *International Journal of Mineral Processing*, vol. 19, no. 1, pp. 157–172, 1987.
- [41] V. Sidorov, V. Rigin, P. Min, and Y. Folomeikin, "Removal of a Sulfur Impurity From Complex Nickel Melts in Vacuum," *Russian Metallurgy (Metally)*, vol. 2015, no. 11, pp. 910–915, 2015.
- [42] T. Ogura, K. Kuwayama, A. Ono, and Y. Yamada, "Production of Fe-Ni by the Rotary Kiln-Electric Furnace Process at Hyuga Smelter," *International Journal of Mineral Processing*, vol. 19, no. 1, pp. 189–198, 1987.
- [43] A. Roine and others, "HSC Chemistry 6.0," *Outokumpu Technology, Pori, Finland*. 2006.
- [44] D. V. Furta, "13. Equilibrium Module-Description of Menus and Options," 2014.
- [45] B. H. Bowen and M. W. Irwin, "Coal Characteristics," 2008.
- [46] J. H. A. Kiel, W. Prins, and W. P. M. van Swaaij, "Mass Transfer Between Gas and Particles in a Gas-Solid Trickle Flow Reactor," *Chemical Engineering Science*, vol. 48, no. 1, pp. 117–125, 1993.

- [47] C. J. Hallet, “A Thermodynamic Analysis of the Solid State Reduction of Nickel from Laterite Minerals,” in *Nickel-Cobalt International Symposium*, 1997, pp. 299–312.